

Single Phase Pump: Non-Mechanical Valvular Conduit

by

Bong-Joo Lee

A thesis
presented to the University of Waterloo
in fulfillment of the
thesis requirement for the degree of
Master of Applied Science
in
Mechanical Engineering

Waterloo, Ontario, Canada, 2011

© Bong-Joo Lee 2011

Author's Declaration

I hereby declare that I am the sole author of this thesis. This is a true copy of the thesis, including any required final revisions, as accepted by my examiners.

I understand that my thesis may be made electronically available to the public.

Abstract

This thesis evaluates performance of a non-mechanical conduit valve that was designed for the purpose of this research. The motivation came from the need for a cooling system of portable computers (e.g. laptops and netbooks). As the technology of micro-processors in portable computers advances, they will generate more heat, requiring a more effective and efficient way to cool the system. Based on this fact, a new method of heat dissipation using a single-phase liquid (i.e. water) instead of air was examined. This potentially allowed 80 times more heat dissipation, which translates to better and faster computers for the near future.

In designing a single-phase-liquid micro-scale cooling system, various pump mechanisms and their functionalities were considered. It was concluded that a diaphragm pump design is the most effective candidate for this cooling system. The essential component when designing a diaphragm pump is a valve; however, the main issues in selecting a valve are its mechanics and required maintenance. Thus, the non-mechanical valvular conduit, which uses no moving mechanism, was studied through a combination of numerical/computational and experimental methods.

The non-mechanical valvular conduit is a micro-channel with a complex geometry; hence, this conduit uses the principle of pressure resistance in the channel flow such that the flow is uni-directional. Through the numerical study, the valvular conduit design's geometric dimensions were optimized. Then numerical simulations of the pumping/oscillating sequence of the valvular conduit were conducted to examine the effectiveness of the valve when placed in use for a diaphragm pump. It was found that the non-mechanical valve was 38 % more effective in the favorable direction than the opposite direction. As for the necessary heat dissipation, this conduit design demonstrates a great potential to dissipate the thermal design power (TDP) of Intel Pentium D processor (i.e. 130 [W]). During the experiments, the non-mechanical valve confirmed the numerical results. The experimental results also demonstrated that the favorable direction flow produced 244 % less pressure resistance than the opposite direction flow.

It was concluded that the non-mechanical valvular conduit can be an effective application for diaphragm pumps in macro and micro-scale without any possibility of obstructing a mechanism.

Acknowledgements

I am ever so grateful for the support, guidance and encouragement from God and many people during these past few years.

Firstly, I'd like to thank God for His constant grace, love and encouragement that He provided throughout my life. Without Him, I would not be the man I am today. (Hebrews 13:5-6)

I am forever grateful to my parents, Jong-Soo, Hyae-Kyung, and my brother, Seung-Joo, for their love and support during past years, as well as my entire life. Thank you for being there for me. Seung-Joo, I could not have completed my thesis without you.

To my supervisor, Professor Richard J. Culham, for his guidance and expertise, thank you for giving me the opportunity to better myself. You were there to help me along the way, and encouraged me to figure things out on my own. Because of that, I learned so much and am grateful.

To my friend, Elmer Galvis, thank you for being like a brother to me and helping make these past few years memorable. You were an important part of the completion of my thesis.

Table of Contents

Author's Declaration.....	ii
Abstract.....	iii
Acknowledgements.....	v
Table of Contents.....	vi
List of Figures.....	ix
List of Tables.....	xii
Nomenclature.....	xiii
Greek Letters.....	xiii
Chapter 1 INTRODUCTION.....	1
1.1 Background Information.....	2
1.2 Motivation.....	3
Chapter 2 LITERATURE REVIEW.....	6
2.1 Microprocessor Cooling Systems.....	6
2.2 Liquid Cooling in Single Phase Micro-Channel.....	8
2.3 Pump Investigation.....	10
2.3.1 Types of Pump Mechanisms.....	11
2.3.2 Mechanism Feasibility for Micro-pumps.....	16
2.4 Check Valve Options.....	20
2.4.1 Non-mechanical Valves.....	21
Chapter 3 NUMERICAL APPROACH: MODELLING AND SIMULATION.....	29
3.1 Model Description.....	31
3.1.1 Model System Setup.....	33
3.1.2 Model Mesh Analysis.....	35
3.2 Steady State Simulation: Optimization.....	39
3.2.1 Angular Comparison.....	39
3.2.2 Channel Thickness Analysis.....	40
3.2.3 Curvature Radii of the Channel Analysis.....	43

3.3 Physics behind the Valvular Conduit Design	44
3.3.1 Pressure Loss in Positive Flow Direction.....	48
3.3.2 Pressure Loss in Negative Flow Direction	49
3.4 Transient Method: Pumping Simulation	50
3.4.1 Transient Flow Model.....	50
3.4.2 Transient Flow Results.....	53
Chapter 4 EXPERIMENTAL APPROACH	56
4.1 Experimental Setup/Test Rig Design	56
4.2 Prototype Design and Manufacture	60
4.2.1 Design Fabrication	61
4.2.2 Actual Manufactured of the Prototype.....	63
4.3 Test Rig Results.....	65
Chapter 5 RESULTS and DISCUSSIONS.....	68
5.1 Simulated results.....	68
5.1.1 Visual Observation from Numerical Study	68
5.1.2 Optimization of the Micro-valve (Steady State Results)	72
5.1.3 Evaluation of the Micro-valve (Transient Results)	74
5.2 Experimental results.....	77
5.2.1 Model Validation versus Experimental Results.....	80
5.2.2 Comparison of the Experiment and the Simulation.....	82
Chapter 6 CONCLUSION	88
Chapter 7 RECOMMENDATION	90
Appendix A Transient: Setup and Results	92
Appendix B Design: Drawings.....	97
Appendix C MicroMachining and MasterCAM	99
Appendix D Comparing Experimented and Simulated Results.....	109
Appendix E Uncertainty Analysis	112
E.1 Method.....	112
E.2 Uncertainty in Measured Values.....	113

E.2.1	Pressure.....	113
E.2.2	Dimensions.....	114
E.2.3	Flow Rate	115
Appendix F Pressure Resistance Calculations		116
Bibliography.....		120

List of Figures

Figure 1-1: Moore’s Law in ICCs [4]	2
Figure 1-2: History of Pentium Processor TDP vs. Frequency [5].....	3
Figure 2-1: Equivalent Thermal Circuit [6]	6
Figure 2-2: Schematics of the Liquid Cooling System.....	9
Figure 2-3: Heat Transfer from the microprocessor to the coolant.....	9
Figure 2-4: Liquid Cooling System for Computer Desktops [9].....	10
Figure 2-5: Operation Steps for a Piston Pump.....	12
Figure 2-6: Two types of Gear Pump Mechanism: External and Internal respectively ...	12
Figure 2-7: An example of diaphragm pump	13
Figure 2-8: One type of Peristaltic Pump.....	13
Figure 2-9: Mechanics of Rotary Vane Pump	14
Figure 2-10: Centrifugal Pump Mechanics [15]	15
Figure 2-11: Schematics of Mechanical Check Valve – (1) Forward Flow; (2) Reverse Flow.....	20
Figure 2-12: Conical and flat-walled diffusers	21
Figure 2-13: Schematic of Diffuser and Nozzle	22
Figure 2-14: Operation of the diffuser-based pump (single-chamber and single- diaphragm): (a) Supply Mode; (b) Pump Mode [26]	22
Figure 2-15: Stability map of a diffuser [26]	23
Figure 2-16: Flow losses in a gradual conical expansion region [12] [27].....	24
Figure 2-17: Typical performance maps for flat-wall and conical diffusers at similar operating conditions: a) flat-wall and b) conical [27]	25
Figure 2-18: N. Tesla’s original valvular conduit design [28].....	26
Figure 2-19: Non-mechanical Valvular Conduit [28].....	27
Figure 2-20: Tesla’s structure investigated in Gamboa et al.’s research [30]	28
Figure 3-1: Non-mechanical Valvular Conduit Design for the Numerical Approach [29]	29

Figure 3-2: Operation of Non-mechanical Valvular Conduit on single-chamber and single-diaphragm pump: (a) Supply Mode; (b) Pump Mode	30
Figure 3-3: Physical domain of the valve-less design [ANSYS-CFX]	32
Figure 3-4: Model and Physical Domain [ANSYS-CFX [31]]	34
Figure 3-5: Mesh Convergence: Pressure vs. Number of Elements Plot	38
Figure 3-6: Final Mesh of the Valvular Conduit System [ANSYS-CFX]	38
Figure 3-7 Angular Analysis for Optimization	40
Figure 3-8: Channel thickness (t) change: Pressure difference between negative flow and positive flow at various angles of the channel	41
Figure 3-9: Pressure ratio analysis of the various channel thickness	42
Figure 3-10: Pressure Difference at various curvature radii ($R_1 = R_2$)	43
Figure 3-11: Pressure Ratio at various curvature radii ($R_1 = R_2$)	44
Figure 3-12: Schematic layout of the conduit design	45
Figure 3-13: Pressure resistance circuit schematics of the conduit design	46
Figure 3-14: Oscillation pressure curve at Frequency 1 [Hz]	51
Figure 3-15: Oscillating Pressure and Velocity over time at Frequency 1 [Hz]	53
Figure 3-16: Oscillating Pressure and Velocity over time at Frequency 100 [Hz]	54
Figure 4-1: Test rig design of the fluid flow circuit	57
Figure 4-2: Infusing in POSITIVE flow direction at a specified volumetric flow rate	58
Figure 4-3: Infusing in NEGATIVE flow direction at a specified volumetric flow rate	58
Figure 4-4: Refilling the syringes	59
Figure 4-5: Actual Test Rig for the Experiment	59
Figure 4-6: General geometry of a valvular conduit with the flow direction indication	60
Figure 4-7: Cover Design (LEFT); Exploded View (RIGHT)	61
Figure 4-8: Master-CAM screen shot (LEFT); Atometric G4-ULTRA CNC (RIGHT)	62
Figure 4-9: Fabricated prototype of the valvular conduit design	63
Figure 4-10: Experimental results with uncertainty analysis	66
Figure 5-1: Velocity field diagram – (A) positive flow direction; (B) negative flow direction	69

Figure 5-2: Streamline diagram – (A) positive flow direction; (B) negative flow direction	70
Figure 5-3: Schematic layout of the alternative conduit design	71
Figure 5-4: Pressure resistance circuit schematics of the alternative design.....	71
Figure 5-5: Optimization Plots of the physical characteristics of the conduit: Up – Angle, Middle – Channel Thickness, and Bottom – Radii of the Curvature	73
Figure 5-6: Normal Velocity of the outlet over normalized time	75
Figure 5-7: Plot of accumulated flow rate over a period at frequency 100 [Hz].....	76
Figure 5-8: Plot of average velocity over frequency	76
Figure 5-9: Pressure drop reading location in the test rig.....	78
Figure 5-10: Multiple pressure measurements at specified flow rates	79
Figure 5-11: Simulation for valvular conduit design confirmation.....	81
Figure 5-12: Comparison between experimental and simulated results with uncertainty analysis	82
Figure 5-13: Comparison between experimental and simulated difference results with uncertainty analysis.....	83
Figure 5-14: Simulated results with tolerance $\pm 5\%$	85
Figure 5-15: Comparison between experimental and simulated results with dimensional tolerance and uncertainty analysis considered	86
Figure 5-16: Pressure difference between negative and positive flow direction plot of simulated and experimental results with uncertainty and dimensional tolerance considered.....	87

List of Tables

Table 1-1: Typical values of the convection heat transfer coefficient [6].....	4
Table 2-1: Average Physical Dimensions and Weight of Different Compact Portable Computers [10].....	11
Table 2-2: Performance of Various Micro-pumps.....	16
Table 2-3: Comparison between Mini-centrifugal Magnetic Drive Pump, Micro-Annular Gear and Piezoelectric Diaphragm Pump.....	18
Table 3-1: Meshing Trials	36
Table 3-2: Grid Convergence Index with Mesh Number.....	37
Table 3-3: Micro-channel thickness - normal velocity list.....	41
Table 3-4: Area averaged velocity (w) of the conduit design layout obtained from ANSYS-CFX simulation.....	45
Table 3-5: Evaluation of Pressure Resistances, ξ , for Positive Flow Direction.....	48
Table 3-6: Evaluation of Pressure Resistances, ξ , for Negative Flow Direction.....	49
Table 3-7: Pressure input expression Setup for ANSYS-CFX.....	53
Table 4-1: Actual approximate measurements from microscope software.....	64
Table 4-2: Experimental Results from the Test Rig.....	65
Table 5-1: Pressure Loss Comparison between the Original and the Alternative Design	72
Table 5-2: Optimization of the Valvular Conduit Design.....	74
Table 5-3: Simulated Results from ANSYS-CFX Workbench.....	80
Table 5-4: Simulated discrepancy study results.....	84

Nomenclature

A	area, m^2
A_s	surface area, m^2
C_p	constant pressure specific heat, $kJ/(kg \cdot ^\circ C)$
D	characteristic length, m
h	convective heat transfer coefficient, $W/(m^2 \cdot K)$
k	thermal conductivity, $W/(m \cdot K)$
L	length, m
P	pressure, kPa
q	energy flux, energy per unit area and per unit time, W/m^2
Q	heat transfer rate, W
Q_{conv}	heat transfer rate through convection, W
Q_{cond}	heat transfer rate through conduction, W
Q_{rad}	heat transfer rate through radiation, W
R	radius of curvature, mm
T	temperature, K or $^\circ C$
T_s	surface temperature, K or $^\circ C$
\bar{V}	voltage, V
V	voltage, V
\dot{V}	flow rate, m^3/s
w	area averaged velocity, m/s

Greek Letters

α	angle, $^\circ$ or rad
μ	dynamic viscosity, $kg/(m \cdot s)$ or $N \cdot s/m^2$
ν	kinematic viscosity, $=\mu/\rho$, m^2/s
ρ	density kg/m^3

Chapter 1

INTRODUCTION

In recent years computer technology has advanced at an exponential rate thereby allowing for the packaging of more complex feature sets into compact devices. In parallel with this miniaturization, the power requirements have increased significantly resulting in much higher levels of heat flux that can potentially lead to overheating. To guarantee that the components' functionality is optimal, the operating temperature ranges roughly between 50 – 80 [°C] (122 – 176 [°F]) [1] and must be maintained by dissipation of the heat generated by each component. Otherwise, the electronic device may degrade in operation and ultimately fail prematurely. It is imperative to monitor operating temperature to ensure that steady state conditions are maintained below critical levels that would cause the silicon device in the processors to fail or to go through intermittent or permanent damage [1]. These days, portable computers use integrated circuit chips (ICC). These ICCs are becoming intricate enough that they tend to generate significant heat (e.g. Intel Pentium D processor generates thermal design power up to 130 [W] with a chip die size of 206 [mm²] [2]). Thus, a major concern of portable computers is the cooling system that is used to dissipate the heat generated. Effective methods for cooling electronic applications typically include forced and natural convection where air is the cooling medium. These convective methods are usually implemented with an extended surface or heat sink that helps maximize the surface area interface between the heat source and the surrounding medium. Forced convection can be further enhanced by applying a fan directly to the surface of the heat sink to reduce the film resistance. When applying these modes of cooling, the heat dissipation is directly related to the size of the fan and/or the heat sink; therefore, this presents a limitation for the size of the actual design of the overall computer system. Thus, a different and more effective process of the heat dissipation must be explored [3].

1.1 Background Information

Evolution of Microprocessors

Over the years, the computer industry has been constantly improving the performance of microprocessors as a result of consumer's demand for faster and more powerful computers. Thus, the microprocessors are becoming more intricate, which is described by Moore's Law. Moore's Law states that the number of transistors in computer ICCs doubles every two years. Moore's law has predicted this trend since the 1960s and this has proven to be fairly accurate, as shown in Figure 1-1.

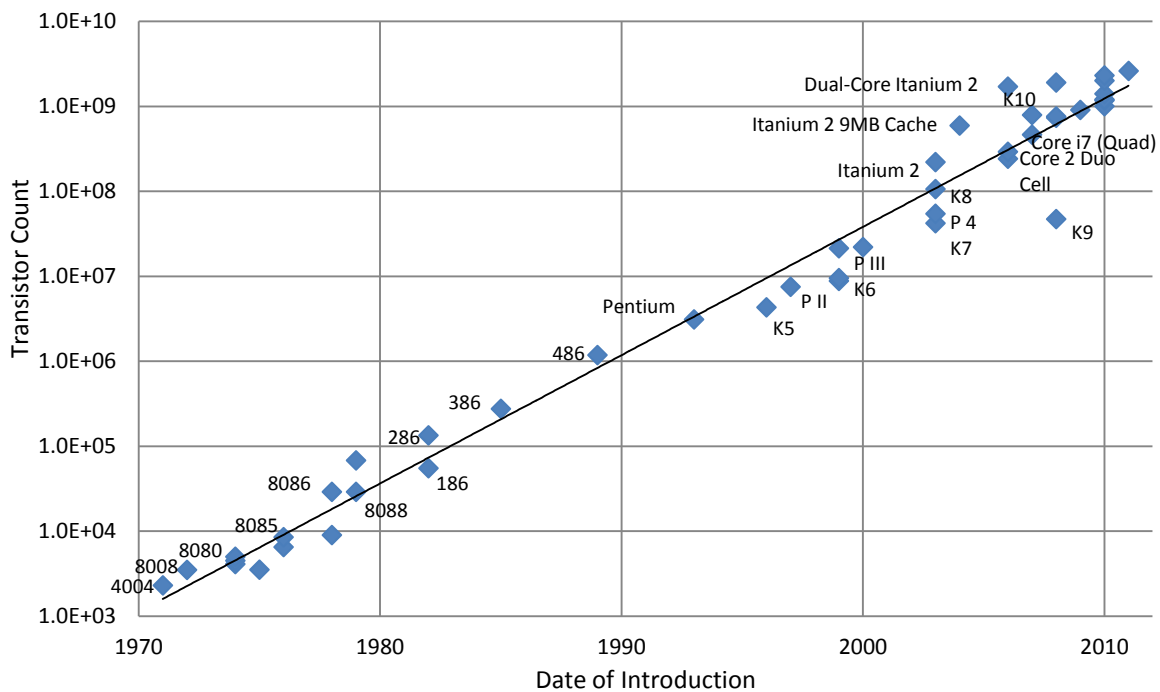


Figure 1-1: Moore's Law in ICCs [4]

From Mahajan et al.'s [5] research paper, it is recognized that this trend of increasing transistor density would ultimately lead to increasing necessary power/heat dissipation. Hence, there are various thermal management approaches of the microprocessor, which will be explained later. The electrical performance of the ICC microprocessor can be improved by two methods: increasing the transistor density and/or increasing the

operating rate (i.e. the frequency of the microprocessor). In either method, the consequence is an increase in the heat generated by the microprocessor. Over the years, the operating frequency (the common measure of microprocessor performance) for Pentium microprocessors has increased from 400 [MHz] to approximately 3,000 [MHz] which led to a corresponding increase in the amount of heat required to dissipate, also known as thermal design power (TDP). As illustrated in Figure 1-2, the history of Pentium processors' TDP is linearly proportional to the frequency of the microprocessors. This means future ICCs require cooling systems that can dissipate the necessary heat to operate optimally.

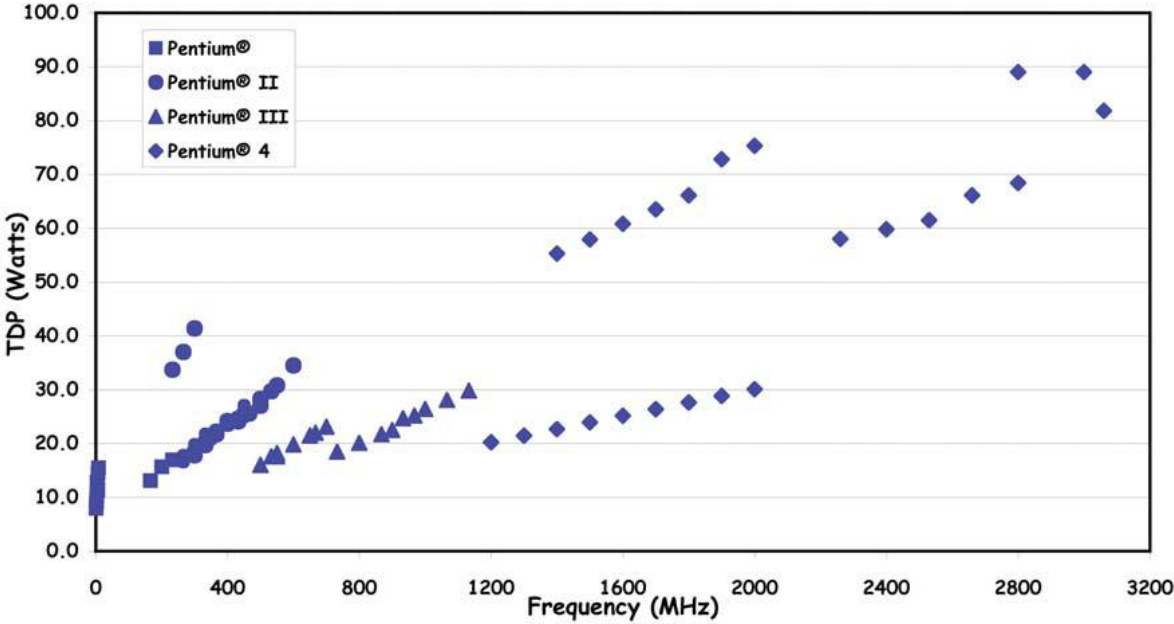


Figure 1-2: History of Pentium Processor TDP vs. Frequency [5]

1.2 Motivation

Heating Issues in Electronics

ICCs must be maintained within a specified operating temperature range [5]. In order to dissipate the necessary heat, a cooling system is implemented. As explained previously, cooling systems use one of two methods of cooling/heat transfer: natural convection or

forced convection. From the fundamentals of heat transfer, the heat transfer rate can be defined as

$$Q = h \cdot A \cdot \Delta T \quad \text{Equation 1-1}$$

where, Q is the heat transfer rate, [J/s = W], h is heat transfer coefficient, [W/(m²K)] (See Table 1-1 for more detail), A is the heat transfer surface area, [m²], and ΔT is the difference in temperature between the solid surface and surrounding fluid area, [K].

Table 1-1: Typical values of the convection heat transfer coefficient [6]

Process		$h \left[\frac{W}{m^2 \cdot K} \right]$
Free/Natural Convection	<i>Gases</i>	2 – 25
	<i>Liquids</i>	50 – 1000
Forced Convection	<i>Gases</i>	25 – 250
	<i>Liquids</i>	100 - 20,000

As shown, the convective heat transfer is proportional to the product of the heat transfer coefficient and the surface area. Therefore, when comparing natural and forced convection, a cooling system that uses natural convection requires a larger surface area to implement, resulting in larger heat sinks, which then translates into more space in the overall design. Such a system is only sufficient for cooling microprocessors operating at low to mid electric operating power. Forced convection heat transfer differs from natural convection in that the air flow is applied directly onto the surface (using a fan). As a result, it can cool microprocessors operating at mid to high power. Thus, a forced convection cooling system is relatively small compared to a natural convection cooling system, and is capable of allowing an ICC to operate at a higher electrical power.

As the microprocessors increase in electrical performance, the ICC packing density becomes greater and/or operates at a higher signal transfer rate. As the demand for more powerful microprocessors continues to increase, even forced air convective cooling systems are not adequate to dissipate the necessary heat in order to maintain operating

temperatures within recommended specifications. One could argue that the fan size could just be increased, since forced air convection is directly proportional to the size of the fan; however, many have discovered that large fans will increase the noise factor and the size of the overall design. Thus, instead of increasing the fan capacity, other elements of the cooling system can be altered to enhance cooling performance. As opposed to using air as the fluid of the system, a liquid coolant, which has higher thermal conductivity, can be applied to the system such that more heat transfer/removal can occur in the system. This liquid cooling system concept can provide sufficient cooling while still allowing adequate space in the portable computer's housing.

Currently, the majority of cooling systems used in laptops are air-cooled-convective cooling systems. This cooling system has thus far been sufficient for operation but the intricacy of the microprocessor is still increasing as described by Moore's Law. It is evident that the heat dissipation requirement increases in proportion to microprocessor technology advancement; hence, alternative methods of the cooling system must be investigated. The primary focus of this work is to investigate reliable, low profile, liquid micro-pumps that can be incorporated into cold plate designs for cooling microelectronic processors that might be used in laptop computers.

After evaluating various pump mechanisms and their functionality, a diaphragm pump was selected for the research (see Section 2.3.2). The study showed that a new micro diaphragm pump was required to build an effective cooling system for this purpose. In a micro-diaphragm pump, the valve is one of the critical components. Given the fact that the size of the valve must be micro-scale, several available mechanics of the valve were investigated. This led to a conclusion that fewer mechanisms in the valve are ideal because any particles can obstruct and/or impair the device. Thus, the non-mechanical design of the valve became the main focus of the thesis with numerical/computational and experimental analytical methods.

Chapter 2

LITERATURE REVIEW

2.1 Microprocessor Cooling Systems

Two important criteria for effective cooling of microprocessor systems include the ability to dissipate heat and the ease of integration with the computers. There are many types of cooling systems which are available for practical applications such as natural/forced convection, heat pipes, liquid cooling, thermal-electric devices and refrigeration. When comparing the various types of the cooling systems, the thermal resistance and the implementation in computers were the two main factors considered in this section. Thermal resistance is the temperature differences across the device per unit of heat energy (i.e. TDP, thermal design power) [6]. During heat transfer, a thermal circuit can be used to represent the heat flow of the system, similar to an electric circuit as shown in Figure 2-1.

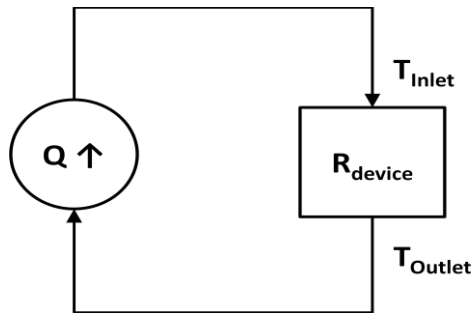


Figure 2-1: Equivalent Thermal Circuit [6]

In Figure 2-1, the heat flow (Q), temperature (T), and the thermal resistance (R) are represented by current, voltage, and resistance of an electric circuit model respectively. Hence, if the thermal resistance is lowered, the heat dissipation is greater due to a greater difference of the inlet and outlet temperatures.

Several cooling systems were researched: 1) **Natural/forced convection** is the simplest to apply but the boundary thermal resistance can be large compared to other cooling systems. 2) A **heat pipe system** can be used as a thermal conduit between the heat source and the sink. The heat pipe does not dissipate heat but rather provides a low resistance path to allow heat to move freely from a region of high thermal resistance, such as in a space constrained microprocessor to a region of lower thermal resistance as in the case of a convectively cooled heat sink. Overall, the system thermal resistance in a heat pipe system is typically lower; however it is imperative that the contact resistance between the heat pipe, the source and the sink be minimized to ensure an effective heat flow path within the circuit. 3) A **liquid cooling system** is an alternative technique for cooling of high heat flux, temperature critical systems. The liquid coolant is pumped through a micro-heat-exchanger to dissipate residual heat; afterward the liquid is cooled at a distant heat exchanger (e.g. radiator). There are many components required in this system: lines, fittings, pump, cold plate (e.g. micro-heat-exchanger) on microprocessor, and heat exchanger. 4) A **thermo-electric system** can also be used where the heat source is targeted specifically. Thermal electric devices have no moving parts, provide reliable operation, and have an effective performance (can provide thermal resistance approaching or even below 0 [K/W]) [5]. The downside of this system is that the operational power to dissipate heat by the thermal electric-cooler needs to be cooled by another heat sink which means that the system can be inefficient. Another effective method for temperature control of microprocessors is 5) the **refrigeration system** which consists of a vapor compressor, condenser, expansion valve and evaporator. However, this system requires input power to operate and the system can be bulky and noisy due to the compressor [5].

Currently available cooling systems are insufficient and/or non-feasible for smaller-scale computers. A liquid cooling system is considered the best option for addressing the physical limitations of smaller laptops. The performance of the liquid cooling system is more effective than a natural/forced convection cooling system and more size-feasible for a microprocessor than a refrigeration system.

2.2 Liquid Cooling in Single Phase Micro-Channel

The level of heat flux on the surface of high performance microprocessors has exceeded 100 W/cm² while temperature constraints have remained constant, or in some cases been reduced to ensure reliable operating conditions [7]. Equation 2-1 shows the relationship between heat flux (Q/A) and the convective heat transfer coefficient. This relationship clearly shows that the resistance to heat flow can be lowered by either increasing the heat transfer coefficient or increasing the surface area. The thermal resistance can be lowered/improved by increasing the surface area (A).

$$Q = h \cdot A \cdot \Delta T \rightarrow R \left[\frac{K}{W} \right] = \frac{\Delta T}{Q} = \frac{1}{h \cdot A} \quad \text{Equation 2-1}$$

where, **R** is the thermal resistance, [K/W], **Q** is the heat transfer rate, [J/s = W], **h** is heat transfer coefficient, [W/(m²K)](See Table 1-1 for more detail), **A** is the heat transfer surface area, [m²], **T** is the difference in temperature between the solid surface and surrounding fluid area, [K].

From the Table 1-1, gas/air forced convective heat transfer coefficient is very low (ranging from only 25 – 250 [W/(m²K)]). Thus, cooling system in a compact portable computer can be improved by increasing the size of the heat exchanger or adding other cooling technologies. However, considering the space constraints in a compact portable computer system, these improvements will inevitably reach a limit. Therefore, instead of increasing the surface area to better the heat transfer, it seems more ideal to maximize the heat transfer coefficient.

Compared to air cooling, liquid cooling has the capability to reach 1 [kW/cm²] of heat flux using micro-channels [7]. From Table 1-1, the heat transfer coefficient of liquid forced convection is potentially 80 times greater than that of forced convection with air as the cooling medium. As a result, the surface area needed for liquid cooling can be significantly less than air/gas cooling. Liquid cooling systems are available for desktop computers; however, several issues associated with implementation have limited their adoption.

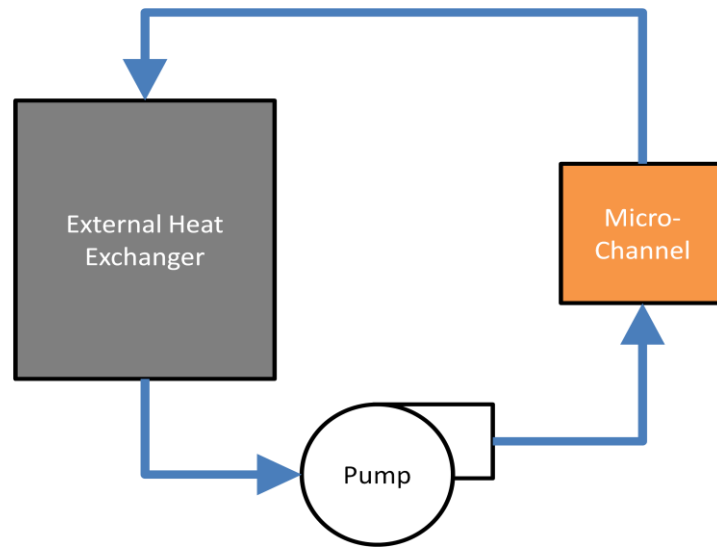


Figure 2-2: Schematics of the Liquid Cooling System

Figure 2-2 shows the schematic drawing for a liquid cooling system and the required essential components. As shown in Figure 2-3, the liquid cooling system is attached to the packaging system of the microprocessor either with a thermal interface material at the interface or by direct contact methods. Initially heat is transferred from the processor to the cold plate by conduction, allowing heat to migrate into the liquid medium travelling through the micro-channels. According to Kandikar, in the near future, single-phase cooling holds more immediate promise due to its reliable operation and ability to handle these heat fluxes. The flow boiling can be a more attractive option, but the operation is unstable and yields a low critical heat flux level which is not practical for implementation [7].

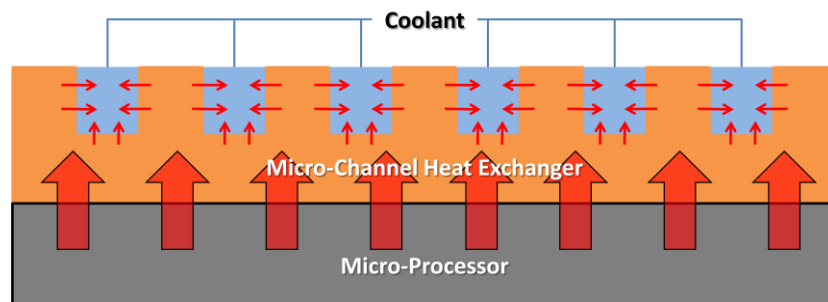


Figure 2-3: Heat Transfer from the microprocessor to the coolant

The challenge in a liquid cooling system using a micro-channel is that the coolant liquid needs to be cooled after removing heat from the surface of the microprocessor. The system requires an external heat exchanger, typically a liquid to air heat exchanger, so that heat can be dissipated to the environment and the coolant can be returned to a lower temperature before re-entering the micro-channels. While some liquid-based systems rely on buoyancy driven flow to circulate the cooling fluid, more often, a micro-pump is used to circulate the cooling medium through the system.

2.3 Pump Investigation

Usually a centrifugal pump is used in liquid cooling systems for larger computers including consumer-grade desktop computers as well as supercomputers [8].

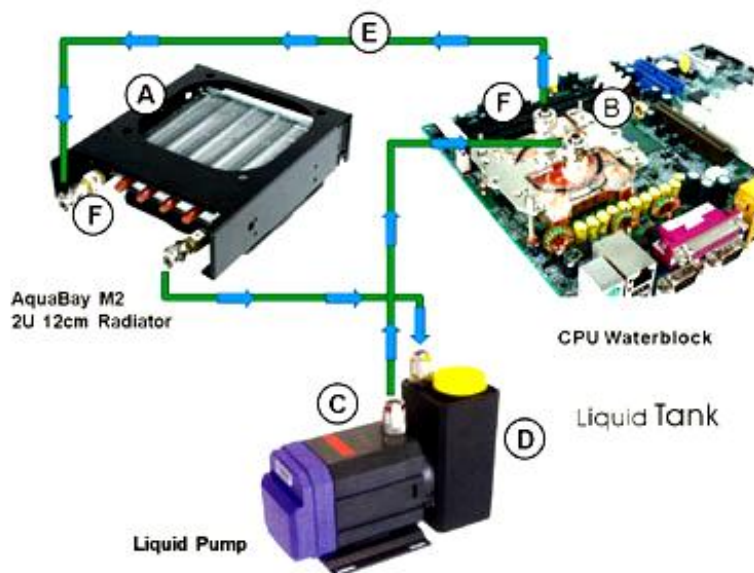


Figure 2-4: Liquid Cooling System for Computer Desktops [9]

Figure 2-4 illustrates the components in a PC liquid cooling system; however, this is unrealistic for compact portable computers. In an industrial design point of view, the bulkiest component is the pump.

Table 2-1: Average Physical Dimensions and Weight of Different Compact Portable Computers [10]

Types of Compact Portable Computers	Dimensions [mm] Width x Length X Depth	Weight [kg]
Netbook/Subnotebook	<267 x <191 x <33	<1.587
Ultraportable	229-305 x 203-229x <38	0.907-2.268
Thin and light	279-381 x <279x 25-43	2.268 -3.175
Desktop Replacement/Laptop	>381 x >279x >38	> 3.175
Luggable	>457 x >330 x >38	>5.443

As shown in Table 2-1, a typical dimension for a laptop is approximately 381 [mm] by 279.4 [mm] wide and 38 [mm] thick (381 [mm] x 279 [mm] x 38 [mm]). From Sidewinder: Computer Systems Inc., the size of a conventional centrifugal pump ranges from approximately 76–91 [mm] [11]. Hence, it is evident that a conventional centrifugal pump is not practical to use for a liquid cooling system in any compact portable computer since the average thickness ranges from 25–43 [mm]. Thus, further investigation is needed for the pump for a micro-size liquid cooling system.

2.3.1 Types of Pump Mechanisms

The main purpose of the pump is to circulate fluid in a uni-directional manner through the various components in the cooling loop. There are many types of pumps available for this purpose, including; piston; gear; diaphragm; and rotary vane. The type of pump used is dependent on a number of factors including: size and flow rate. The type of pump is selected based on noise constraints and reliability.

Piston Pump

The mechanism involves a piston or plunger which is placed inside a stationary cylinder and displaced back and forth. As shown in Figure 2-5, when 1) the piston is displaced in one direction, the fluid is replenished and stored in the cylinder, and then 2)

the piston pushes the fluid out of the cylinder as it moves to the opposite direction. Using check valves, the flow only flows in one direction; hence, the pump is operational. The mechanism oscillates in a way such that there is a constant average flow where the flow supply is necessary. The components included in a piston pump area cylinder, piston and check valves [12].

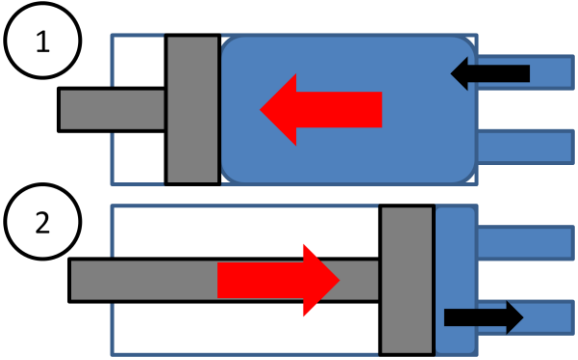


Figure 2-5: Operation Steps for a Piston Pump

Gear Pump (External and Internal)

One of the most common positive displacement pumps¹ is a gear pump. The pump operates by the meshing of gears to pump the fluid. The fluid is displaced by the rotary motion of the gears. There are two main types of gear pumps: external and internal pumps.

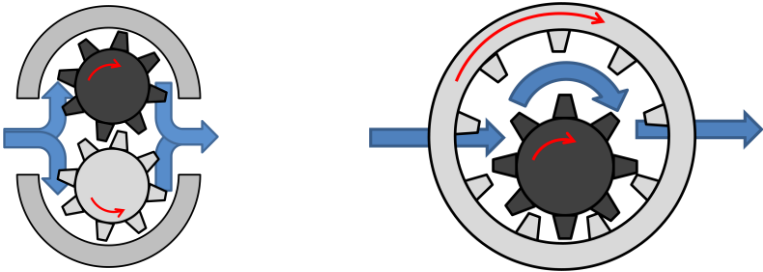


Figure 2-6: Two types of Gear Pump Mechanism: External and Internal respectively

As shown in Figure 2-6, an external gear pump uses two external spur gears which allow the fluid to pump between the casing of the pump and the gears. For an internal gear

¹ positive displacement – pump causes a fluid to move a fixed amount of fluid to be displaced (forced) to the connect pipe.

pump, it uses an internal and an external gear where the fluid is pumped through an internal gear and forced by the external gear. The components required for the gear pump are two gears, a motor to power one of the two gears and a container to enclose the fluid and the gears together. The advantage of the gear pump over the piston pump is that it requires no check valves [12].

Diaphragm Pump

The drive mechanism in a diaphragm pump is similar to a piston pump but instead of using a piston to oscillate, the diaphragm pump uses a pulsating flexible diaphragm to generate the volumetric difference. The advantage of the diaphragm is that the shape of the pump is more adaptable to low profile applications and does not require the functioning component to fully contract and expand for the fluid to circulate, unlike the piston pump. The diaphragm can be fabricated with rubber, thermoplastic, Teflon, piezoelectric crystal or anything that can change volume at a sufficiently high frequency.

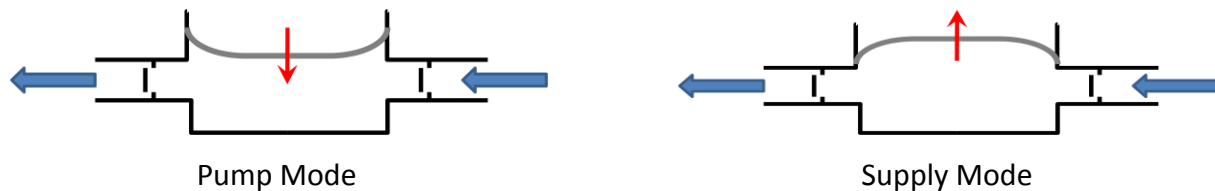


Figure 2-7: An example of diaphragm pump

Peristaltic/Roller Pump

A peristaltic pump operates using a flexible tube inside a circular casing. The fluid is squeezed and forced to pump by a rotor with multiple rollers.

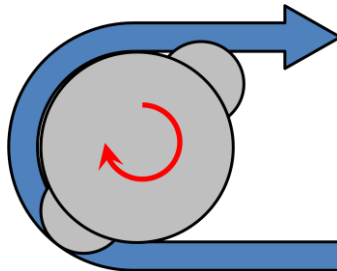


Figure 2-8: One type of Peristaltic Pump

Rotation of the rotor causes one of the rollers to occlude a section of the tube. Where the other section of the tube is opened up, this allows the fluid to exit the pump as demonstrated in Figure 2-8. If additional rollers used in the peristaltic pump, the pump becomes more efficient; however, more rollers will reduce the flexible tube life. A peristaltic pump is a positive displacement pump. The components required for this pump are a rotor, one or more rollers, flexible tubing, and a circular casing [13].

Rotary Vane Pump

Another positive displacement pump is a rotary vane pump. This pump is composed of a vane attached to a rotor which rotates in a larger circular cavity. The purpose of the vane is to seal the edges of the cavity which pumps the fluid as the rotor turns, as exemplified in Figure 2-9. Thus, the vane(s) is of a variable length (usually tensioned) so that it is in contact with the cavity at all times.

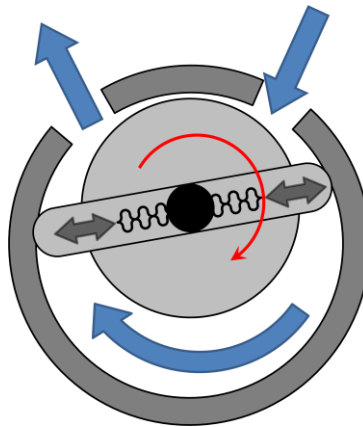


Figure 2-9: Mechanics of Rotary Vane Pump

Similar to a peristaltic/roller pump, increasing the number of vanes increases the efficiency of the pump. As shown in Figure 2-9, the components needed for this pump are a rotor, a larger circular cavity, and variable-length vane(s) [14].

Centrifugal Pump

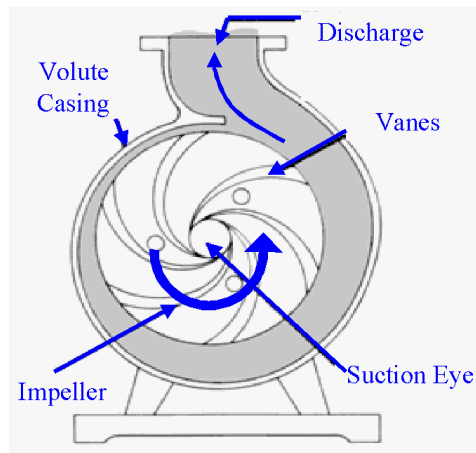


Figure 2-10: Centrifugal Pump Mechanics [15]

Figure 2-10 is the cross-section of a centrifugal pump which consists of a volute casing, an impeller with curved vanes and a motor to operate. The process of centrifugal pumping begins with fluid entering at the suction inlet to the center of the impeller (see the suction eye in Figure 2-10). As the impeller rotates, the fluid forces outward along the vanes due to centrifugal force. Then the fluid exits the impeller to a low-pressure section between the volute casing and the impeller. Due to the curvature of the impeller vanes, the fluid is forced in a radial direction by the centrifugal force where the fluid then is discharged as shown in Figure 2-10 [15].

Electromotive Pumps [16]

There are many nonstandard pumps that have been discussed in various papers. The magneto-hydrodynamics (MHD) pump is an example which utilizes electric conducting fluid such that when the fluid is induced in electric currents the fluid is in motion. The electro-hydrodynamics (EHD) pump is another example where the ionized particles/molecules in the fluid interact with the electric fields and the surrounding fluid creates hydrostatic motion to pump the fluid. Yet another example is the electro-osmotic (EO) pump where the fluid is pumped through a membrane that introduces an electric field. These pumps have been examined and reported on but within the current application,

the pros and cons of the application are undetermined. In addition, the cost to produce these pumps could not be found since they are not available for commercial use yet.

2.3.2 Mechanism Feasibility for Micro-pumps

Although pump technologies have matured over the years, the component hardware and the flow mechanics associated with macro scale pump technologies do not always translate well to the micro-scale. In order to examine various pump technologies, their performance, manufacturability, and reliability/sustainability were examined and evaluated. Circulating pumps are generally evaluated based on flow rate at a prescribed pressure head loss, Table 2-2 provides a summary of several pump technologies, including rotary, diaphragm, centrifugal, MHD, EHD, and EO mechanisms

Table 2-2: Performance of Various Micro-pumps

Types of Micro-Pump	Fluid	Performance		
		Flow Rate [$\mu\text{l}/\text{min}$]	Back Pressure [kPa]	Volume [mm^3]
Micro-Annular Gear [17]	low viscosity liquids	$2.88 \cdot 10^5$	0.000	$2.50 \cdot 10^{-1}$
Piezoelectric Diaphragm 70-180 Hz [18]	water	$7.20 \cdot 10^3$	0.000	$3.92 \cdot 10^3$
Peristaltic at 2 Hz [19]	DI water	$7.50 \cdot 10^{-2}$	0.000	N/A
Rotary Vane (magnetic micro-motor) [20]	water	$3.50 \cdot 10^2$	14.00	$6.04 \cdot 10^0$
Mini-Centrifugal Magnetic Drive [21]	water	$1.14 \cdot 10^7$	345.0	$8.98 \cdot 10^5$
Magneto-hydrodynamics (MHD) [22]	$\text{Ga}^{61}\text{In}^{25}\text{Sn}^{13}\text{Zn}^1$	$4.06 \cdot 10^5$	8.000	$4.40 \cdot 10^3$
Electro-hydrodynamics (EHD) [23]	ethanol	$1.40 \cdot 10^4$	2.480	$6.84 \cdot 10^0$
External Electro-osmotic (EO) [24]	DI water	$7.00 \cdot 10^3$	160.0	$1.41 \cdot 10^3$

In Table 2-2, the various micro-pump can operate from 0.075 to $1.14 \cdot 10^7$ [$\mu\text{l}/\text{min}$] at various back pressures.

From Chapter 1, a Pentium D processor generates thermal design power (TDP) up to 130 [W], and assuming the water temperature rises (ΔT) by 50 [$^{\circ}\text{C}$] with the standard condition, the required flow rate can be calculated ($\dot{V} = 3.74\text{E} \cdot 10^4$ [$\mu\text{l}/\text{min}$]) using

$$Q_{out} = TDP = \rho_{water} \cdot \dot{V} \cdot C_{p_{water}} \cdot \Delta T \quad \text{Equation 2-2}$$

where, Q_{out} is the heat transfer out of the system, ρ_{water} and $C_{p_{water}}$ are the density and specific heat capacity of water, \dot{V} is the volumetric flow rate, and T is the temperature difference from the inlet to outlet. Hence, one of the micro-pumps that can produce the required flow rate is the MHD pump; however, the pump needs to operate with high electrical conductivity fluid (e.g. $\text{Ga}^{61}\text{In}^{25}\text{Sn}^{13}\text{Zn}^1$, liquid metal). This is inappropriate for any CPU cooling systems. From Table 2-2, the EHD pump can produce a flow rate of $1.40 \cdot 10^4$ [$\mu\text{l}/\text{min}$] with ethanol. This rate is slightly below the required flow rate but still a potential choice for a cooling system. However, due to the mechanism of the pump (i.e. electrolysis of water), the performance of this pump deteriorates over time and usage. Another pump which is a viable option is the external EO pump with distilled water, but again, the complexity of generating a membrane with an electric field seems unsuitable for a cooling system in portable computers. Thus, the pumps in miscellaneous categories have performed well but the application for these pumps does not correspond to the needs of computer cooling systems [16].

Consequently, investigations for other mechanical pumps have been prepared. The mini-centrifugal magnetic drive pump, annual gear pump, and the piezoelectric diaphragm pump with operating frequencies ranging from 70 – 180[Hz] seem to be promising. The rotary vane pump and peristaltic pump did not perform well compared to the others. With this knowledge, a comparison of pros and cons between the mini-centrifugal magnetic drive pump, annual gear pump, and piezoelectric diaphragm pump have been analyzed.

Table 2-3: Comparison between Mini-centrifugal Magnetic Drive Pump, Micro-Annular Gear and Piezoelectric Diaphragm Pump

Types of Micro-Pump	Description	Functionality	
		Advantage	Disadvantage
Mini-centrifugal Magnetic Drive Pump	<ul style="list-style-type: none"> • a small-scaled conventional centrifugal pump • overcome high back pressure without jeopardizing flow rate 	<ul style="list-style-type: none"> • positive displacement pump with a constant flow • long service life • high precision dosage accuracy 	<ul style="list-style-type: none"> • largest micro-pump • bulky, not an easy shape to work with • manufacturability (i.e. impeller) • noise
Micro-Annular Gear	<ul style="list-style-type: none"> • a micro-scaled gear pump • overcome high back pressure and can produce flow rate in small package 	<ul style="list-style-type: none"> • suitable for low viscosity liquids • positive displacement pump with a constant flow • long service life • high precision dosage accuracy 	<ul style="list-style-type: none"> • bulky, not a easy shape to work with • the size can be quite large due to the gears • manufacturability (i.e. micro-gears) • noise
Piezoelectric Diaphragm	<ul style="list-style-type: none"> • a micro-scaled diaphragm pump • with piezoelectric device one side actuating pump operation frequency 70-180 [Hz] 	<ul style="list-style-type: none"> • shape and size are easier to manoeuvre • simple manufacturability • long service life 	<ul style="list-style-type: none"> • actuator (i.e. piezo-crystal) can be expensive • produces oscillating flow which may change the chamber volume by changing the curvature of a diaphragm • requires check valves due to the oscillating flow

Based on the findings from Table 2-3, the mini-centrifugal magnetic drive pump and the micro-annular gear pump are considered to be positive displacement pumps that can operate at a high pressure and produce a constant flow rate in a small package. Both pumps have an advantage that they can adapt to fluids with various viscosities and deliver flows at

a constant rate with precision. However, a disadvantage is that these pumps are bulky and sizeable due to the impeller or gears, as well as the enclosure of the pump. A centrifugal pump consists of an impeller and a volute casing which cannot be reshaped. Similarly, a gear pump is known to be round and cylindrical which cannot be compromised due to the shape of the gears and the mechanism performance. The piezoelectric diaphragm pump from H.K. Ma operates with one sided piezo-crystal actuator at a frequency which ranges from 70-180 [Hz]. Unlike the gear pump or the centrifugal pump, the shape of the piezoelectric diaphragm pump is quadrilateral, which is easier to adapt in a laptop cooling system. Also, the manufacturability is simpler than that of the mini-centrifugal magnetic drive pump and the micro-annular gear pump once the piezo-crystal is obtained. A disadvantage of the piezoelectric diaphragm pump is that the piezo-crystal actuator can be expensive. In addition, contrary to the other pumps, the diaphragm pump is not a positive displacement pump. The diaphragm pump functions via the volumetric change in the chamber; hence the flow of the pump oscillates, which means that the pump requires check valves in the inlet and the outlet.

Overall, the micro-pump used in a micro-scale single-phase liquid cooling system must provide sufficient flow rate to remove the high heat flux produced by CPU ICC chips to maintain an optimal operating temperature with minimal temperature gradient. As mentioned in Section 2.1, the micro-channels used in a cooling system provide enhanced heat transfer capabilities given that heat transfer coefficient increases as cross sectional area decreases but along with this enhanced heat transfer comes a sizeable increase in pressure drop. The micro-pump must be able to overcome the pressure drop to allow for effective circulation of the heat transfer fluid through the cooling loop. Other essential aspects of the micro-pump include the size, adaptability to the cooling system, cost, noise, and reliability. Taking all of this into consideration, the micro-pump which seems most feasible is the piezoelectric diaphragm pump. Among the various types of pump mechanics, the piezoelectric diaphragm pump uses a simple concept which has proven to perform well in terms of the flow rate [18]. This pump seems to be versatile and has the potential to be adaptable for laptop use from an industrial design point of view due to the shape and size

of the pump. While the MHD and EHD pumps have proven to be superior in performance, the piezoelectric diaphragm pump is more sustainable, leading to a longer service life. However, the downfall of using any diaphragm pump, as mentioned previously, is that it requires check valves at the inlet and the outlet of the pump.

2.4 Check Valve Options

In order to design an effective diaphragm pump it is important that the check valves provide continuous, reliable operation. From research papers, there are two options in designing a check valve: a mechanical check valve or a non-mechanical valve with no moving parts. Mechanical check valves have a simple purpose which allows the fluid to flow in one direction but blocks the flow in the opposite direction.



Figure 2-11: Schematics of Mechanical Check Valve – (1) Forward Flow; (2) Reverse Flow

Some of the moving parts inherent in a mechanical check valve include lift, swing, wafer, disc, ball, and diaphragm mechanisms [25]. In designing a valve for a micro-pump, however, the number of mechanisms should be minimized: even the smallest particle will damage and/or obstruct the valvular device. Thus, the latter option of a check valve (i.e. non-mechanical valve) seems more practical for the purpose of creating a single-phase liquid cooling system.

2.4.1 Non-mechanical Valves

A non-mechanical valve is a valve which has no moving parts. The principle of non-mechanical check valves is that using the resistance of fluid flow, one direction of the flow is favored compared to the opposite, resembling a check valve.

2.4.1.1 Diffuser/Nozzle

When investigating non-mechanical valves, the most common type available currently are nozzle-diffuser valves. As shown in Figure 2-12, there are two main types of diffusers: conical and flat-walled.

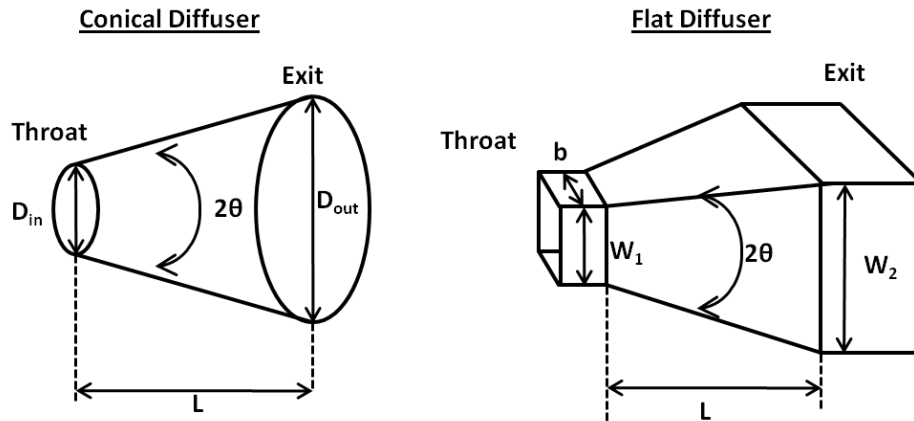


Figure 2-12: Conical and flat-walled diffusers

From conservation of mass principle in Equation 2-3, the entrance mass and the exit mass are equal; $\dot{m}_{entrance} = \dot{m}_{exit}$ which can be expressed as

$$\rho \cdot \dot{V}_{entrance} = \rho \cdot \dot{V}_{exit} \rightarrow A_{entrance} \cdot u_{entrance} = A_{exit} \cdot u_{exit} \quad \text{Equation 2-3}$$

where, ρ is the density of the fluid, \dot{V} is the volumetric flow rate, A is the cross-sectional area, and u is the normal velocity. Assuming that the fluid is incompressible (i.e. density, ρ), the volumetric flow rate is conserved ($\dot{V}_{entrance} = \dot{V}_{exit}$). Due to the profile of the diffuser/nozzle, the flow channel is gradually changing in cross-sectional area, so the

entrance and the exit cross-sectional area are radically different. Logically, conserving the volumetric flow, the change in the cross-sectional area would lead to a change in the velocity of the fluid and thus the kinetic energy [6].

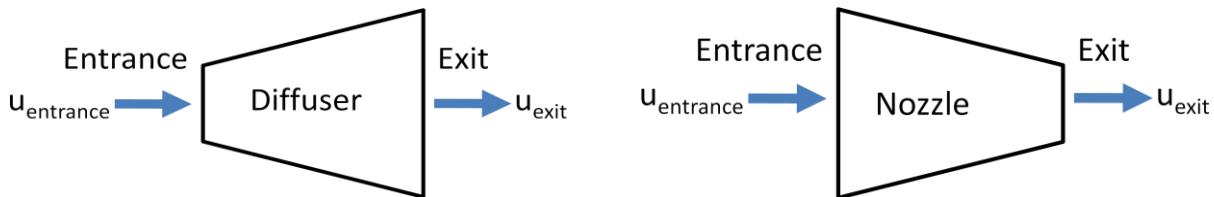


Figure 2-13: Schematic of Diffuser and Nozzle

For the diffuser case, the cross-sectional area of the entrance is less than that of the exit ($A_{entrance} < A_{exit}$); as a result, the velocity of the entrance would be greater than that of the exit ($u_{entrance} > u_{exit}$) as shown in Figure 2-13. Conversely for the nozzle case, the cross-sectional area of the entrance is greater than that of the exit ($A_{entrance} > A_{exit}$); therefore, the velocity of the entrance is less than that of the exit ($u_{entrance} < u_{exit}$). Using this phenomenon, the diffuser/nozzle can be used as a valve.

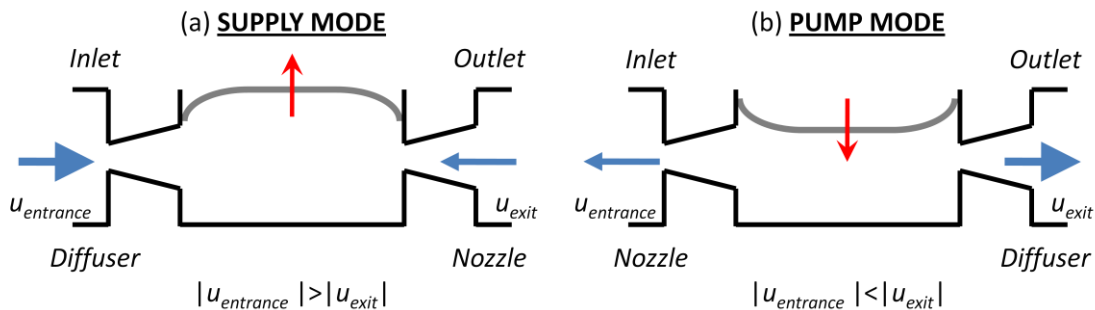


Figure 2-14: Operation of the diffuser-based pump (single-chamber and single-diaphragm): (a) Supply Mode; (b) Pump Mode [26]

As illustrated in Figure 2-14, the principle of operation for a diffuser is that during the pumping mode, fluid flows more quickly through the outlet than through the inlet. Conversely, during the supply mode, fluid flows into the chamber from the inlet opening faster than from the outlet opening. The operation of the diffuser is to transform kinetic

energy from the velocity change to the pressure change [26]. This is a result of Moody-type friction loss which is also known as minor losses due to gradual expansions or contractions [12]. Depending on the type of flow in a diffuser, the “stability” is determined by Figure 2-15. The stability map of a diffuser illustrates the effect of the geometry, which will establish the operation of flow in the diffuser. From the Figure 2-15, in the *jet flow* region, it is noticed that the diffuser almost retains constant cross-sectional area producing an ineffective diffuser. The flow separates almost entirely at the diffuser walls. In the *bi-stable steady stall* region, the flow can reverse from wall to wall of the diffuser; as a result, a poor performance diffuser is produced. Next in the *transitory steady stall* region, the flow is known to be unsteady with minimum pressure loss. Lastly, in the *no stall* region, the flow is steady and viscous without separation at the diffuser walls; hence, it performs moderately well [26].

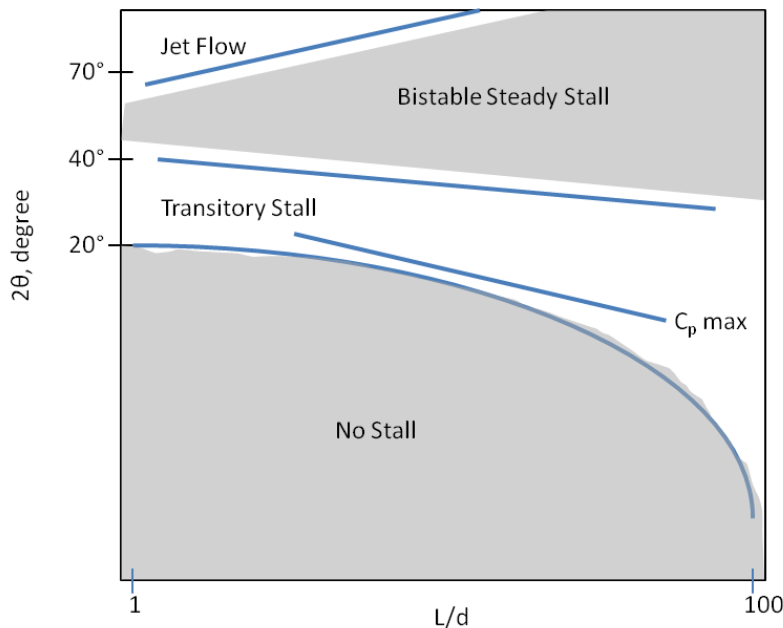


Figure 2-15: Stability map of a diffuser [26]

Both the conical and the flat-walled diffusers have similar performances; thus, the diffuser types are chosen generally by the manufacturing process [12]. However, the flat-walled diffusers are more common due to their compact design [26]. In Figure 2-16, the

flow losses in a diffuser expansion is illustrated. The loss coefficient of the diffuser is dependent on the diffuser angle.

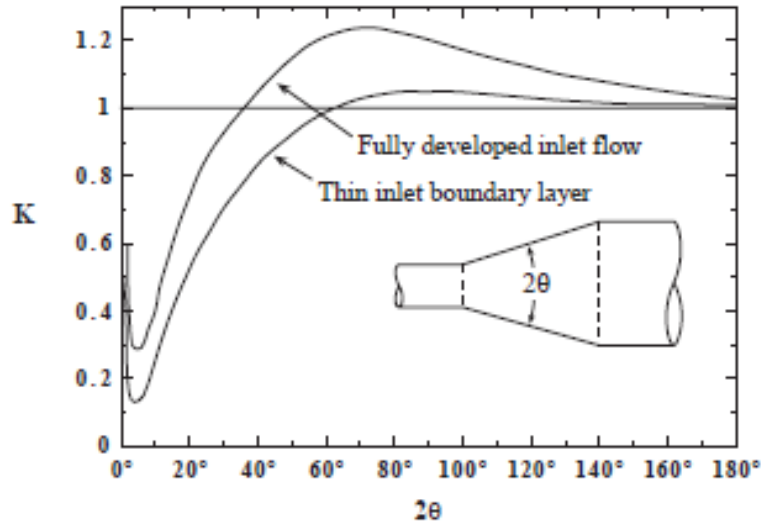


Figure 2-16: Flow losses in a gradual conical expansion region [12] [27]

The loss coefficient, K , is related to the pressure-recovery coefficient, C_p value by

$$K = 1 - \left(\frac{A_{in}}{A_{out}} \right)^2 - C_p \quad \text{Equation 2-4}$$

where A_{in} and A_{out} are the inlet and outlet cross-sectional areas of the diffuser, respectively. From Figure 2-16, the minimum loss (K) occurs when the cone angle 2θ is equal to approximately 5° . Also, the maximum loss (K) occurs between the cone angles, 2θ , of 40° to 60° . As seen in the equation above Equation 2-4, the higher the pressure recovery, the lower the loss; therefore, the pressure recovery must be maximized to produce a successful diffuser. The pressure recovery coefficient performances are in respect to the area ratio ($AR = A_{out}/A_{in}$) and the slenderness (L/W_{throat} or L/D_{throat}) as demonstrated in Figure 2-17.

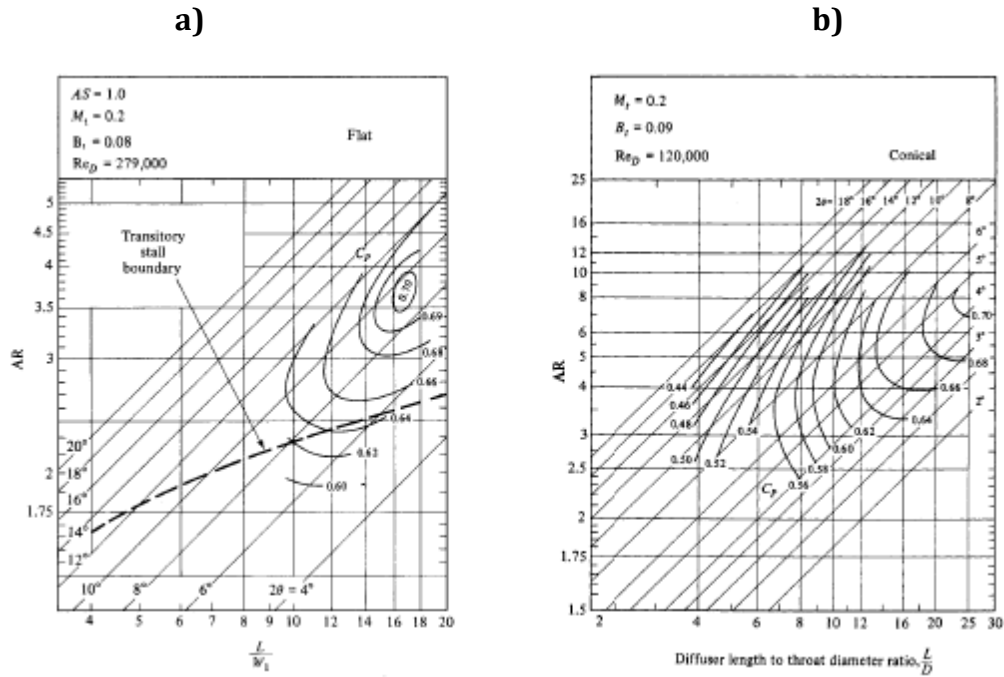


Figure 2-17: Typical performance maps for flat-wall and conical diffusers at similar operating conditions: a) flat-wall and b) conical [27]

From these design criteria, a diffuser must produce a highest possible flow directing capability to be a non-mechanical valve. The possible flow directing capability of a diffuser can be estimated by the pressure drop, Δp , in an internal flow system expressed with the loss coefficient, K :

$$\Delta p = K \cdot \frac{1}{2} \cdot \rho \cdot \bar{u}_{exit}^2 \quad \text{Equation 2-5 [26]}$$

where ρ is the fluid density and \bar{u}_{exit} is the average velocity of the exit (upstream). For more practicality, the pressure drop can be related to the velocity in the cross-section of the throat as

$$\Delta p = \xi \cdot \frac{1}{2} \cdot \rho \cdot \bar{u}_{throat}^2 \quad \text{Equation 2-6 [26]}$$

where ξ is the pressure loss coefficient and \bar{u}_{throat} is the average velocity of the throat.

The pressure loss coefficient, ξ , can be defined with loss coefficient, K as

$$\xi = K \cdot \left(\frac{A_{throat}}{A_{exit}} \right)^2 \quad \text{Equation 2-7 [26]}$$

Then the efficiency, η , can be calculated with ratio of the flow in the diffuser direction to the nozzle direction as shown in Figure 2-13:

$$\eta = \frac{\xi_{diffuser}}{\xi_{nozzle}} \quad \text{Equation 2-8 [26]}$$

where the efficiency of the diffuser (η) should be maximized to optimize the design.

As a result, the flow directing capability of a non-mechanical valve is dependent on the pressure drop across the device. This allows the device to potentially replace any check valves.

2.4.1.2 Alternative: Non-mechanical Valvular Conduit

To broaden the knowledge of non-mechanical valves, an alternate method for this process was examined. The concept of the diffuser/nozzle is to create a pressure difference such that the flow of the fluid in one direction of the channel is favored compared to the opposite. Hence, using a complex geometry, a similar idea can be enforced and can potentially be used as a non-mechanical valve.

From other non-mechanical valve research, an original design of Tesla was found known as valvular conduit as shown in Figure 2-18 [28].

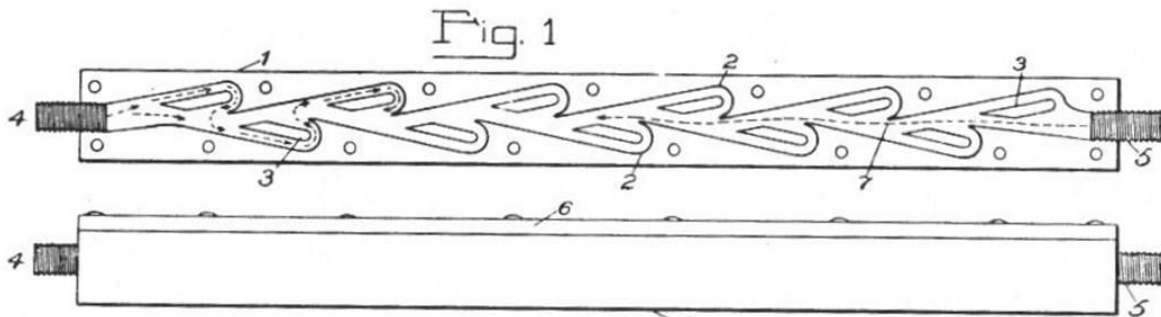


Figure 2-18: N. Tesla's original valvular conduit design [28]

There has been some research performed to optimize this valvular conduit from the geometric characteristics. The research of this valvular conduit has been limited to micro-channel applications only. Forster et al. [29] have investigated the conduit with just the two curvatures of redirecting the flow as shown in Figure 2-19.

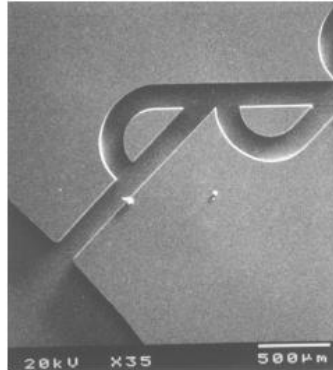


Figure 2-19: Non-mechanical Valvular Conduit [28]

According to Forster et al.'s investigation [29], the valve demonstrated viscous behavior² in the forward/positive direction and dynamic behavior³ in the reverse/negative direction. Nevertheless, Forster compared the diodicity⁴ between the diffuser and valvular conduit design and determined that the valvular conduit's performance was significantly superior due to dynamic pressure loss in one flow direction and viscous loss in the opposite direction.

From Gamboa et al.'s numerical research [30], they have taken the valvular conduit structure to be significant with a single loop of curvature as shown in Figure 2-20.

² viscous behavior: the pressure loss/resistance is mostly due to the frictional and viscous loss.

³ dynamic behavior: the pressure loss/resistance is caused by moving flow of gas or liquid

⁴diodicity: ability to pass flow in the forward direction while inhibiting flow in the reverse direction [43]

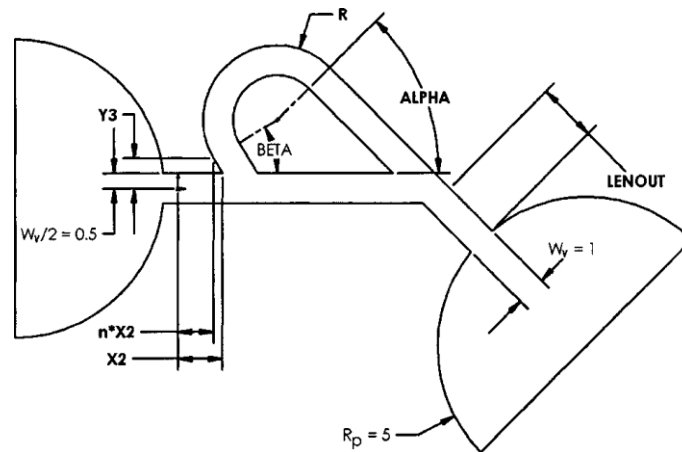


Figure 2-20: Tesla's structure investigated in Gamboa et al.'s research [30]

This research has optimized the dimension shown in Figure 2-20. Thus, the valvular conduit allows the fluid to pass in the forward direction, and prevents it from flowing in the backward direction by the geometric turbulence. The result was 25% higher ratio of reverse flow to forward flow resistance. Hence, this research can be utilized in real applications [30]. Due to a lack of research in non-mechanical valve other than for diffuser/nozzle valves, the valvular conduit was chosen to be investigated with the interest of new non-mechanical valve methodology.

Chapter 3

NUMERICAL APPROACH: MODELLING AND SIMULATION

A non-mechanical valvular conduit was studied using a numerical approach to understand the complex geometry in depth.



Figure 3-1: Non-mechanical Valvular Conduit Design for the Numerical Approach [29]

As shown in Figure 3-1, the valvular conduit is a micro-channel with curved split pathways where the fluid can flow. This conduit is open for the fluid to flow in the positive flow direction or the opposite (i.e. negative) flow direction. Figure 3-1 shows the positive flow direction which is also known as the favorable fluid flow direction. This is due to less pressure resistance the fluid experiences as it flows in the positive flow direction compared to the negative flow direction. As a result, the effectiveness of the valve can be evaluated by the pressure differences across the micro-channel conduit in the positive flow direction and in the negative flow direction.

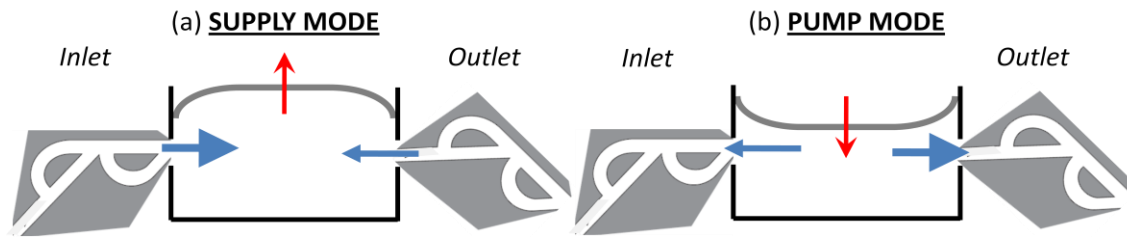


Figure 3-2: Operation of Non-mechanical Valvular Conduit on single-chamber and single-diaphragm pump: (a) Supply Mode; (b) Pump Mode

Using similar fundamentals of the diffuser/nozzle valves, the non-mechanical valvular conduit is placed at the inlet and the outlet of the diaphragm pump, as illustrated in Figure 3-2. As explained in Section 2.4.1.1, the principle of the non-mechanical valves is that the fluid will expectedly flow where the pressure resistance is minimal; thus, the valvular conduit behaves like a valve. When the diaphragm pump operates in positive stroke (b) pump mode, the fluid can flow in both forward and reverse direction as shown in Figure 3-2. However, if the valve has a greater pressure resistance in the negative flow direction, then the net flow will be in the positive flow direction (i.e. favorable direction).

The effectiveness of the complex micro-channel geometry, shown in Figure 3-1, was studied numerically using computational fluid dynamic (CFD) commercial software. From many choices of software for CFD simulation, the one selected to perform fluid-flow study was ANSYS-CFX Workbench 12.1. The software enables the user to perform a fluid-flow analysis of incompressible fluid flow in complex geometries using a high resolution scheme. First, the initial design of the valvular device was modeled using software incorporating a reliable, converging mesh. The software requires the properties of the fluid and the boundary conditions to be set for the computational simulations. The pressure drops across the micro-channel pathways for both directions were obtained from the CFD simulations. The pressure drop resulting from this analysis is the main area of interest of the numerical approach.

The pressure drop across the micro-channel generated by the inlet flow rate was obtained from the CFD study. Using these data, a mesh convergence study was performed. To investigate the performance of the complex geometry, one must alternate the flow direction of the micro-channel pathway and analyze the outcome of the results. The main purpose of the simulation was to analyze the pump-effectiveness-- more specifically, the overall flow of the valvular conduit in an oscillating flow. (See Section 3.3 for oscillating flow simulations and its parameters)

3.1 Model Description

From ANSYS-CFX Workbench 12.1, the flow of the micro-channel was investigated. As mentioned, the purpose of the numerical CFD simulation is to improve the efficiency of the valvular conduit in a micro-pump. Initially, the micro-channel in the conduit was analyzed with a single direction flow to understand the effectiveness of the geometry characteristics (e.g. the channel thickness, the radius of the curvature, and the diverging angle of the channel). Then an oscillating flow simulation was performed to observe the valvular conduit when the fluid changes direction over time, simulating the operation of a diaphragm pump. The Forster et al. [29] and Tesla's geometry design of the non-mechanical valvular conduit was slightly modified with the optimal geometry characteristics from the single direction flow analysis while maintaining the concept.

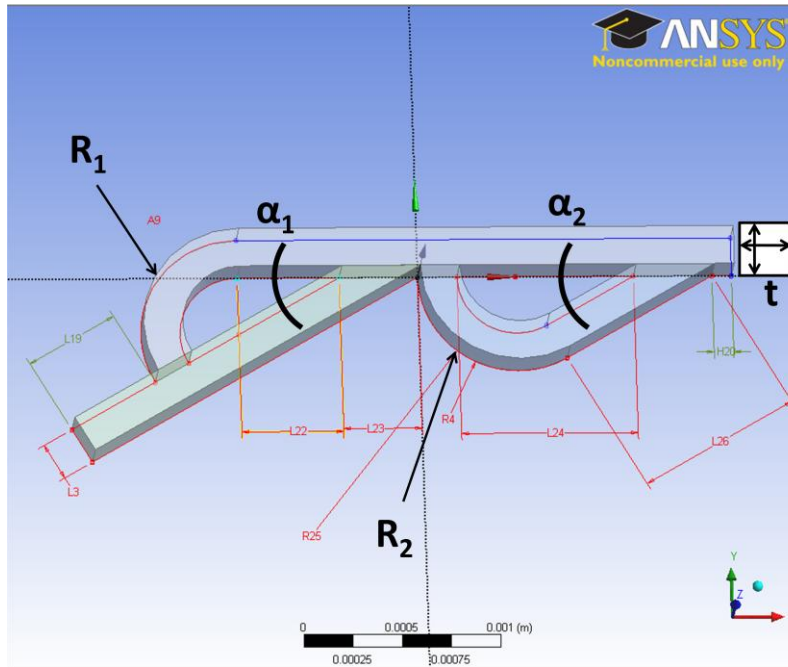


Figure 3-3: Physical domain of the valve-less design [ANSYS-CFX]

Figure 3-3 shows the layout of the geometry which was established with constant cross-sectional area throughout with a square profile and channel thickness, t . Also, the two points of curvature in the conduit (R_1 and R_2) were chosen for further investigation. In addition to that the two angles (α_1 and α_2) of the channel with respect to the horizontal channel were studied to maximize the pressure drop across the micro-channel. It was noticed that during the negative flow direction, the fluid flow would re-circulate along the curvature and as the flow entered –the angled bends the pressure flow resistance would potentially change. Hence, these parameters (i.e. channel thickness, curvature radii, and two angles) were selected to be altered to study the effectiveness and determine the best dimension for the micro-channel’s geometry. As mentioned previously, the purpose of this valvular conduit is to create maximum pressure resistance in the negative flow direction while minimizing the pressure resistance in the positive flow direction such that the net flow will be favorable in the positive flow direction. For simplicity of changing the geometric parameter, the two radii of the curvatures were maintained to be equal to each other (i.e. $R_1 = R_2$) and the two angles were kept equal (i.e. $\alpha_1 = \alpha_2$). For the numerical

simulation analysis of the valve-less conduit design, the geometrical characteristics were altered to optimize the design while keeping the entrance and the exit channel length constant. The optimization was evaluated with two methods: (1) the pressure difference, ΔP , between the pressure drop across the valvular conduit in the negative direction and the positive direction ($\Delta P = P_{negative} - P_{positive}$); and (2) the pressure ratio, PR , of the pressure drop in the negative direction to the positive direction ($PR = P_{negative}/P_{positive}$).

3.1.1 Model System Setup

3.1.1.1 Fluid Characterization

The fluid in the system was water with a temperature of 25 [°C] at atmospheric pressure (i.e. 1 [atm]). Also, constant thermodynamic properties were used during the simulations. Water is a common heat transfer fluid with a density, ρ , of 997 [kg/m³] and dynamic viscosity, μ , of $8.90 \cdot 10^{-4}$ [kg·m/s] which are values set in the ANSYS-CFX software. [31] It was assumed that the system is an incompressible and steady state flow system for optimization of the valvular conduit design. Furthermore, during the oscillating simulation, transient flow was assumed for the performance of the conduit in the pumping process. The transient flow allows the simulation to imitate the dynamic action of a diaphragm pump. When a diaphragm pump operates, the diaphragm fluctuates, changing the pressure inside the pump chamber over time as explained in Section 3.3.

First, for the optimization of the valvular conduit design, the system was assumed to be incompressible (constant fluid properties) and steady state flow. The flow model was generated using a laminar model. This is because the cross-sectional area of the channel (i.e. wetted area and hydraulic diameter, $D_h = 175$ [μm], 200 [μm], 225 [μm], and 250 [μm]) is very small. In a pipe or channel, the flow can be determined as laminar if the Reynolds number is less than 2300 [12]. By definition

$$Re = \frac{\rho_{fluid} \cdot \dot{u} \cdot D_h}{\mu_{fluid}} \quad \text{Equation 3-1 [12]}$$

where, Re is the Reynolds number, ρ_{fluid} and μ_{fluid} are the density and dynamic viscosity of the fluid, and \bar{u} is the average velocity of the fluid. The Reynolds number is directly proportional to the hydraulic diameter. Since the dimensions of the channels are in micro-scale, specifically, the channel thickness chosen was approximately 200 μm and the velocity of the fluid used was approximately 0.9565 m/s (See Section 3.1.1.2 for more details), the Reynolds number was 214.3 which does not exceed 2300.

3.1.1.2 Boundary Conditions

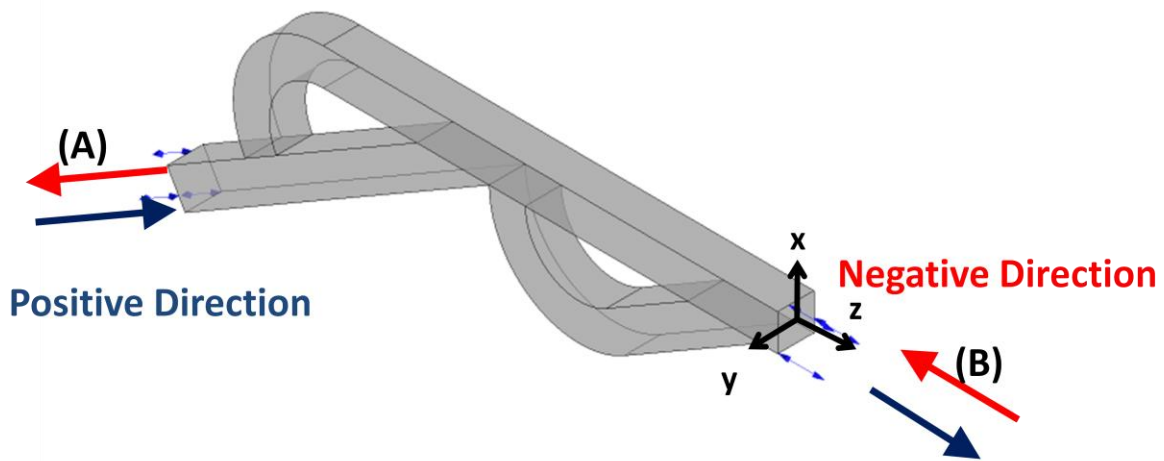


Figure 3-4: Model and Physical Domain [ANSYS-CFX [31]]

Figure 3-4 shows the schematic of the system and its physical domain. Initially, the CFD simulation was performed with the designed geometry of the micro-channel to visually observe the flow in the complex pathway. It was evident that the flow was symmetrical across the flow channel in the x-z plane according to the co-ordinates shown in Figure 3-4. A symmetry boundary condition is commonly used to reduce the mesh elements and the duration time of the simulation. However, after performing many simulations to produce a working CFD model, the mesh analysis of the CFD model was carried out without a symmetry boundary condition. Since the mesh convergence analysis was operational and successful, the computational analysis was prepared using the entire geometry as the

physical domain (See Section 3.1.2 for mesh convergence analysis) instead of utilizing the symmetry boundary condition. The wall condition of the micro-channel was considered to be a no slip wall boundary condition. In this numerical study, there were three cases: positive direction (A to B), negative direction (B to A), and oscillating flow direction. For the positive direction case, the boundary condition for the inlet and the outlet was from left to right as illustrated in Figure 3-4. Conversely for the negative direction case, the inlet and outlet boundary condition was from right to left. For both positive and negative directions, the inlet boundary condition was a normal velocity of 0.9565 [m/s] and the outlet condition was a static pressure of 0 [Pa]. The normal velocity was calculated using a similar methodology from Galvis' research [32]. Assuming that the target microprocessor is the Intel Pentium D processor from Chapter 1, the heat input is 130 [W] and the chip die size is 206 [mm²] [2]. Also, it was assumed that the wall temperature of the microprocessor is 85 [°C], which is the maximum permitted temperature of a chip according to Galvis' research [32]. With this knowledge, a micro-heat-exchanger was estimated using Galvis' program. (i.e. 35 channels, 200 x 200 [μm] cross-sections, and 200 [μm] fin spacing) [32]. As a result, the mass flux of the system was evaluated at 974 [kg/m²s] from Galvis' heat transfer calculation, which led to a corresponding normal velocity of the channel. The oscillating flow case did not have an inlet or outlet but instead opening boundary conditions for the two left and right openings.

3.1.2 Model Mesh Analysis

Initially, the valvular conduit was analyzed in CFD model to study the sensitivity of the pressure to the number of elements/nodes in the mesh of the model. From the CFD software, there are two main element types of meshing: tetrahedral and quadrilateral. Tetrahedral meshing easily fills the surface space but only contains three sided planar surface elements. Quadrilateral, however, is not so simple when implemented in the system but contains four sided planar surface elements which would provide more accurate results. Hence, when generating the mesh, quadrilateral meshing was used.

The meshing convergence criteria values were evaluated from the computer simulations with respect to pressure of the inlet and outlet of the flow with a given normal inlet velocity of 0.9565 [m/s].

3.1.2.1 Meshing Details

The main area of interest for the numerical/computational analysis was obtaining the pressure output value from the simulations. Thus, the meshing convergence criteria were made with respect to pressure values obtained from the ANSYS-CFX computer simulations. The features of the mesh trials were by trial and error as shown in Table 3-1.

Table 3-1: Meshing Trials

Meshing Features						
	<i>Meshing</i>					
	#1	#2	#3	#4	#5	#6
Element Size on Walls [mm]	0.09	0.06	0.045	0.03	0.02	0.015
Expansion Factor		1.5	1.3333	1.5	1.5	1.3333
Mesh Results						
Number of Nodes	12265	19184	26400	42845	72347	109692
Number of Elements	10470	16380	22590	36880	62650	95560

3.1.2.2 Grid Convergence Index

After the mesh features were determined, the mesh discretization analysis was performed with respect to pressure using the grid convergence index (GCI). From GCI analysis, convergence of the pressure value can be seen. Therefore, the GCI can be evaluated by minimizing estimated error (ϵ_f = estimated error in a global property of the solution) using the equation below [33]:

$$\epsilon_f \approx \frac{f(\Delta) - f(r\Delta)}{r^p - 1} \quad \text{Equation 3-2}$$

where, $f(\Delta)$ is the fine mesh result, $f(r\Delta)$ is the coarser mesh result, r is the number of control volume multiplier (mesh element multiplier), and p is the order of accuracy (for high resolution scheme $p \approx 2$ [33]). Since the main interest of the simulation is in pressure drop, the comparison between fine and coarse mesh results were performed as follows:

$$f(\Delta) - f(r\Delta) = \frac{P_{fine} - P_{coarse}}{P_{coarse}}$$

Table 3-2: Grid Convergence Index with Mesh Number

	Mesh 1	Mesh 2	Mesh 3	Mesh 4	Mesh 5	Mesh6
Number of Elements	10470	16380	22590	36880	62650	95560
Number of Nodes	12265	19184	26400	42845	72347	109692
Positive Flow Pressure [kPa]	0.37379	0.33524	0.31735	0.29652	0.27596	0.26662
Negative Flow Pressure [kPa]	0.98240	1.3689	1.4613	1.6257	1.7598	1.7502
Pressure Difference between Negative and Positive Flow [kPa]	0.60860	1.0337	1.1439	1.3292	1.4839	1.4836
	Mesh 1-2	Mesh 2-3	Mesh 3-4	Mesh 4-5	Mesh 5-6	
ϵ_f	55.9 %	13.7%	13.0%	9.31%	0.025%	

As shown and highlighted in Table 3-2, Mesh 5 has the convergent solution. The estimated error (ϵ_f) calculated from the pressure difference from the pressure drop value of the negative flow to the positive flow is minimal between Mesh 5 and Mesh 6.

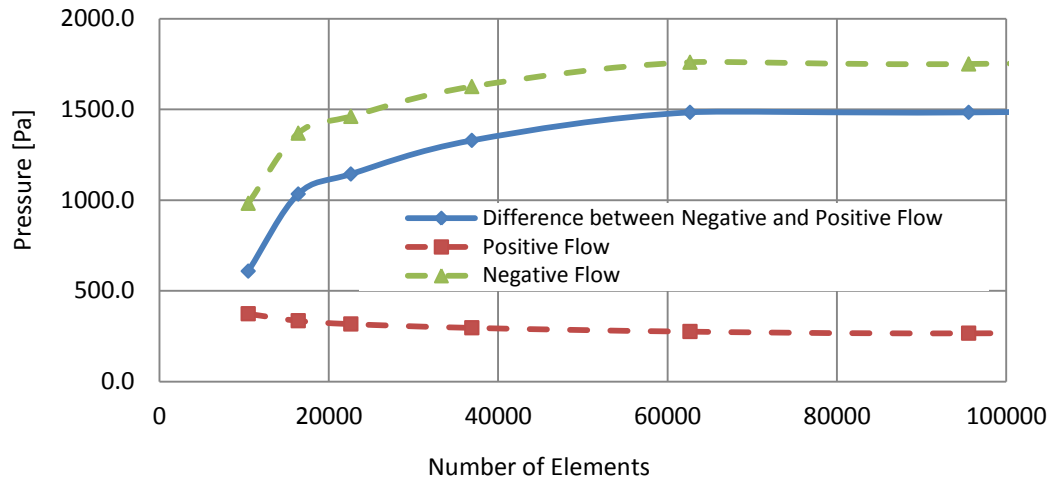


Figure 3-5: Mesh Convergence: Pressure vs. Number of Elements Plot

After grid independence analysis, the chosen meshing was Mesh 5, which produced 62,650 nodes and 72,347 elements. In Figure 3-5, the convergence is shown graphically where the mesh elements range from 60,000 to 100,000.

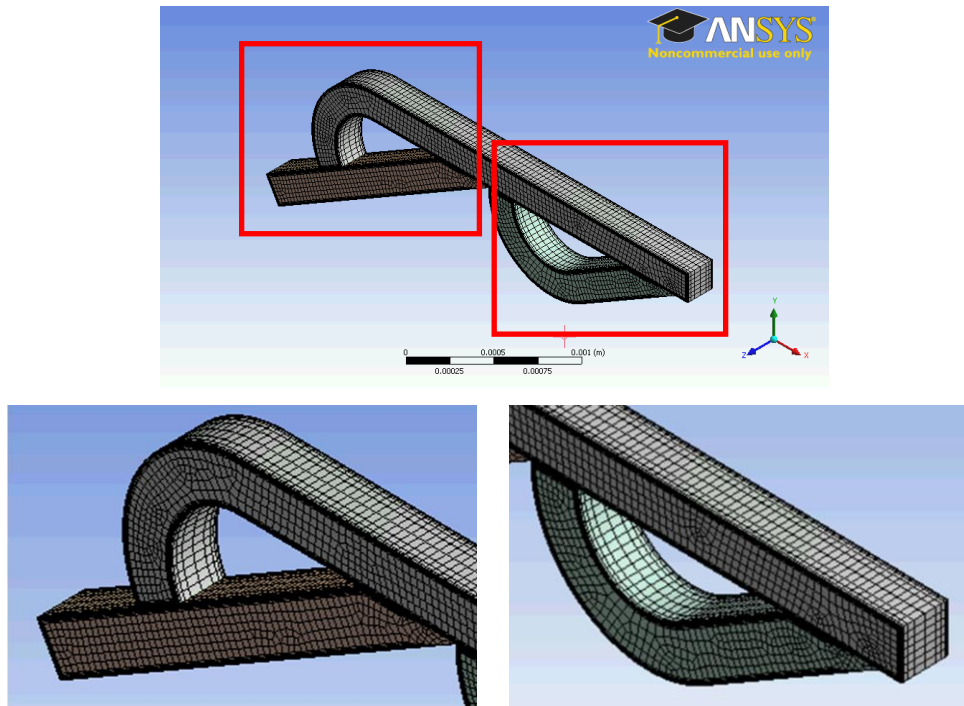


Figure 3-6: Final Mesh of the Valvular Conduit System [ANSYS-CFX]

As mentioned earlier, quadrilateral elements use four nodes of values to generate a solution while the tetrahedral elements use three nodes of values. Therefore, as shown in Figure 3-6, the mesh was created using quadrilateral elements as opposed to tetrahedral elements since quadrilateral mesh would produce more accurate results because the iterative calculation would consider a greater number of nodes.

3.2 Steady State Simulation: Optimization

With the converged mesh, different simulations were performed by altering the physical aspect of the complex conduit to observe any variance in performance (i.e. the pressure drop between the inlet and the outlet of the micro-channel) using ANSYS-CFX.

Pressure Difference Evaluated from ANSYS-CFX

Using ANSYS-CFX 12.1, the pressure values were taken from the inlet and the outlet of the micro-channel as described in Section 3.1.1.2. Despite the fact that the pressure value (i.e. area average static pressure value of 0 [Pa]) was prescribed at the outlet during the boundary condition set-up, the pressure values were still obtained from the outlet to calculate the pressure drop across the conduit design. Thus, the measured average pressure drop (ΔP) was calculated by the difference of pressure between inlet and outlet.

$$\Delta P = P_{areaavg_{inlet}} - P_{areaavg_{outlet}} \quad \text{Equation 3-3}$$

where, $P_{areaavg} = \frac{1}{A_{Total}} \iint \mathbf{P}(\mathbf{A})d\mathbf{A}$ is the area-weighted average pressure, and \mathbf{A} is the cross-sectional area.

From the evaluated pressure drop, the key physical aspects analyzed and altered were the angle of the slope in the micro-channel (α), the channel thickness (t), and the curvature radii (R) of the complex geometry as shown in Figure 3-4.

3.2.1 Angular Comparison

From the horizontal channel, there are two channels which branch off at an angle (α) as described in Section 3.1. To observe the effect of the angle in terms of the performance of the valvular conduit, several angles were simulated using the converged mesh. Angles

between $0^\circ - 90^\circ$ were studied. The allowed range of angles chosen to be simulated on the CFD software was between $5^\circ - 88^\circ$ from the horizontal axis channel. Hence, at a given parameter of channel thickness of $200\ \mu\text{m}$, curvature radii of $500\ \mu\text{m}$ and using water as fluid, the simulation analysis was performed at a provided flow rate.

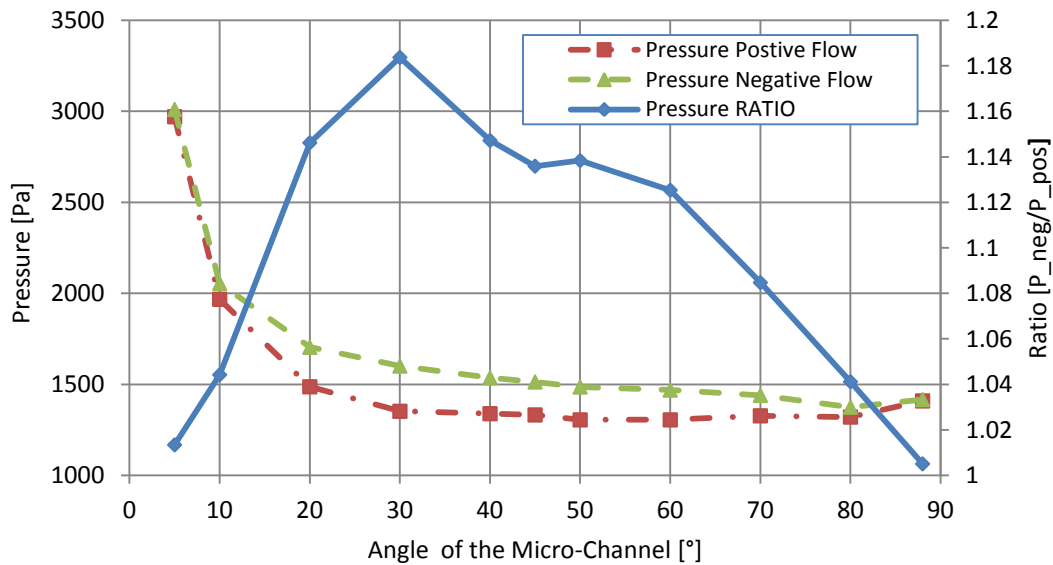


Figure 3-7 Angular Analysis for Optimization

Figure 3-7 is the angular analysis of the micro-channel valvular design, which observes the effect of pressure with respect to the angle (α). From the analysis, there is one angle which appears superior compared to the rest. As shown in Figure 3-7 secondary y-axis, at the lowest angle the pressure ratio between negative to positive flow pressure drop (i.e. PR) is almost equal to one. Similarly, at the highest angle the pressure ratio reaches a value of one. From the results, the highest pressure ratio value achieved is at 30° . Hence, the optimum angle for most effective performance of the valvular conduit is when the two branched micro-channels are at an angle of 30° from the horizontal micro-channel.

3.2.2 Channel Thickness Analysis

After the analysis of the angles, another parameter considered was modifying the micro-channel thickness without compromising the mass/volumetric flow rate. It was

assumed that the flow rate would be constant during the pumping sequence. This analysis was done to understand if changing the channel thickness would affect the performance of the valvular conduit.

The simulation was done with thicknesses ranging from 175 – 250 [μm]. Since the mass/volumetric flow rate was kept constant, the normal velocity changed according to the micro-channel thickness as listed in Table 3-3.

Table 3-3: Micro-channel thickness - normal velocity list

<i>Micro-Channel Thickness, t [μm]</i>	<i>Normal Velocity, u [m/s]</i>
175	1.2493
200	0.9565
225	0.7557
250	0.6121

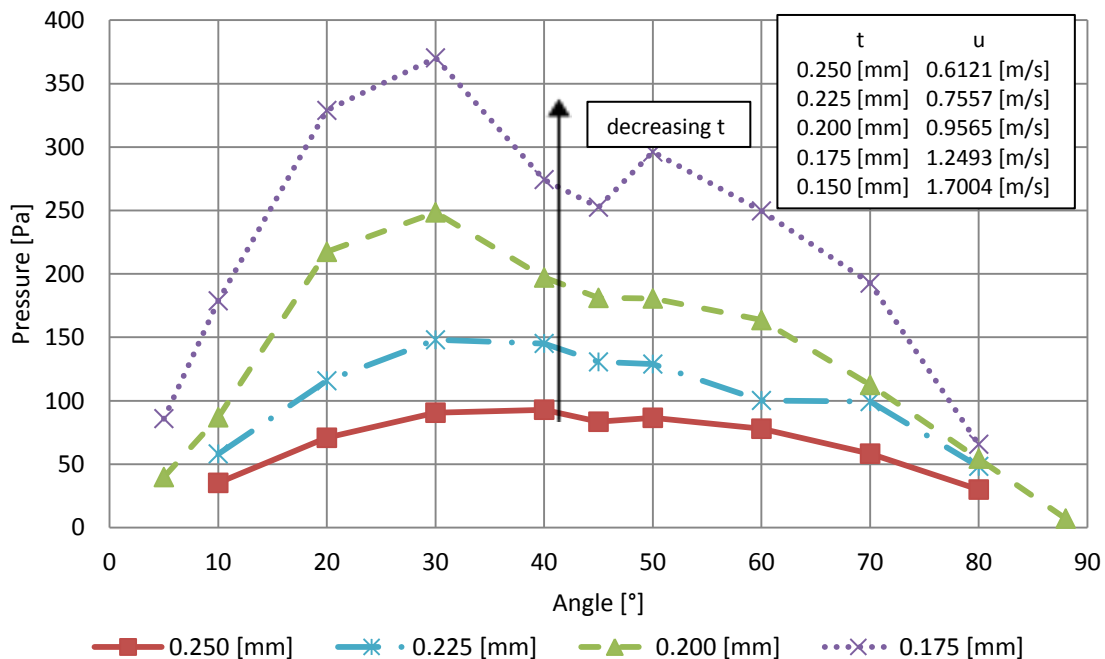


Figure 3-8: Channel thickness (t) change: Pressure difference between negative flow and positive flow at various angles of the channel

Figure 3-8 shows the pressure difference between negative flow and positive flow with respect to the angle (α). The simulations are done for four different channel thicknesses ($t = 0.250$ [mm], 0.225 [mm], 0.200 [mm], and 0.175 [mm]). It is observed that there is a direct correlation between the pressure difference and the channel thickness (t), as the thickness decreases, the pressure difference increases as shown in Figure 3-8. This was expected since a narrower channel means smaller cross-sectional area with the same constant mass flow rate would lead to a greater pressure drop and ultimately a greater pressure difference. As a result, to analyze this further, the pressure ratio of the negative and positive flow was evaluated. This is plotted with respect to angle (α) as shown in Figure 3-9.

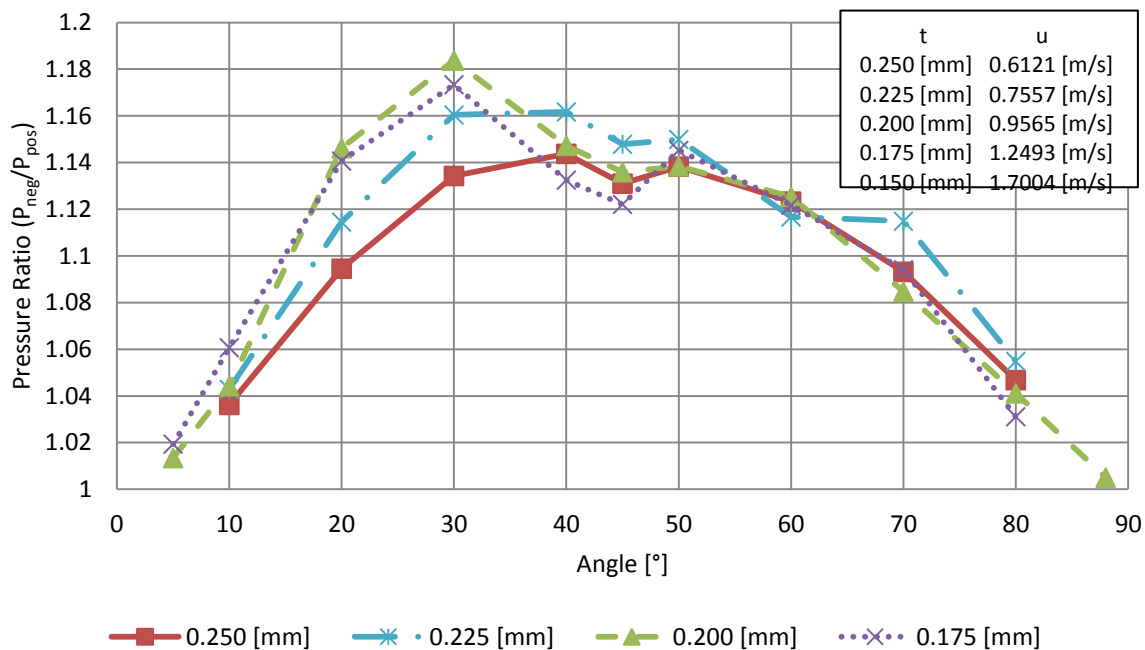


Figure 3-9: Pressure ratio analysis of the various channel thickness

Figure 3-9 illustrates that a micro-channel with thickness $200[\mu\text{m}]$ performs best compared to all other thicknesses in terms of the pressure ratio between negative to positive flow pressure drop. Therefore, the optimal channel thickness was chosen to be 200 $[\mu\text{m}]$ at 30° (optimal angle).

3.2.3 Curvature Radii of the Channel Analysis

The last feature analyzed to optimize the non-mechanical valvular conduit design was the two inner curvature radii (R_1 and R_2) indicated in Figure 3-3. For this feature, the range investigated was 0.3 – 0.7 [mm] while maintaining optimal parameters. The analysis was done in a manner similar to Section 3.2.2 by analyzing the pressure difference magnitude and the pressure ratio.

Figure 3-11 shows two plots of the pressure relation to the angle (α) with various curvatures ($R_1 = R_2 = 0.7$ [mm], 0.6 [mm], 0.5 [mm], 0.4 [mm] and 0.3 [mm]). The top plot illustrates the pressure difference between negative and positive flows with respect to the angles (α), and the bottom plot illustrates the pressure ratio with respect to the angles (α).

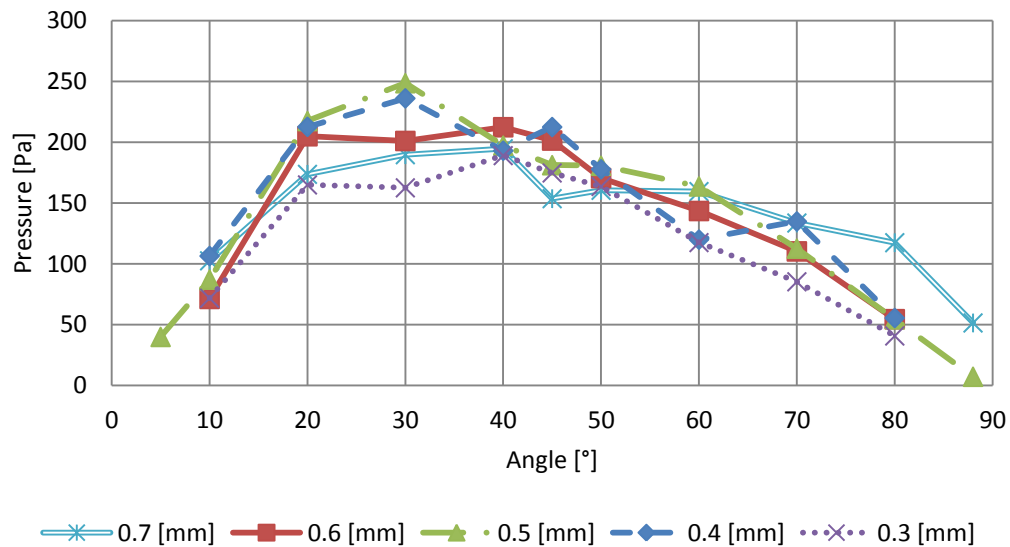


Figure 3-10: Pressure Difference at various curvature radii ($R_1 = R_2$)

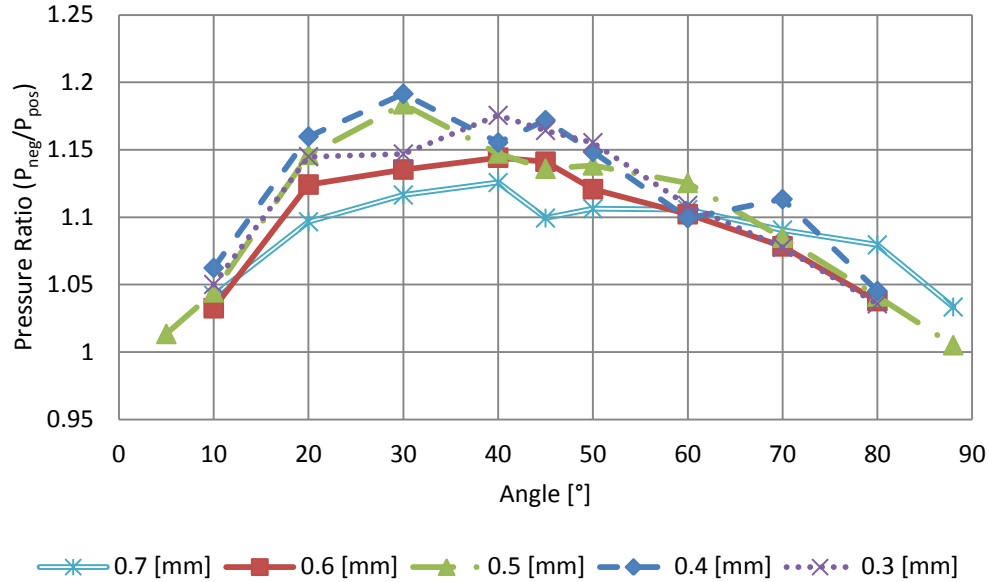


Figure 3-11: Pressure Ratio at various curvature radii ($R_1 = R_2$)

In the plot in Figure 3-11 and Figure 3-11, there are two prominent curves which demonstrate superior performance characteristics at an angle of 30°: 0.5 [mm] and 0.4 [mm]. Both curvatures have very similar performances; therefore, using either set of geometric parameters would perform optimally. In order to continue the study for the effectiveness of the geometry characteristics, the radius of curvature chosen was 0.5 [mm] since the magnitude of the pressure drop difference between negative and positive flow was greater for 0.5 [mm] than 0.4 [mm]. The greater magnitude of the pressure drop difference indicates that the negative flow pressure drop is significantly greater than the positive flow pressure drop; hence, the fluid will predominantly flow in the positive direction more for 0.5 [mm] than 0.4 [mm].

3.3 Physics behind the Valvular Conduit Design

As demonstrated in Section 3.2, the fluid flow in different direction produces different pressure drop across the conduit channel design. It is evident that the difference in the pressure drop is a result of the shape and structure of the geometrical design of the channel. Hence, the influences of the geometrical characteristics were investigated to

further understand the physics behind the conduit design using the optimized dimensions acquired from Section 3.2. Applying the hydraulic resistance calculation, the head/pressure loss (resistance), ΔH , across the channel for both the positive and the negative flow direction can be estimated [34].

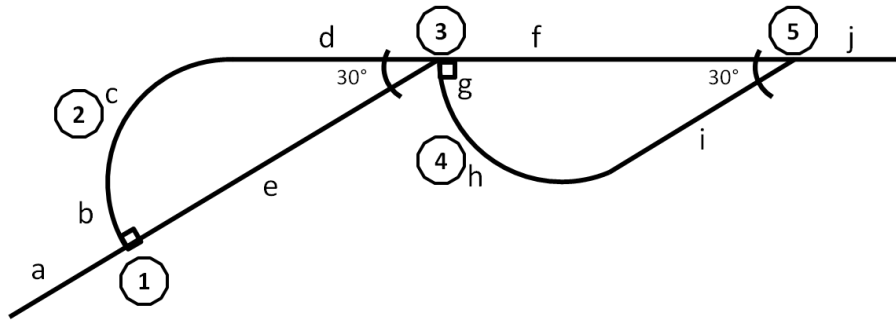


Figure 3-12: Schematic layout of the conduit design

As shown in Figure 3-12, the schematic layout of the conduit has five sections where the flow encounters pressure loss. For the positive flow direction, the flow will enter from (a) to (j); conversely, for the negative flow direction, the flow will enter from (j) to (a) in Figure 3-12. To begin the evaluation of the pressure loss, the area averaged velocity (w) of the inlet and outlet of the five sections were obtained from the ANSYS-CFX simulation listed in Table 3-4.

Table 3-4: Area averaged velocity (w) of the conduit design layout obtained from ANSYS-CFX simulation

<i>[m/s]</i>	POSITIVE FLOW	NEGATIVE FLOW	NOTES
	(a) → (j)	(j) → (a)	
$w_a = w_j$	0.9565	0.9565	$w_{in} = w_{out}$
$w_b = w_c = w_d$	0.02283	0.9565	Section (1)
$w_e = w_a - w_b$	0.9337	0.0000	$w_a = w_b + w_e$
$w_3 = w_b + w_e$ $= w_f + w_g$	0.9565	0.9565	Section (3) $w_d + w_e = w_f + w_g$
w_f	0.9565	0.6302	Section (5) $w_j = w_f + w_i$
$w_g = w_3 - w_f$ $= w_h = w_i$	0.0000	0.3263	

As shown in Table 3-4, the area averaged velocity applies to the conservation of mass. The conservation of mass states that mass-in must be equal to the mass-out (i.e.

$m_{in} = m_{out}$). Assuming that the fluid in the flow has constant thermal properties (i.e. density, ρ) throughout, then the inlet flow rate must be equal to the outlet flow rate (i.e. $Q_{in} = Q_{out}$). In addition, since the cross-sectional area of the conduit channel is constant throughout, the inlet velocity equals to the outlet velocity (i.e. $w_{in} = w_{out}$). Thus, when the flow encounters diverging and converging wye sections, such as, section (1), (3), and (5) of Figure 3-12, the sum of the area averaged diverging and converging velocities at the respective section must equal to the inlet input velocity of 0.9565 [m/s] as listed in the notes of Table 3-4.

Head/pressure loss, ΔH , then can be calculated using:

$$\Delta H_x = \xi_x \cdot \left(\frac{\rho \cdot w_x^2}{2} \right) \rightarrow \xi_x = \frac{\Delta H_x}{\left(\frac{\rho \cdot w_x^2}{2} \right)} \quad \text{Equation 3-4 [34]}$$

, which consists of the pressure resistance coefficient, ξ , the area average velocity, w , and the density of the fluid (i.e. for water at 25 [°C], $\rho = 997$ [kg/m³]). Equation 3-4 also shows the pressure resistance coefficient expression in terms of the pressure loss. Thus, the schematics of the conduit design in Figure 3-12 can be represented as Figure 3-13 in terms of pressure resistance coefficient.

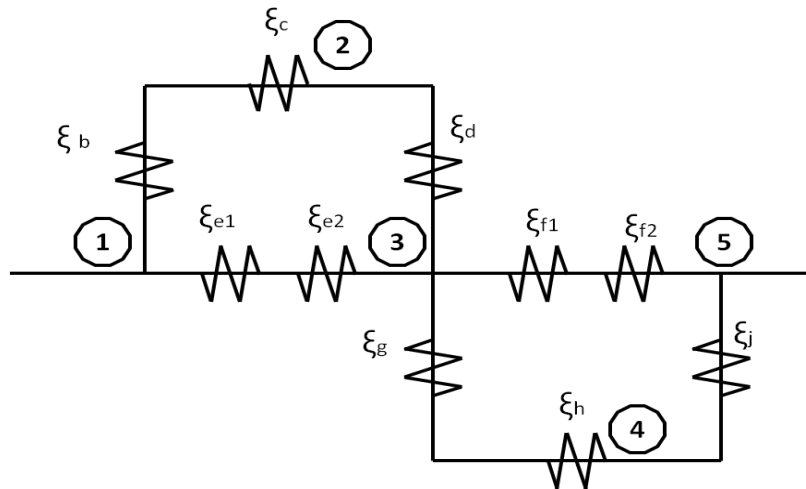


Figure 3-13: Pressure resistance circuit schematics of the conduit design

As illustrated in Figure 3-13, the pressure resistances of the conduit design are connected in series and parallel circuit. When the resistances are connected in series, the flow rate

through the channel remains constant regardless of the bends; therefore, the total head loss in that channel are the sum of pressure resistances caused by the divergence/convergence and the bend of the channel. Thus, the total pressure resistances in series can be simply the sum of the pressure resistance. However, for channels that branch out into two other channels and then rejoins at a junction (i.e. parallel channel), the total flow rate is the sum of the flow rates in the individual channels. As a result, in parallel parts of the circuit, the pressure resistance in each channel connected must be same since the change in pressure must be the same. The governing equations for parallel channels in Figure 3-12 are:

$$w_{1-3} = w_b + w_e \quad \text{where, } w_x = \sqrt{\frac{2 \cdot \Delta H_x}{\rho \cdot \xi_x}}$$

$$\sqrt{\frac{2 \cdot \Delta H_{1-3}}{\rho \cdot \xi_{1-3}}} = \sqrt{\frac{2 \cdot (\Delta H_b + \Delta H_c + \Delta H_d)}{\rho \cdot (\xi_b + \xi_c + \xi_d)}} + \sqrt{\frac{2 \cdot (\Delta H_{e1} + \Delta H_{e2})}{\rho \cdot (\xi_{e1} + \xi_{e2})}}$$

and since, $\Delta H_{1-3} = \Delta H_b + \Delta H_c + \Delta H_d = \Delta H_{e1} + \Delta H_{e2}$ with constant thermal properties therefore, the expression above simplifies to:

$$\frac{1}{\sqrt{\xi_{1-3}}} = \frac{1}{\sqrt{\xi_b + \xi_c + \xi_d}} + \frac{1}{\sqrt{\xi_{e1} + \xi_{e2}}}$$

$$\frac{1}{\sqrt{\xi_{3-5}}} = \frac{1}{\sqrt{\xi_{f1} + \xi_{f2}}} + \frac{1}{\sqrt{\xi_g + \xi_h + \xi_i}}$$

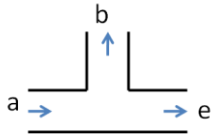
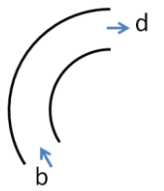
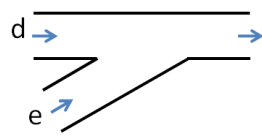
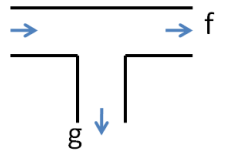
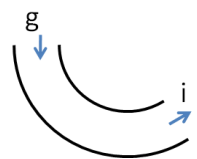
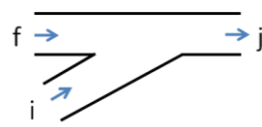
Equation 3-5

Hence, Equation 3-5 can be utilized to evaluate the pressure resistance for the parallel channels from section (1) to (3), ξ_{1-3} , and similarly, for the parallel channels from section (3) to (5), ξ_{3-5} . Then Equation 3-4 can be used to calculate the equivalent pressure loss, ΔH , for section (1) to (3), ΔH_{1-3} , and section (3) to (5), ΔH_{3-5} . The sum of the equivalent pressure loss will give the total pressure loss of the overall conduit system (i.e. $\Delta H_{\text{total}} = \Delta H_{1-3} + \Delta H_{3-5}$). This methodology of estimating the overall pressure resistance can be applied to both in the positive and negative flow directions.

3.3.1 Pressure Loss in Positive Flow Direction

In the positive flow direction, the fluid flow undergoes a pressure loss from section (1) to (5) as listed in Table 3-5. Using methodology from Idel'Chik, the pressure resistance coefficient, ξ , can be evaluated [34].

Table 3-5: Evaluation of Pressure Resistances, ξ , for Positive Flow Direction

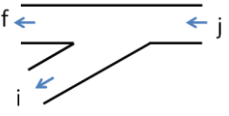
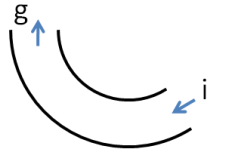
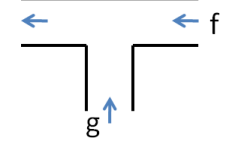
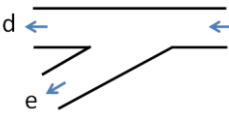
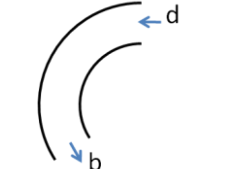
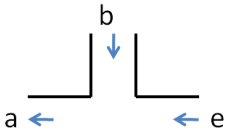
Sections	Resistance Type	Diagrams	Angle	Velocity Ratio	Pressure Resistance Coefficient
(1)	Diverging Wye		90 °	$\frac{w_b}{w_a} = 0.0239$	Branched $\xi_b = 1755$
				$\frac{w_e}{w_a} = 0.976$	Main Passage $\xi_{e1} = 0.0501$
(2)	Smooth Bends Arbitrary Angle (Low Reynolds)		60 °	N/A	$\xi_c = 13.68$
(3) a.	Converging Wye		30 °	$\frac{w_e}{w_c} = 0.976$	Branched $\xi_{e2} = 0.3159$
					Main Passage $\xi_d = -1191$
(3) b.	Diverging Wye		90 °	$\frac{w_g}{w_3} = 0$	Branched $\xi_g = 8.594$
				$\frac{w_f}{w_3} = 1$	Main Passage $\xi_{f1} = 0$
(4)	Smooth Bends Arbitrary Angle (Low Reynolds)		60 °	N/A	$\xi_h = 0$
(5)	Converging Wye		30 °	$\frac{w_i}{w_j} = 1$	Branched $\xi_i = -8.593$
					Main Passage $\xi_{f1} = 0$

After determining the pressure resistance coefficients, Equation 3-5 was applied and the total pressure loss was estimated to be 158.84 [Pa].

3.3.2 Pressure Loss in Negative Flow Direction

Correspondingly, the pressure loss in negative flow direction was calculated. From Figure 3-12, the negative flow encounters from section (5) to (1) and the pressure resistance coefficients at each section were determined as listed in Table 3-6.

Table 3-6: Evaluation of Pressure Resistances, ξ , for Negative Flow Direction

Sections	Resistance Type	Diagrams	Angle	Velocity Ratio	Pressure Resistance Coefficient
(5)	Diverging Wye		30°	$\frac{w_i}{w_j} = 0$	Branched $\xi_i = 4.560$
				$\frac{w_f}{w_j} = 1$	Main Passage $\xi_{f2} = 0.1111$
(4)	Smooth Bends Arbitrary Angle (Low Reynolds)		60°	N/A	$\xi_h = 2.427$
(3) b.	Converging Wye		90°	$\frac{w_g}{w_3} = 0.341$	Branched $\xi_g = 0.9991$
					Main Passage $\xi_{f1} = 0.9512$
(3) a.	Diverging Wye		30°	$\frac{w_e}{w_3} = 0$	Branched $\xi_{e2} = \infty$
				$\frac{w_d}{w_3} = 1$	Main Passage $\xi_d = 0$
(2)	Smooth Bends Arbitrary Angle (Low Reynolds)		60°	N/A	$\xi_c = 1.206$
(1)	Converging Wye		90°	$\frac{w_b}{w_a} = 1$	Branched $\xi_b = 1.200$
					Main Passage $\xi_{e1} = \infty$

Then the total pressure loss in the negative flow direction was estimated to be 1357.7 [Pa] which is approximately 8.55 times greater than the total pressure loss estimated for the positive flow direction. The difference between the total pressure loss in the negative and the positive flow direction is 1198.9 [Pa].

(See Appendix F for details)

3.4 Transient Method: Pumping Simulation

Using the chosen dimensions given above in Section 3.2, the pumping simulation was performed. From the previous publications, there have been experimental and simulated results on this micro-channel for steady flow, but pump simulation was untouched [26]. Knowing that the pumping simulation is due to oscillating flow, the simulation was performed using two open boundary conditions with fluctuating pressure expression. As described later, a transient approach was prepared with time dependent pressure expression. Then the outcome of the area average normal velocity-- more specifically, the volumetric flow rate--could be measured from ANSYS-CFX 12.1.

3.4.1 Transient Flow Model

For the transient simulation, certain simulation model details were augmented from the steady state simulation. The transient flow model used time-dependent fluctuating pressure at one end of the valvular conduit design geometry. Therefore, the only augmented detail was that the simulation type has been changed from steady state to transient which requires three time inputs for the simulation. First, total time is established, which is the desired amount of simulation time. Then the timestep is set for the instantaneous result at a particular time. Lastly, the initial time is set to determine, at what time the simulation begins (e.g. simulation starts at $t = 0$ [s]).

3.4.1.1 Pressure Input Expression

Before creating the transient flow model, other research papers have been reviewed. According to the research of no-moving-parts valves from Wang et al. [35], to imitate the

realistic operation of a piezo-electric buzzer driving force system, a sine wave with frequency corresponding to the different pressure energy and driving frequency are applied at the inlet of micro-channel to study the net volume flow. As mentioned in Section 2.3.2, piezoelectric diaphragm pumps can operate at a frequency of 70 – 180 [Hz]. Also according to Kang [36], a high performance check valve diaphragm micro-pump can produce a maximum backpressure of approximately 10.5 [psi] (approx. 72.4 [kPa]). With this knowledge, the pressure input expression can be derived using the frequency/period and maximum pressure:

$$P_{input} = P_{max} \cdot \sin\left(\frac{2 \cdot \pi \cdot t}{T}\right) \quad \text{Equation 3-6}$$

where, P_{input} is the pressure input expression, P_{max} is the maximum backpressure, t is the dependent variable, time, and T is the period of the oscillating.

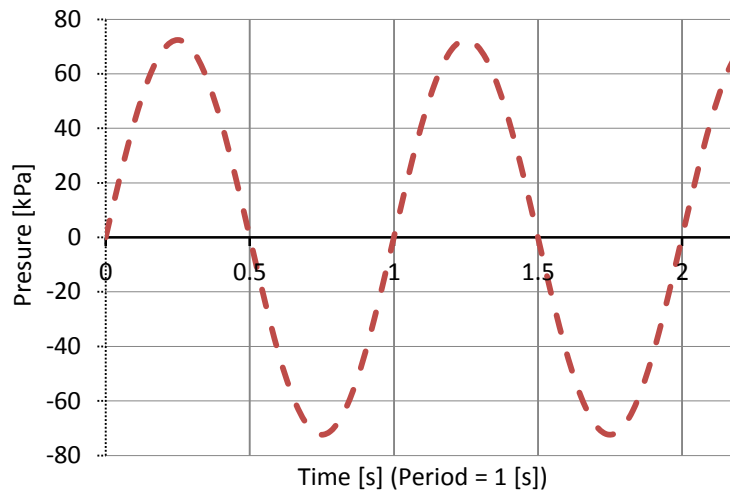


Figure 3-14: Oscillation pressure curve at Frequency 1 [Hz]

Notice that Equation 3-6 contains a sine function, which allows the pressure value to be positive and negative in an oscillating manner as shown in Figure 3-14. This will allow the flow to fluctuate from one direction to the opposite direction at a given period.

Previously for the optimization, the flow was laminar, but the transient flow was considered turbulent. During the steady state simulation, the laminar flow was assumed since the steady flow rate proved to show that the Reynolds number did not exceed Reynolds laminar standard (i.e. $Re_{sim} = 214.3 < 2300$) [12] with a maximum pressure drop across the channel of averaging approximately 3.0 [kPa]. For transient flow, to simulate the oscillation during cooling application, the fluid conditions were changed. The fluid in the system was water with temperature of 50 [°C] at atmospheric pressure (i.e. 1 [atm]). Also, constant thermodynamic properties were used during the simulations. At 50 [°C], the thermodynamic properties for water changed with a density, ρ , of 988.1 [kg/m³] and dynamic viscosity, μ , of $5.47 \cdot 10^{-4}$ [kg·m/s] which are values from Cengel et al. [6]. From the initial transient simulation with 72.4 [kPa] pressure input at time period of 30 [s], the flow produced maximum velocity of 9.89 [m/s]: hence, the Reynolds number was evaluated to be 3572.9. At this velocity, the flow is characterized as a transitional flow (i.e. $2300 < Re < 4000$). Since ANSYS-CFX software cannot simulate the transitional flow and the valvular conduit causes geometric turbulences [37], it was assumed to be turbulent flow in system. Solving turbulent flow, k-epsilon was chosen from ANSYS-CFX 12.1 CFD software with an assumed intensity of 5% which is the standard setting used [33].

3.4.1.2 Boundary Condition Change for Transient Flow

The steady state boundary condition has been changed for the transient flow simulations. Instead of assigning an inlet and outlet boundary condition as shown in Figure 3-4, the micro-channel in transient flow has two openings on both sides. This permits the fluid to flow bi-directionally as opposed to the steady state case where the fluid can only flow in one direction based on the determined flow direction. The opening boundary conditions are programmed with subsonic flow regime⁵. The difference between the inlet and outlet is that the inlet has a pressure input expression (P_{input}) and the outlet has zero relative pressure. The normal velocity can be observed from the simulated results to understand the overall flow of the valvular conduit design and its effectiveness.

⁵ subsonic flow - a low-speed fluid

(See Appendix A for detailed Flow Model and Boundary Conditions)

3.4.2 Transient Flow Results

For the transient flow of the valvular conduit, various periods (T) have been considered for the CFD simulation as listed in Table 3-7. The total duration time was set to approximately 200 % of the period to observe the transition from a full period to the next.

Table 3-7: Pressure input expression Setup for ANSYS-CFX

ANSYS-CFX Expression						
Maximum Pressure (P_max)	72.4 [kPa]					
Period (T) [s]	30	1	0.2	0.1	0.02	0.01
Total Duration Time (t_total) [s]	50	2.2	0.5	0.225	0.045	0.0225
Pressure input (P_in)	P_max*sin(2*pi*t/period)					

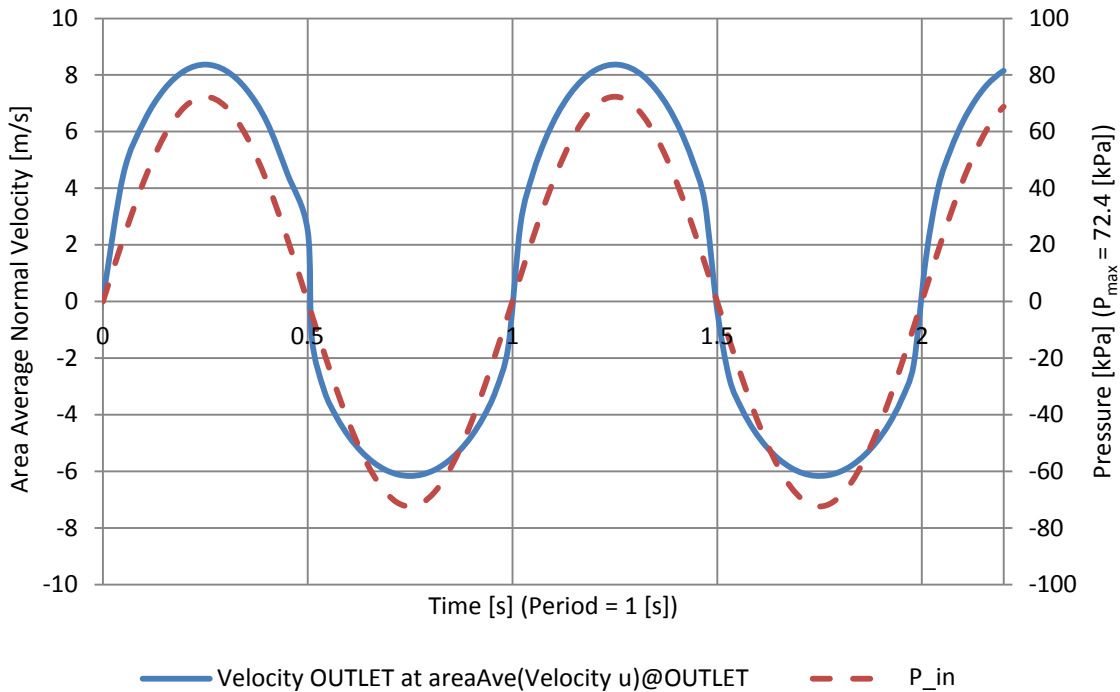


Figure 3-15: Oscillating Pressure and Velocity over time at Frequency 1 [Hz]

Figure 3-15 is the plot of outlet normal velocity profile for one second period (i.e. 1 [Hz]). At a 100 [Hz] frequency of oscillation, another plot of normal velocity profile is displayed in Figure 3-16. Many transient simulations were performed at various periods/frequencies: 30 [s]/0.03 [Hz], 1 [s]/1 [Hz], 0.2 [s]/5 [Hz], 0.1 [s]/10 [Hz], 0.02 [s]/50 [Hz], and 0.01 [s]/100 [Hz]. (See Appendix A for more plots)

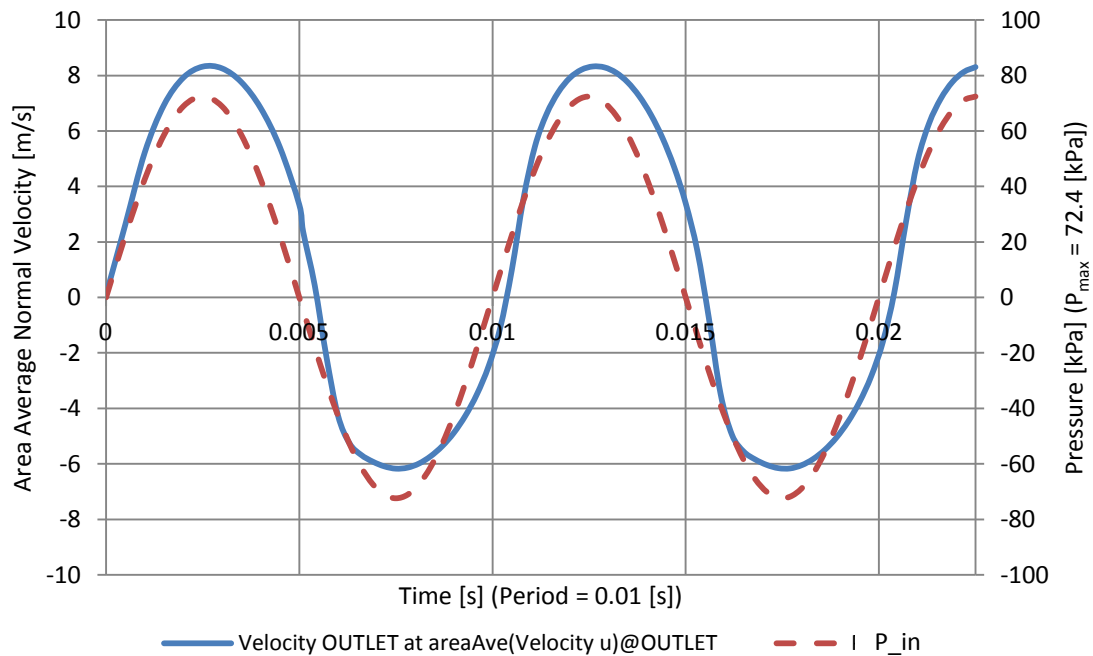


Figure 3-16: Oscillating Pressure and Velocity over time at Frequency 100 [Hz]

At all the various periods studied, the profile and the characteristics were very similar to the velocity profile at frequency 1 [Hz] and 100 [Hz] are illustrated in Figure 3-15 and Figure 3-16. From simulated results, as the pressure oscillates in a sinusoidal manner as expected and the normal velocity measured at the outlet produces an oscillating profile with favoring one direction more than the other. This favoritism is towards the positive flow direction. From both Figure 3-15 and Figure 3-16, the positive flow side amplitude of the velocity profile is approximately 25 % greater integral than that of the negative side

amplitude. Hence, as the flow accumulates over a long period of time the fluid would be transferred to the positive flow direction. The effectiveness of various time periods was compared by calculating the total volumetric flow rate over a single period. The Section 5.1.3: Evaluation of the Micro-valve (Transient Results) further discusses the effectiveness which proves that the valvular conduit design has the potential to function as a check valve.

Chapter 4

EXPERIMENTAL APPROACH

The numerical approach demonstrated great potential for the valvular conduit design. Therefore, the next step was to create a prototype to perform actual experiments for the conduit design. Using Tesla's design [28], the non-mechanical valvular conduit design was fabricated and tested. The main intention of this chapter is to experimentally demonstrate that the valvular conduit design with improved geometrical dimensions (from the numerical approach) behaves like a non-mechanical valve (e.g. nozzle/diffuser). As mentioned previously in Chapter 3, valve behavior depends on the pressure difference across the micro-channel conduit design in both the positive and negative flow direction. The principle is that the fluid flow favors a flow direction with least flow resistance. Thus, once the prototype was made, it was tested for the pressure drop across the micro-channel in both the positive and negative flow direction to determine the effectiveness of the conduit design.

4.1 Experimental Setup/Test Rig Design

To test the non-mechanical valvular conduit design an experimental setup/test rig was designed. The primary purpose of the test rig was to measure the gauge pressure drop of the valvular conduit design for both cases: the positive flow direction and the negative flow direction. The outlet gauge pressure was expected to be atmospheric pressure because the outlet was connected to the atmosphere; thus, the gauge pressure reading was approximately zero; nevertheless, the pressure sensor (transducer) was connected to both inlet and the outlet of the micro-channel design. Figure 4-1 shows the arrangements of the apparatus for the test rig design.

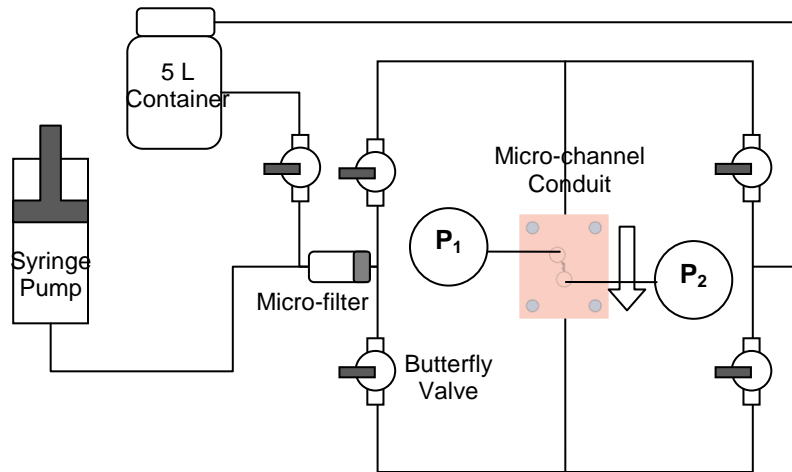


Figure 4-1: Test rig design of the fluid flow circuit

For the experimental setup, the following list is the apparatus for the experiment rig design:

- HARVARD Apparatus PHD 22/2000 Syringe Pump
 - 140 [mL] syringes ; ID 38.4[mm] (Quantity: 2)
- Micro filter
- Butterfly valves (Quantity:5)
- 1/4" OD, 1/8" ID Plastic and rubber tubing (10 ft. length)
- 5 [L] container
- PX26 Series pressure transducers 30[PSIG]
 - FLUKE Digital Model 187 Multimeter (to measure the voltage signals)
- Prototype of the valvular micro-channel conduit
 - Prototype header (cover)

This test rig required a syringe pump (HARVARD Apparatus PHD 22/2000) for the consistent flow that it could provide and capability to overcome high backpressure. Also, it required a micro filter before the fluid enters the micro-valve because any scrap particles could clog the channels. In addition, a long plastic rubber tube for the fluid flow circuit cycle and a 5 [L] reservoir container is utilized.

The test rig was designed so that the syringe pump supplies the fluid in both positive and negative flow directions of the micro-valve as illustrated in Figure 4-2 and Figure 4-3 using butterfly valves. While infusing in a positive flow direction of the micro-valve at a specific flow rate, the butterfly valves directed the necessary fluid flow through the valve and the measurement of the steady state inlet pressure (P_1) and outlet pressure (P_2) are attained. From the illustration Figure 4-2, the outlet was exposed to the container (i.e. atmosphere) so P_2 (gauge) was approximately zero.

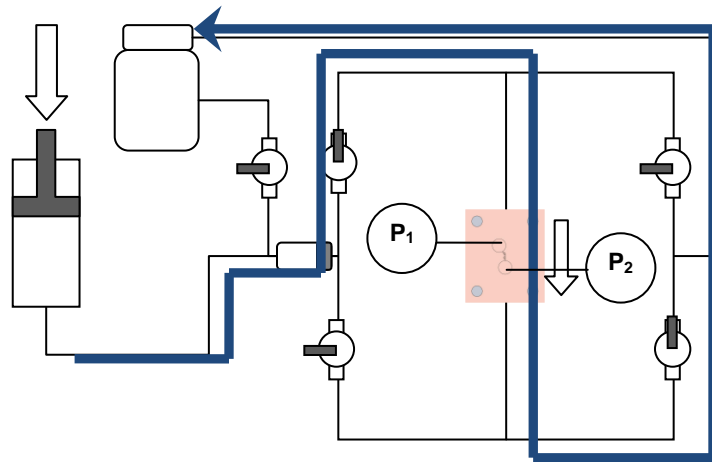


Figure 4-2: Infusing in POSITIVE flow direction at a specified volumetric flow rate

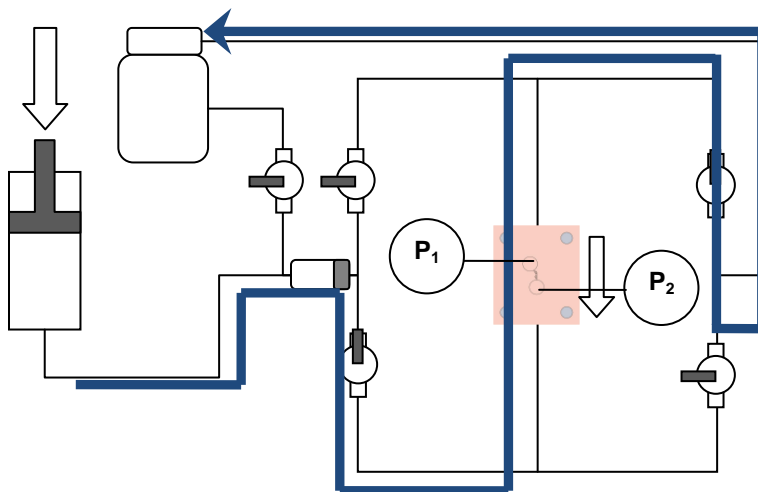


Figure 4-3: Infusing in NEGATIVE flow direction at a specified volumetric flow rate

During infusing in the negative flow direction, the butterfly valves re-directed the fluid to enter in the opposite direction. This allowed to measure the inlet pressure (P_2) and outlet pressure (P_1) using the pressure transducer in reverse order. For this case the atmosphere was exposed to P_1 according to Figure 4-3.

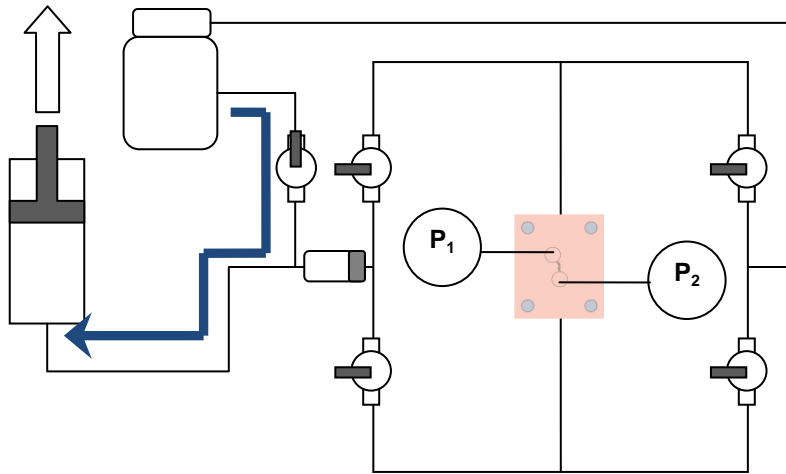


Figure 4-4: Refilling the syringes

Then by closing butterfly valves of all the circuits connecting to the valvular conduit, the syringe can be refilled from the reservoir container as demonstrated in Figure 4-4. The actual test rig setup is displayed in Figure 4-5.

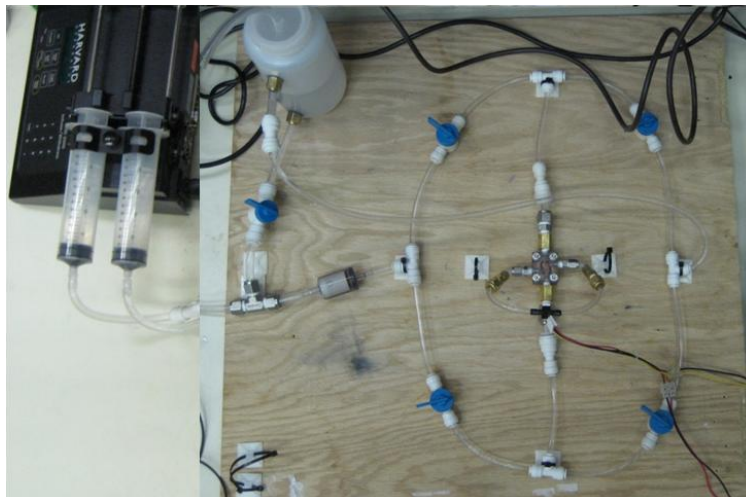


Figure 4-5: Actual Test Rig for the Experiment

4.2 Prototype Design and Manufacture

One of the main components of the test rig was the fabricated prototype design of the valvular conduit design based on measurements attained from numerical simulations. The prototype valve, as shown in Figure 4-6, was used to demonstrate the functionality of the valve and to validate ANSYS flow performance predictions.

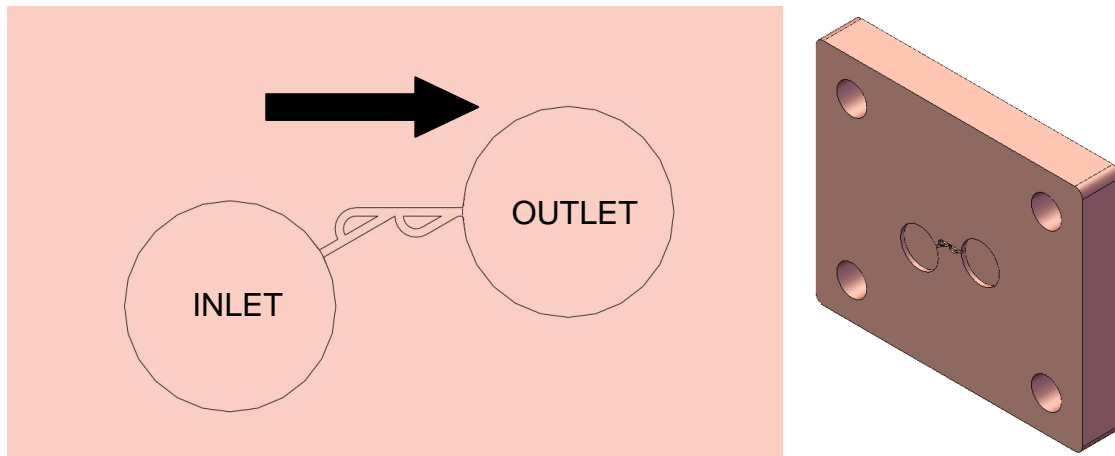


Figure 4-6: General geometry of a valvular conduit with the flow direction indication

Figure 4-6 is a schematic of the general geometry of a valvular conduit design for a diaphragm pump using SolidWorks 2009 CAD software. The flow geometry was arranged such that when the flow enters the inlet reservoir a uniform flow enters the valvular conduit design and exits to the outlet reservoir with minimum air bubbles. The inlet and outlet reservoirs are cylindrical containers which fill with fluid before the fluid enters the valvular conduit design. (See Appendix B for actual CAD drawing of the conduit design)

Following this prototype, the cover was designed such that it allows the fluid to enter according to the intentions of the test rig design such that the flow can enter from both positive and negative flow direction, and where pressure can be measured.

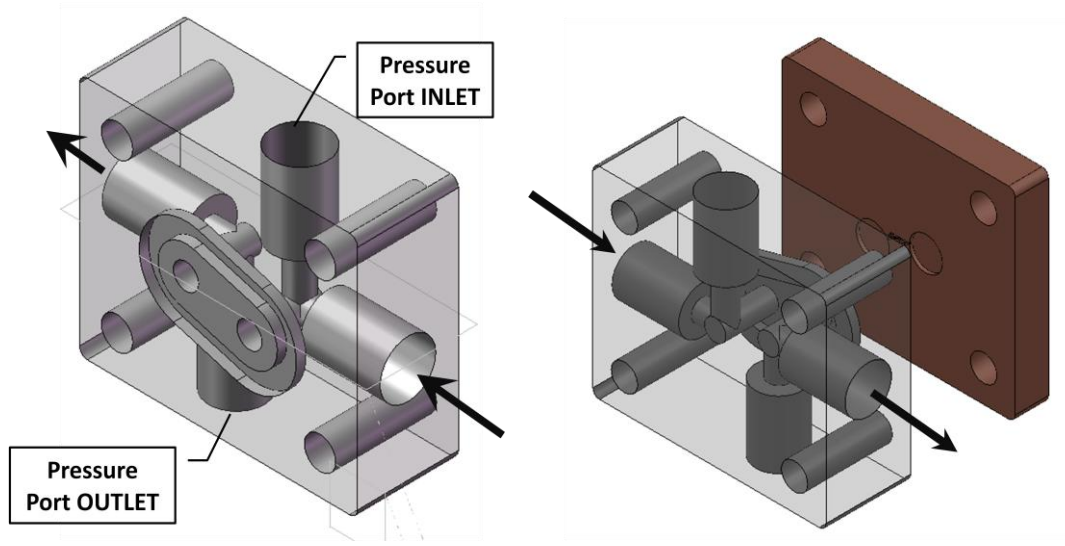


Figure 4-7: Cover Design (LEFT); Exploded View (RIGHT)

Figure 4-7 indicates the positive flow direction with arrows and the ports for the pressure sensors. The flow enters and the pressure meter is attached at the both openings of the valvular conduit such that accurate results can be attained. Also, the cover design has a 5/8" O-ring groove to prevent the fluid from any leakage. (See Appendix B for actual CAD drawing of the cover design)

4.2.1 Design Fabrication

Before building the prototype, both the materials of the valvular conduit and cover designs and the fluid were determined. The fluid chosen for the experiment was distilled water. The material for the valvular conduit was oxygen-free copper to minimize the metal from oxidizing and reacting with water. Also, the cover was fabricated with Lexan so that it would be both strong enough to attach fittings and transparent to visually observe the flow of the complex micro-channel valve. The cover design was fabricated using a computer numerical control (CNC) milling machine. Similarly, for the construction of the valvular conduit design, a CNC micro-milling machine was programmed and used due to micro-size measurements.

The valvular conduit design was constructed using an ATOMETRIC G4-ULTRA CNC machine with Master-CAM programming shown in Figure 4-8. The ATOMETRIC G4-ULTRA CNC is a five axes micro-mill machine. This micro-mill machine has a maximum accuracy tolerance of 0.6 [μm] to position and 2 [μm] along the dynamic path [38].

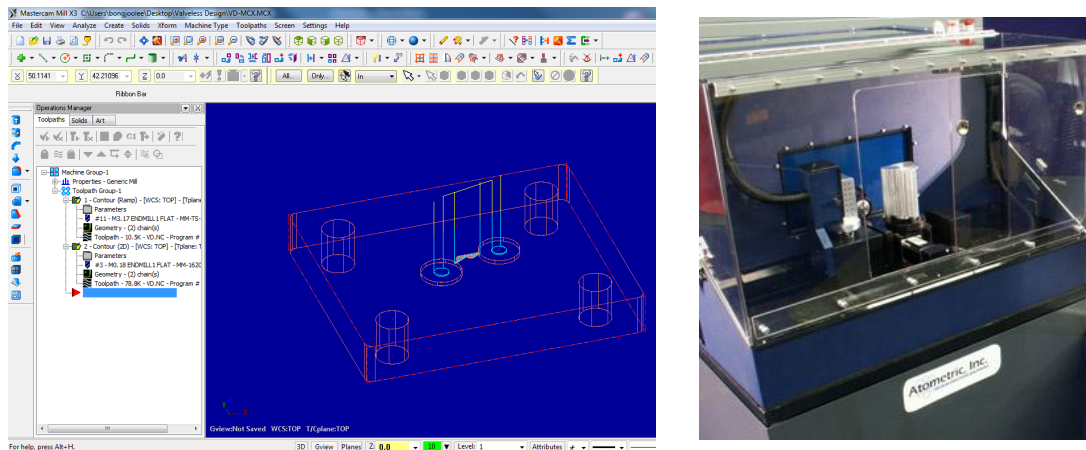


Figure 4-8: Master-CAM screen shot (LEFT); Atometric G4-ULTRA CNC (RIGHT)

This micro-mill machine allows micro-scale parts to be cut after being programmed in Master-CAM. The micro-end mill bits are very fragile since the tool bit diameter used to cut the micro-channel was 0.1778 [μm] and the tool bit diameter used to cut the two cylindrical reservoir was 3.175 [mm]. The technique is to set a low feed rate (100 mm/min) and a very high rotation rate (10,000-30,000 RPM) so that the micro-end mill bit does not get damaged. Since the micro-channel is very fine and requires accurate measurements, planarization was employed to the copper block before cutting the micro-channel groove. Planarization would reduce any cutting discrepancy during the micro-channel incision and produce more consistent channel depth. (See Appendix C for CAM program code in details)

4.2.2 Actual Manufactured of the Prototype

Inputting the Master-CAM program into the Atometric G4-ULTRA CNC, the actual prototype was built as shown in Figure 4-9. The part was polished with a fine polish cylinder block so that the micro-channel would be free of any debris and would produce accurate results.

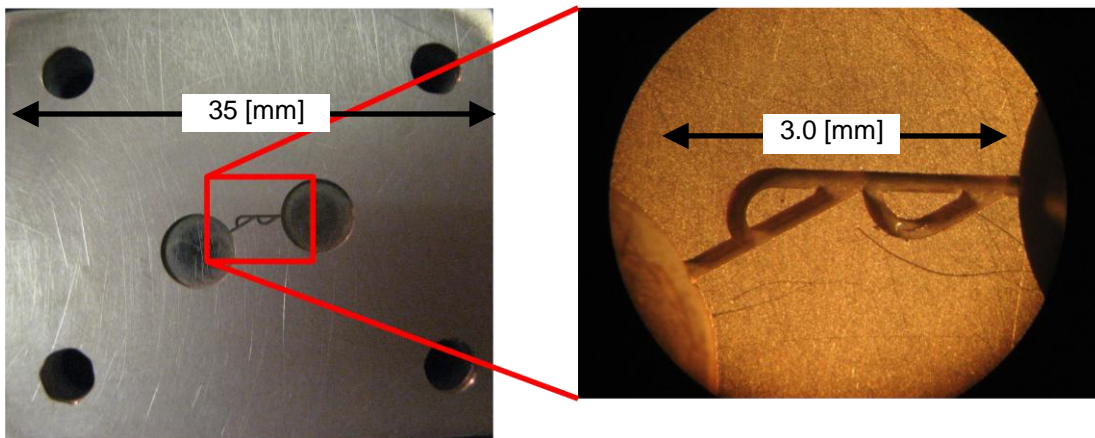
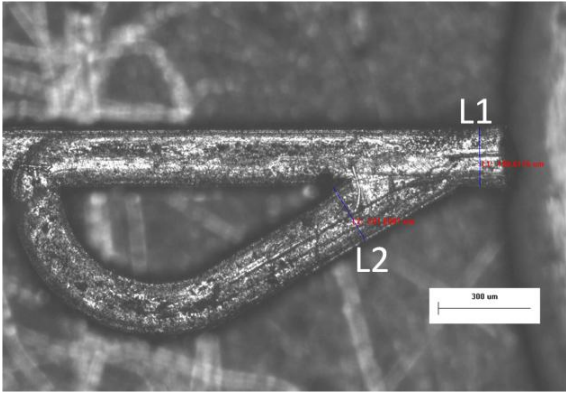
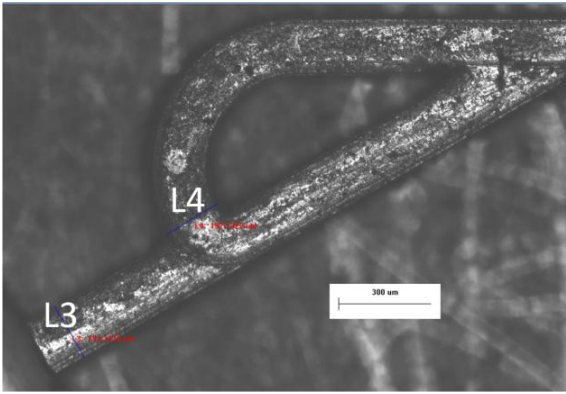
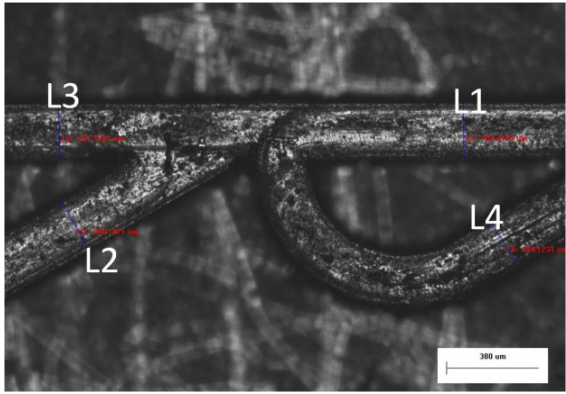


Figure 4-9: Fabricated prototype of the valvular conduit design

Using an electron microscope, the valvular conduit design prototype was measured to compare with the computer aided design (CAD) drawing. The images were at a preview resolution of 682 X 512 pixels from a Q-Imaging Digital Camera with the Image-Pro MC software program. Since the imaging software does not recognize the edges of the complex micro-channel, the measurements in Table 4-1 are approximate readings performed by the user.

Table 4-1: Actual approximate measurements from microscope software

				Features	Value [μm]	Min. Tol. [μm]	Max. Tol. [μm]
				L1	190.6	-0.001	0.001
				L2	201.7	-0.001	0.001
Features	Value [μm]	Min. Tol. [μm]	Max. Tol. [μm]				
L3	193.4	-0.001	0.001				
L4	192.1	-0.001	0.001				
				Features	Value [μm]	Min. Tol. [μm]	Max. Tol. [μm]
				L1	183.4	-0.001	0.001
				L2	189.1	-0.001	0.001
				L3	181.8	-0.001	0.001
				L4	184.1	-0.001	0.001

From Table 4-1, it is evident that the measurements are accurate. From the entrance and the exit of the micro-channel, the dimensions deviate by approximately 4.7 % maximum from the 200 [μm] channel thickness. This was expected since the Atometric

micro-milling machine has a tolerance of 2 [μm] and the actual measurement reading was done with the naked eye. The mid-section, however, has a measurement that differs approximately 18.2 [μm] from the designed dimension. Hence, this may cause some variance in the experimental results compared to the numerical results.

4.3 Test Rig Results

The experiment was set at volumetric flow rates of 5 [ml/min], 10 [ml/min], 15 [ml/min], 20 [ml/min], and 25 [ml/min] for both positive and negative flow direction. The HARVARD Apparatus PHD 22/2000 Syringe Pump can be programmed to supply fluid at a specified input flow rate in ml/min until a specified volume is reached. Afterward, the pressure measurements were taken as shown in Figure 4-2 and Figure 4-3. The PX26 Series pressure transducer was used to measure the pressure drop from the inlet to the outlet of the micro-channel valve. NOTE: HARVARD Apparatus PHD 22/2000 Syringe Pump has 1 % accuracy tolerance and PX 26 has 1 % full scale tolerance (i.e. 0.3 [PSIG] (2.068 [kPa])).

Table 4-2: Experimental Results from the Test Rig

Flow Rate		Positive Flow	Negative Flow
[ml/min]	[mm³/s]	[kPa]	[kPa]
5	83.33	8.301	10.45
10	166.7	23.99	36.48
15	250.0	46.72	63.91
20	333.3	76.12	104.2
25	416.7	113.1	179.4

4.3.1.1 Uncertainty Analysis of the Experimental Results

The uncertainty analysis of the experiment was performed to better understand any discrepancy of the experimental equipment and the results. (See Appendix E) Due to the pressure sensor (PX26 transducer) and the voltage reader (FLUKE multimeter), the pressure measurements from the experimental results yielded approximately 1.0003 % of

uncertainty. Also, the flow rate (HARVARD Apparatus PHD 22/2000 Syringe Pump and Atometric G4-ULTRA CNC machine) that is produced and measured have approximately 7.76 % of uncertainty due to the HARVARD syringe pump and the inaccuracy tolerance in Atometric micro-milling machine.

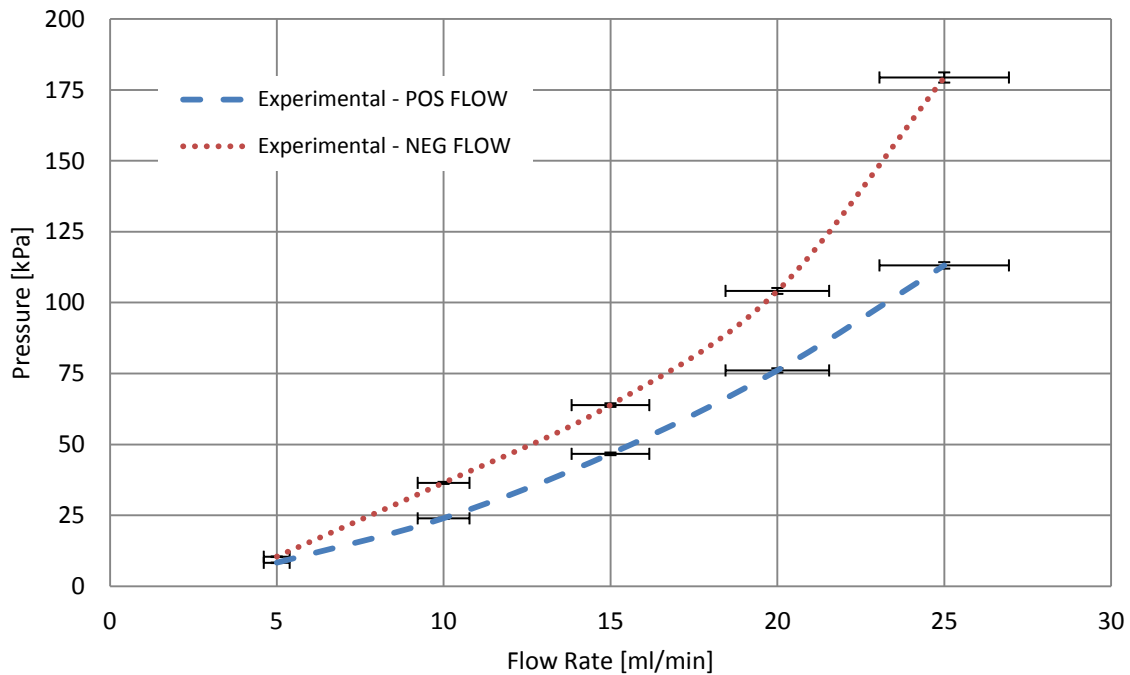


Figure 4-10: Experimental results with uncertainty analysis

Both plots of the positive and negative flow seem to increase in pressure drop across the channel at a cubic growth rate as the flow rate increase. In Figure 4-10, as expected, the negative flow direction produces higher pressure drop than of the positive flow direction. This confirms the effectiveness and the purpose of the valvular conduit. Since the negative flow direction produces great pressure drop/resistance than of the positive flow, when placed as a valve, the fluid in the positive direction, which is more favorable.

Figure 4-10 is a plot of pressure versus flow rate for averaged experimental results when the uncertainty analysis of the experiment was considered. As illustrated in Figure 4-10, the uncertainty of the flow rate was significantly greater than the pressure measurement uncertainty; therefore, the uncertainty of the pressure readings from the

experiments is negligible. Thus, the overall uncertainty of the final experimental results is from the flow rate of 7.76 %.

Chapter 5

RESULTS and DISCUSSIONS

The redesign and testing of the valvular conduit has resulted in an improved design that can be incorporated as part of a low profile, diaphragm pump for use in forced, liquid convection cooling. Previous studies have focused on the testing of the valve in isolation but not for pumping applications where they are used to replace mechanical check valves. The following section will examine the relationship between experimental results obtained using the prototype developed in the previous section and compare actual performance results to simulated results from numerical studies. The performance characteristics of the valve will be discussed along with an explanation of physical behavior of the valve subject to various boundary conditions. Finally an assessment of the types of flow conditions where this valve is most suited will be presented.

5.1 Simulated results

The numerical simulations were performed using ANSYS-CFX Workbench with a steady state and a transient model. From Section 3.2, the steady state analysis was performed to gain insight into the flow dynamics of the complex micro-channel geometry and to ascertain under which conditions optimum behavior could be achieved.

5.1.1 Visual Observation from Numerical Study

The numerical simulation was used to perform a preliminary visual analysis of the operation of the valvular conduit operation. The purpose of the intricate geometry of the valvular conduit design was to generate greater pressure resistance in one direction compared to the other. Given the larger resistance to fluid flow in the negative flow direction, the valvular conduit has the potential to operate as a check valve in an oscillating flow scenario, such as in a diaphragm pump.

Using the flow conditions from section 3.1.1, the CFD simulations were performed for both positive and negative flow direction of the conduit design. The velocity field through

the mid-section of the micro-channel, shown in Figure 5-1, indicates that there is acceleration of the fluid at three particular segments where the channel diverges and changes direction.

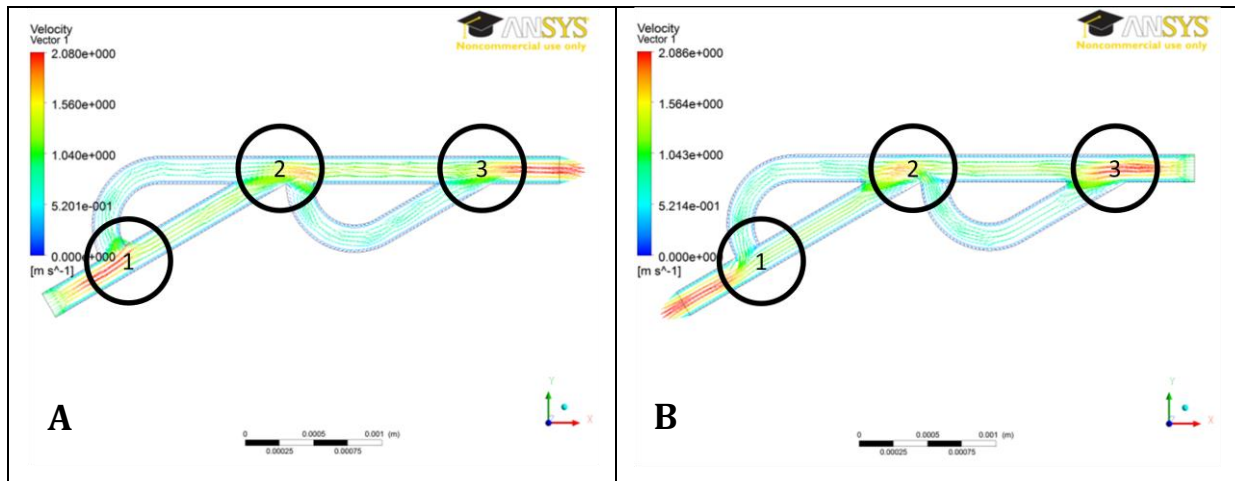


Figure 5-1: Velocity field diagram - (A) positive flow direction; (B) negative flow direction

Figure 5-1-A represents the flow distribution through the downstream check valve when the diaphragm is depressed producing a positive pressure at the inlet to the check valve. For Figure 5-1-A at segment 1, the flow diverges due to the branching of the channel causing a change of direction which leads to a local acceleration of the fluid. Then at segment 2, mixing occurs as the fluid streams reattach and the flow instantly diverges, once again causing an acceleration of the fluid stream. Lastly, segment 3 mixes the flow and exits to the outlet. In Figure 5-1-B, the fluid flow enters at a reverse direction, as would be typical of a check valve upstream of a diaphragm pump. Similar to the positive flow, the velocity field of micro-channel leads to flow acceleration at the same three segments with similar behaviors. The difference is the order of the flow entering the segments as shown in Figure 5-1-B.

In Figure 5-2, the streamline diagram of the positive and negative flow direction is illustrated. For the positive flow, the primary flow path is through the straight conduit while the bends experience only minimal fluid flow; thus, the mixing and diverging of the fluid flow are nominal as shown in Figure 5-2-A. Overall, there appears to be minimal

disturbance of the flow in the positive direction. Figure 5-2-B represents the case of fluid flow in the reverse direction where the streamlines now enter the intricate curvature of the microvalve. The flow is more complex and congested in the bend of the micro-channel which is redirecting the flow and causing flow resistance as a result of the increased pressure drop along this path.

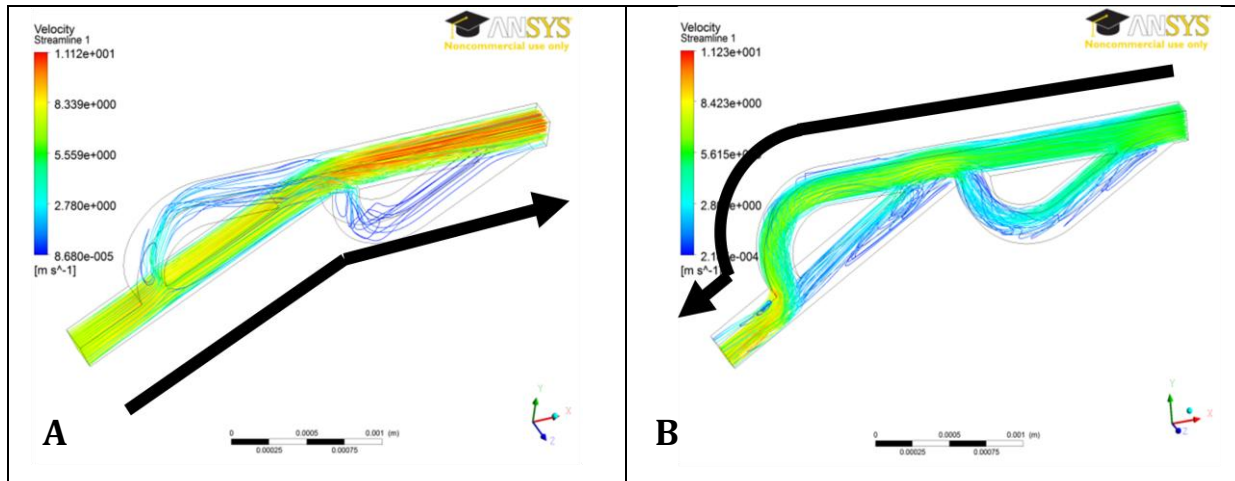


Figure 5-2: Streamline diagram – (A) positive flow direction; (B) negative flow direction

The main observation to make is that bends of the micro-channel are utilized and cause the flow to mix further and produce more resistance in the negative flow direction compared to the positive flow direction of the micro-valve design.

5.1.1.1 Geometrical Discussion

From the visual observation, the under-loop of the conduit design appears to be very ineffective for both the positive and the negative flow direction as illustrated in Figure 5-2. As a result, applying the methodology from Section 3.3, the effectiveness of the under-loop study can be performed. Instead of analyzing the Figure 3-12: Schematic layout of the conduit design, an alternative layout can be analyzed to understand the efficacy of the under-loop as illustrated in Figure 5-3.

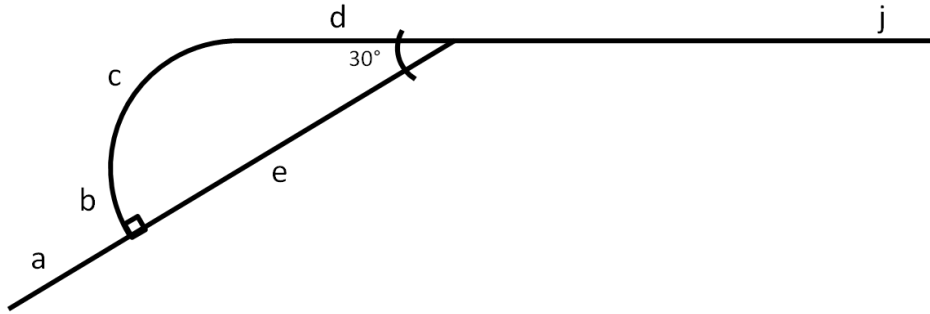


Figure 5-3: Schematic layout of the alternative conduit design

From the schematic of the alternative conduit design without the underloop in Figure 5-3, the representative pressure resistance coefficient circuit can be formed as shown in Figure 5-4.

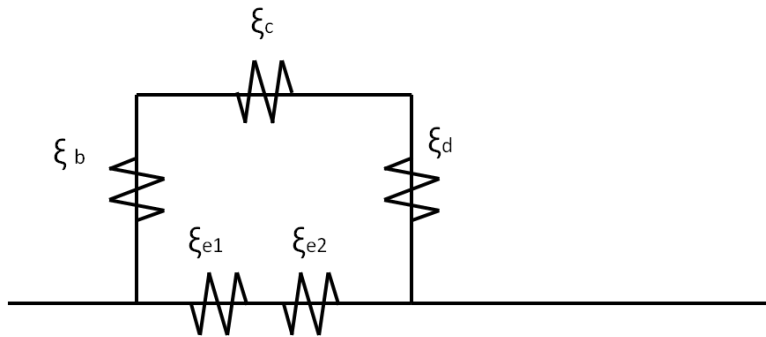


Figure 5-4: Pressure resistance circuit schematics of the alternative design

From the results from ANSYS-CFX, the area averaged velocity in each part of the conduit channel were obtained. Given that the area averaged velocity at specified segments, the pressure resistance coefficients evaluated from the original conduit design does not change for the alternative design even without the underloop. However, the total pressure resistance coefficient expression (i.e. Equation 3-5) only applies to the sections (1) to (3), (i.e. ξ_{1-3} only). As a result, the total pressure loss evaluated for the positive and negative flow directions are 158.84 [Pa] and 1097.5 [Pa] respectively.

Table 5-1: Pressure Loss Comparison between the Original and the Alternative Design

<i>Design</i>	$P_{positive\ flow}$ [Pa]	$P_{negative\ flow}$ [Pa]	<i>Pressure Loss Ratio,</i> $= P_{negative\ flow}/P_{positive\ flow}$	<i>Pressure Loss Difference [Pa],</i> $= P_{negative\ flow} - P_{positive\ flow}$
<i>Original</i>	158.84	1357.7	8.5476	1198.9
<i>Alternative</i>	158.84	1097.5	6.9095	938.66

The pressure loss in the positive flow direction had no change because the pressure loss due to the under-loop was zero for the original design. When comparing the pressure loss between the original and the alternative design of the conduit, the original conduit design produced a larger pressure loss difference of approximately 21.71 % according to Table 5-1. Therefore, the underloop generated approximately 21.71 % more effective valvular conduit design.

5.1.2 Optimization of the Micro-valve (Steady State Results)

From the original design of Tesla [28], other features of the design were examined. By changing some of the parameters (e.g. branched angle of the bend of the channel, channel thickness, and radii of the bend) in isolation during the steady state simulations, some optimizations were achieved. The optimization was accomplished by calculating the maximum difference between the pressure values of the negative and positive flow direction and the pressure ratio between the pressure values of the negative and the positive flow as displayed in Figure 5-5.

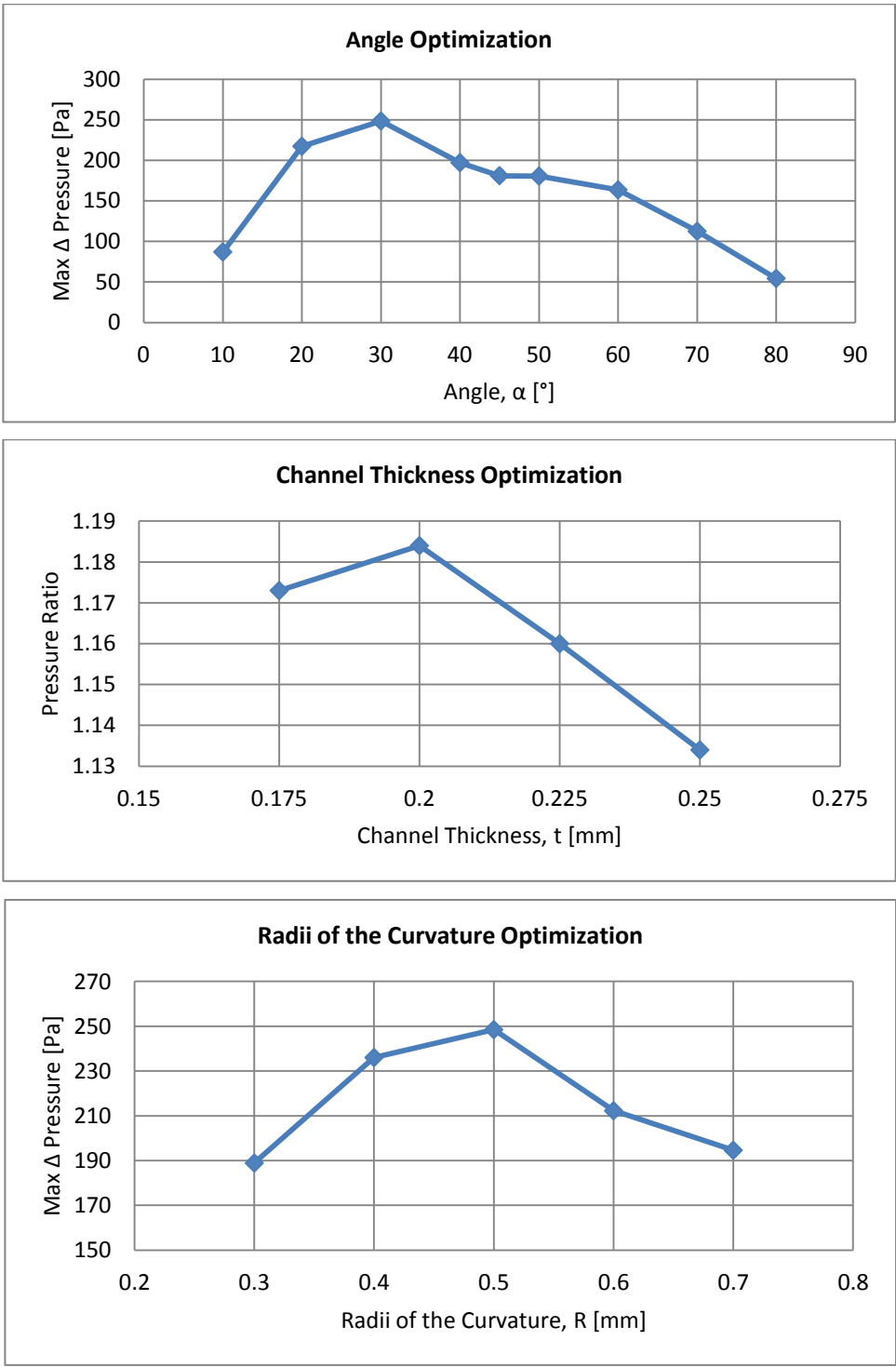


Figure 5-5: Optimization Plots of the physical characteristics of the conduit: Up – Angle, Middle – Channel Thickness, and Bottom – Radii of the Curvature

A summary of the optimization of the valvular conduit design is listed in Table 5-2. The optimal dimensions of the design characteristic are: 30 [°] for the angles (α_1 and α_2), 0.200 [mm] for the channel thickness (t) and 0.500 [mm] for the curvature bend radii (R_1 and R_2) as highlighted in Table 5-2.

Table 5-2: Optimization of the Valvular Conduit Design

Angle		Channel Thickness		Radii of the Bend	
α [°]	Max Δ Pressure [Pa]	t [mm]	Pressure Ratio	R [mm]	Max Δ Pressure [Pa]
10	86.990	0.175	1.173	0.300	188.96
20	217.40	0.200	1.184	0.400	236.05
30	248.52	0.225	1.160	0.500	248.52
40	197.17	0.250	1.134	0.600	212.31
45	181.10	It is evident that as the cross-sectional area decreases the difference in pressure increases but for all cases the max pressure difference occurs at 30 °.		0.700	194.67
50	180.63			The dimension side of 0.2 μm was kept constant and the max pressure difference occurred between the angles of 30 °- 40 °.	
60	163.63				
70	112.51				
80	54.380				

5.1.3 Evaluation of the Micro-valve (Transient Results)

After the optimization of the valvular conduit design, a numerical pumping simulation was performed. As explained in Section 3.3, the transient simulations were performed based on the studies from optimization. From ANSYS-CFX, the outlet normal velocity (defined as the area average velocity value normal to the cross-section of the outlet) is obtained. Then the volumetric flow rate is evaluated since it is directly proportional to the normal velocity.

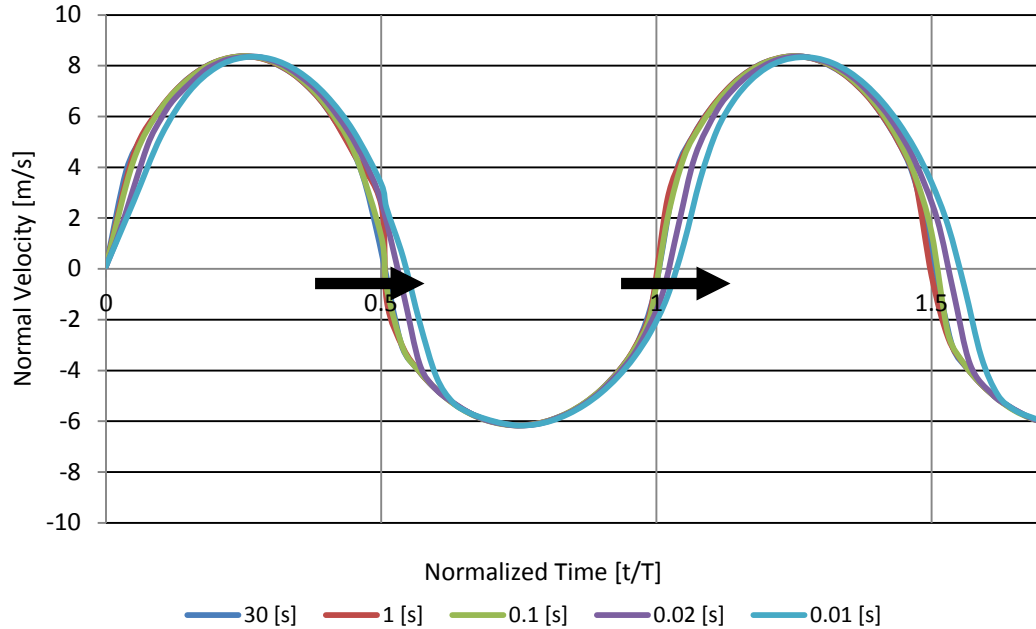


Figure 5-6: Normal Velocity of the outlet over normalized time

In order to compare the results of the various time periods, the time (primary x-axis) was normalized by dividing respective instantaneous time by the duration of the period as shown in Figure 5-6. As illustrated in Figure 5-6, as the duration of the period decreases the oscillating wave function shifts. This is due to the frequency rate of the fluctuating pressure, since the fluid requires time to react in the channel; the higher the frequency, the greater the delay in response of the fluid flow. This shift is reasonable due to the mass flow lag from the pressure variation because of the flow inertial feature. It is evident that the flow plot of various time periods shown, in Figure 5-6, is basically oscillating with a non-zero mean because of its asymmetry; therefore, the flow will produce a net mass flow [35].

The effectiveness of adjusting the frequency merits further discussion. The method chosen is to compare the total volumetric flow rate per unit area transferred over a single period time. Using the trapezoidal rule, the area under the curve was calculated to evaluate the accumulated flow rate. Then the sum of the positive and negative areas over the duration of the period gave the volumetric flow rate per unit area per period. Figure 5-7 illustrates a volumetric flow rate per unit area over a single period and the accumulated

flow rate per unit area. As observed, the positive flow rate is multiple of 1.38 greater than the negative flow rate; hence, the total volume per unit area transferred is 8.274 [mm] over 0.0096 [s]. As a result, the volumetric flow rate per unit area (i.e. area average velocity) at 100 [Hz] was 0.862 [m/s].

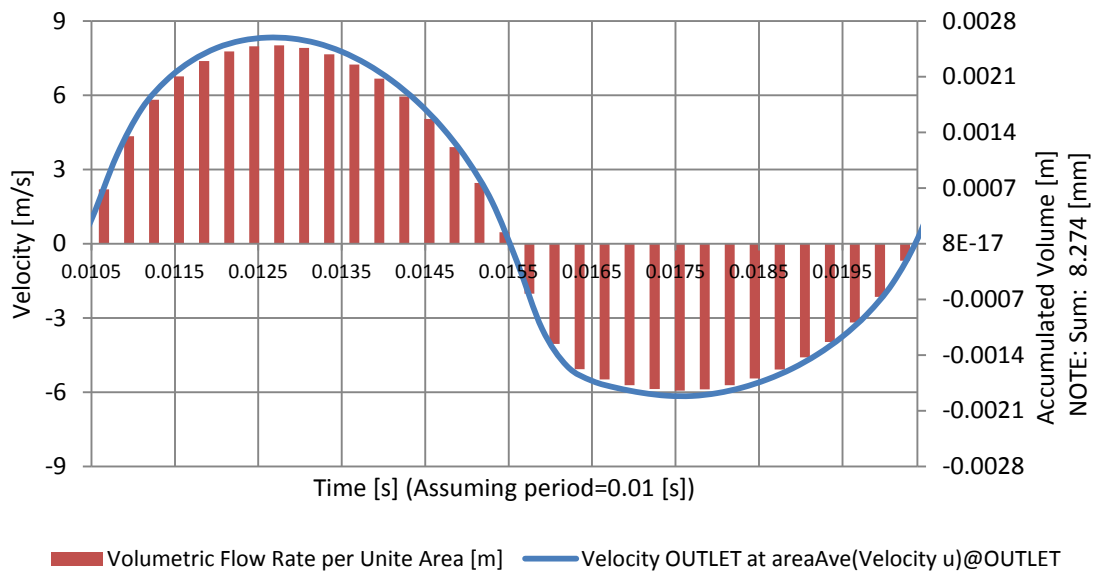


Figure 5-7: Plot of accumulated flow rate over a period at frequency 100 [Hz]

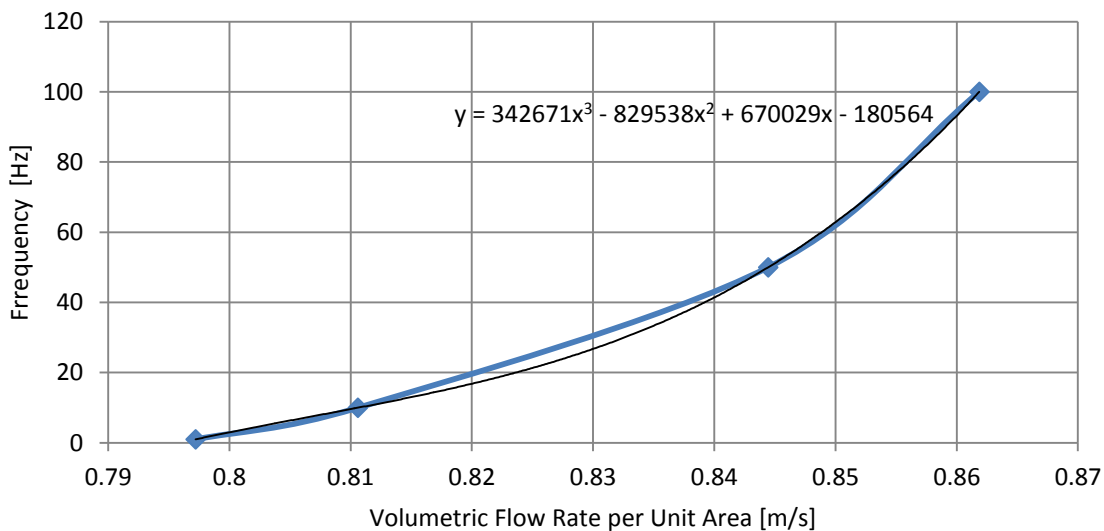


Figure 5-8: Plot of average velocity over frequency

Thus, the other frequencies were evaluated similarly to plot the volumetric flow rate per unit area over various frequencies as shown in Figure 5-8. The effectiveness of the frequency/period change was evident as shown in Figure 5-8. According to the Microsoft EXCEL 2007 best fit-tread line, the correlation between the area average velocity (\dot{v}) and the frequency (f) was generated as listed:

$$f = 342671 \cdot \dot{v}^3 - 829538 \cdot \dot{v}^2 + 670029 \cdot \dot{v} - 180564 \quad \text{Equation 5-1}$$

As the frequency increases, the volumetric flow rate increases in a direct inverse cubic function correlation. This clearly demonstrates the fundamental premise of the valvular conduit and shows its potential for use in a micro valve with no mechanical parts.

From Table 2-2, the piezoelectric diaphragm pump operating at 70 – 180 [Hz], which translates to volumetric flow rates per unit area in the range of 0.8529 – 0.8787 [m/s] obtained by Equation 5-1. With the constant cross-sectional of the valvular conduit known (i.e. 0.04 [mm²]), the volumetric flow rate ranges from 2.046 – 2.108 [mL/min]. Using Equation 2-2, the total heat transfer ($Q_{out} = TDP$) can be calculated from the known flow rates, between 7.15 – 7.37 [W] at a single period (0.014 – 0.0056 [s]). The heat dissipation required for the Pentium D processor is 130 [W]; therefore, at an operating rate in the range of 70 – 180 [Hz], the time required to dissipate the produced heat ranges between 0.255 – 0.0988 [s]. Thus, this non-mechanical valvular conduit can produce sufficient flow rate to dissipate the TDP within the operating frequency. In addition, as illustrated in Figure 5-8, the flow rate increases with increasing frequency. Considering increasing cross-sectional area and/or the frequency, the valvular conduit design has the ability to be employed in diaphragm pumps for cooling applications. The following step is to compare the accuracy of the numerical results to the experimental results.

5.2 Experimental results

As explained in section 4.3, the experiments were conducted at various volumetric flow rates of 5 [ml/min], 10 [ml/min], 15 [ml/min], 20 [ml/min], and 25 [ml/min] for both

positive and negative flow direction of the valvular conduit. The pump apparatus used was able to prescribe a specified input flow rate in milliliters per minute [ml/min].

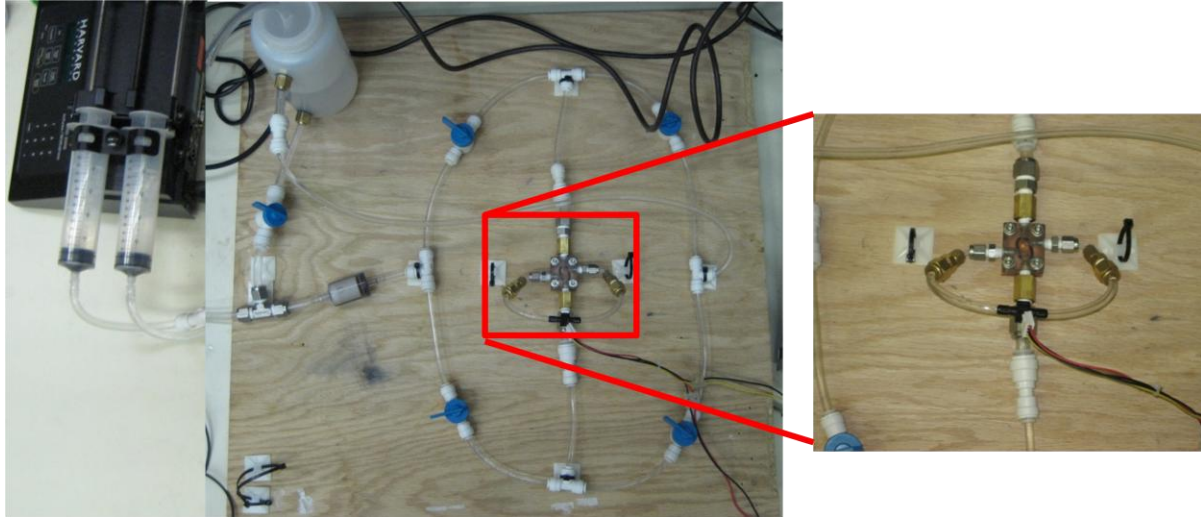


Figure 5-9: Pressure drop reading location in the test rig

During the experiments, the reading of the pressure drop across the micro-channel was taken at steady state for each flow rate as indicated in Figure 5-9. It was observed that at high flow rates the pressure readings fluctuated significantly which can be reviewed in Appendix D. As a consequence, rather than acquiring one measurement, multiple measurements were taken systematically (i.e. every 1 minute) to visualize the range of results at each flow rate.

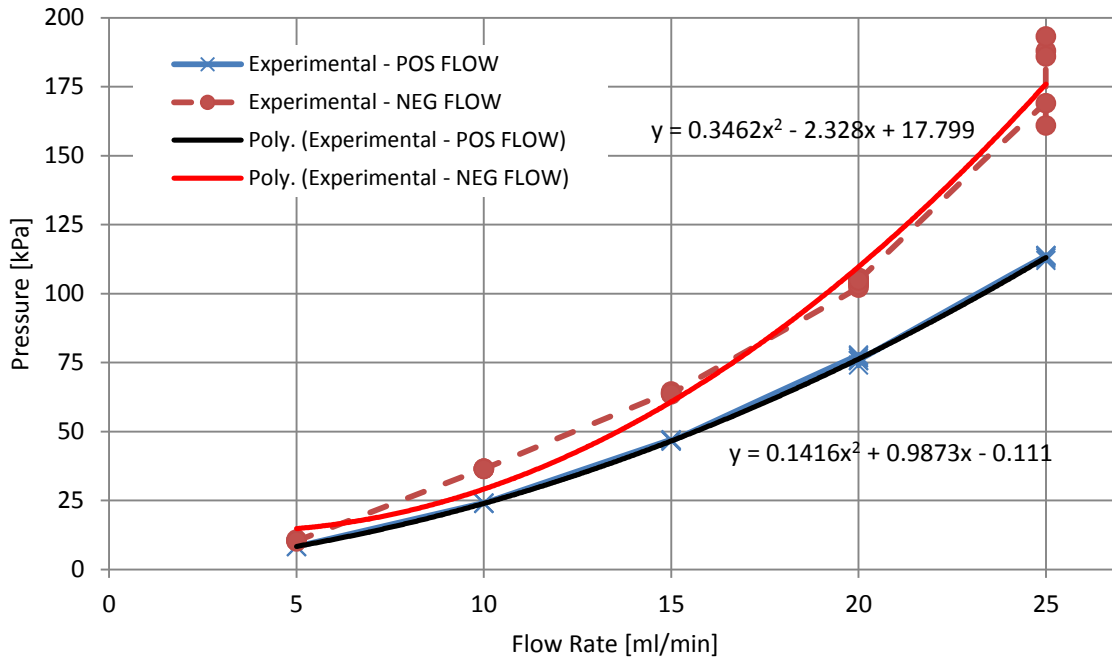


Figure 5-10: Multiple pressure measurements at specified flow rates

The tests were performed to distinctly define the pressure and flow rate profile of the valvular conduit design. As a consequence, there are clear distinctions between the positive and negative flow direction of the conduit in terms of their pressure drop readings as shown in Figure 5-10. From Figure 5-10, at 25 [ml/min] flow rate the pressure value measure varies approximately 35 [kPa]. Also, as shown in Figure 5-1 and Figure 5-2, the negative direction flow enters the multiple bends of the micro-channel more vigorously than the positive direction flow. This can cause disturbances in the readings. Thus, this may be the cause of inconsistent results during the negative flow pressure measurement compared to those of the positive flow pressure measurement. In order to resolve these inconsistent results, there were five trials for the experimental pressure measurements with same condition each time. Each trial was sampled every minute after the steady state was fairly established.

From the multiple readings, using Microsoft EXCEL 2007, best-fit trend lines of the results were obtained as shown in Figure 5-10. The profiles of the plot fit well with a quadratic function, especially the measurements obtained for positive flow direction. When comparing the two trend-line equations, the quadratic coefficient of the negative flow plot is approximately 2.44 times greater than that of the positive flow plot, which is a significant difference between the pressure resistance generated in the negative flow direction and the positive flow direction.

5.2.1 Model Validation versus Experimental Results

The purpose of the experimental results was to validate the accuracy of the simulated results. The simulated results have demonstrated the fundamental behavior of the micro valve in regulating directional flow patterns and the experimental testing is used to substantiate these observations. Another numerical simulation was executed using the specified flow rates employed in the experiments using the same parameters (i.e. mesh elements/nodes, fluid properties, etc) derived from the ANSYS-CFX simulation performed in Chapter 3.

Table 5-3: Simulated Results from ANSYS-CFX Workbench

Density		997.0	[kg/m ³]	Simulated –Pressure Drop		
Dynamic Viscosity		8.899E-04	[kg*m/s]			
Kinematic Viscosity		1.004	[mm ² /s]			
Cross-Sectional Area		0.040	[mm ²]			
Hydraulic Diameter (D_h)		0.200	[mm]			
Flow Rate		Normal Speed	Reynolds Number	Positive	Negative	Differences
[ml/min]	[mm³/s]	[m/s]		[kPa]	[kPa]	[kPa]
2.4	40.00	1.000	199.2	2.799	3.316	0.517
5	83.33	2.083	415.0	7.660	10.54	2.880
10	166.7	4.167	830.0	20.82	34.58	13.76
15	250.0	6.250	1245	37.92	72.69	34.77
20	333.3	8.333	1660	58.41	124.0	65.59
25	416.7	10.42	2075	82.12	193.8	111.68

Based on the Reynolds numbers listed in Table 5-3, the flow model is considered to be laminar flow (i.e. $Re < 2300$). With these flow conditions and the fluid properties listed in Table 5-3, another set of simulation results were obtained and are recorded in Table 5-3. Comparing the positive and negative flow graphs in Figure 5-11, the pressure values for the negative flow are significantly greater than that of positive flow, which is similar to the experimental results.

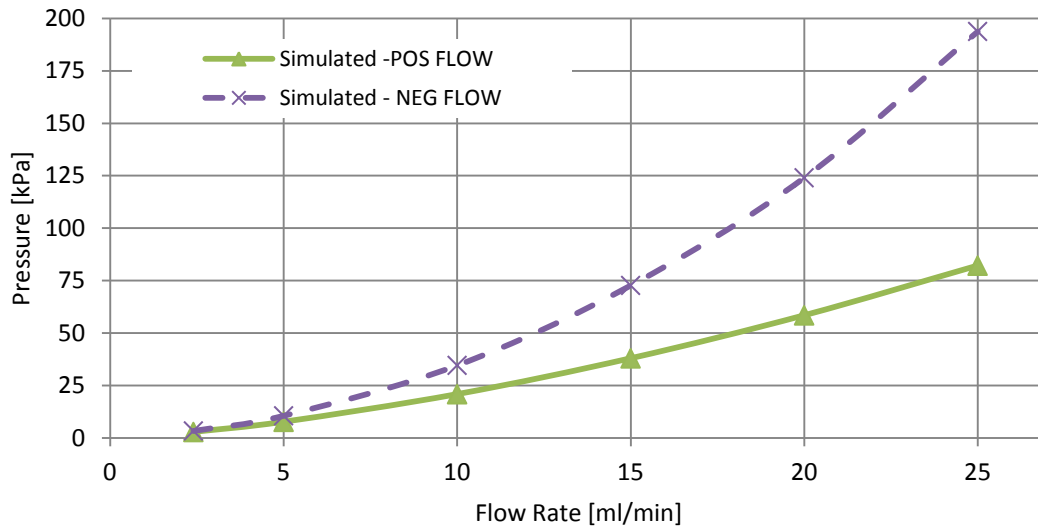


Figure 5-11: Simulation for valvular conduit design confirmation

5.2.2 Comparison of the Experiment and the Simulation

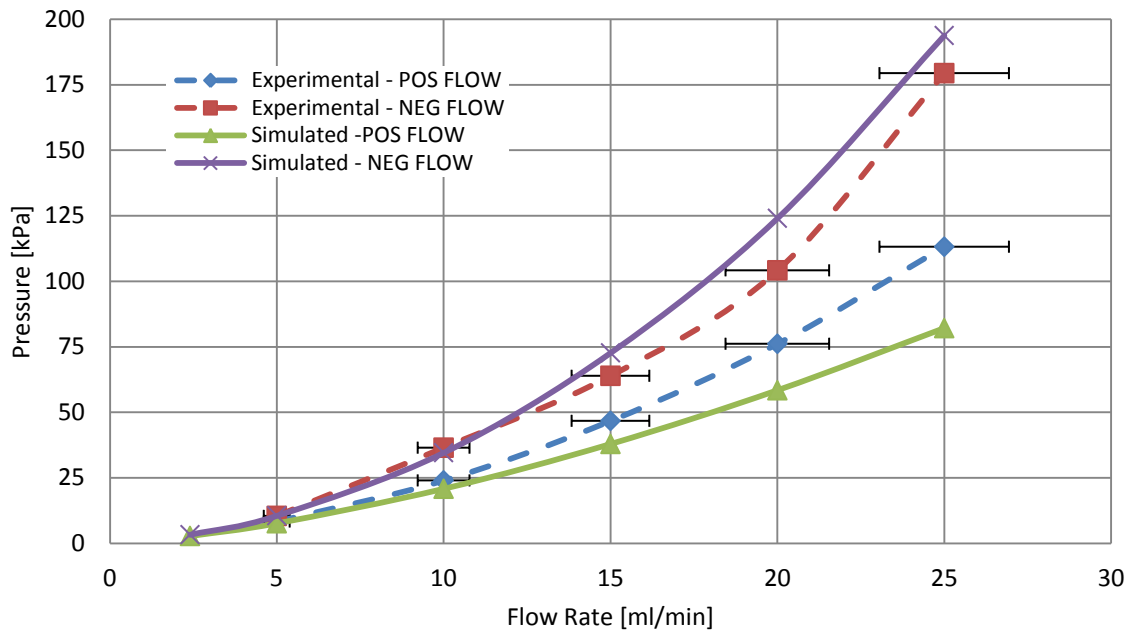


Figure 5-12: Comparison between experimental and simulated results with uncertainty analysis

When comparing the experimental data and the simulated data, it is evident that both follow similar trends as observed in Figure 5-12. Experimental and simulated results demonstrate significant differences between pressure measurements for positive and negative direction flow. The experimental results for the negative direction flow are slightly below the simulated results while the experimental positive direction flow results are slightly above the simulated results for a flow rate greater than 10 [ml/min]. The possible explanation of the discrepancy could be where the pressure drop is measured. In the numerical case, the pressure readings were attained directly at the entrance and exit of the micro-channel only, whereas in the experimental case, the pressure readings were obtained from the external cover which is connected to plastic tubes attached to the pressure transducer.

Figure 5-12 illustrates various plots of pressure versus the flow rate based on the simulation results and the averaged experimental results when the uncertainty analysis

(from section 4.3.1.1) of the experiment was considered. Taking the uncertainty analysis to the averaged experimental flow rate results, the experimental plots show 7.76 % of inaccuracy within the flow rate measurements (x-axis error bars). As for the uncertainty of the pressure measurements (y-axis error bars), it was neglected because the inaccuracy was only 1.003 % of the readings. From Figure 5-12, the results are in a better agreement with the averaged experimental results when the uncertainty analysis was considered.

Due to the obvious uncertainty as a result of the transducer location, the differences of the pressure drop across the conduit between the negative and the positive flow directions were evaluated. Subsequently, the pressure uncertainty of the transducer location can be ignored since the differences will cancel the pressure uncertainty from the negative and the positive flow pressure drop measurements. With the new pressure differences value, the new pressure uncertainty value was calculated 10.97 % using the root sum square method. Hence, the results can be compared as shown in Figure 5-13.

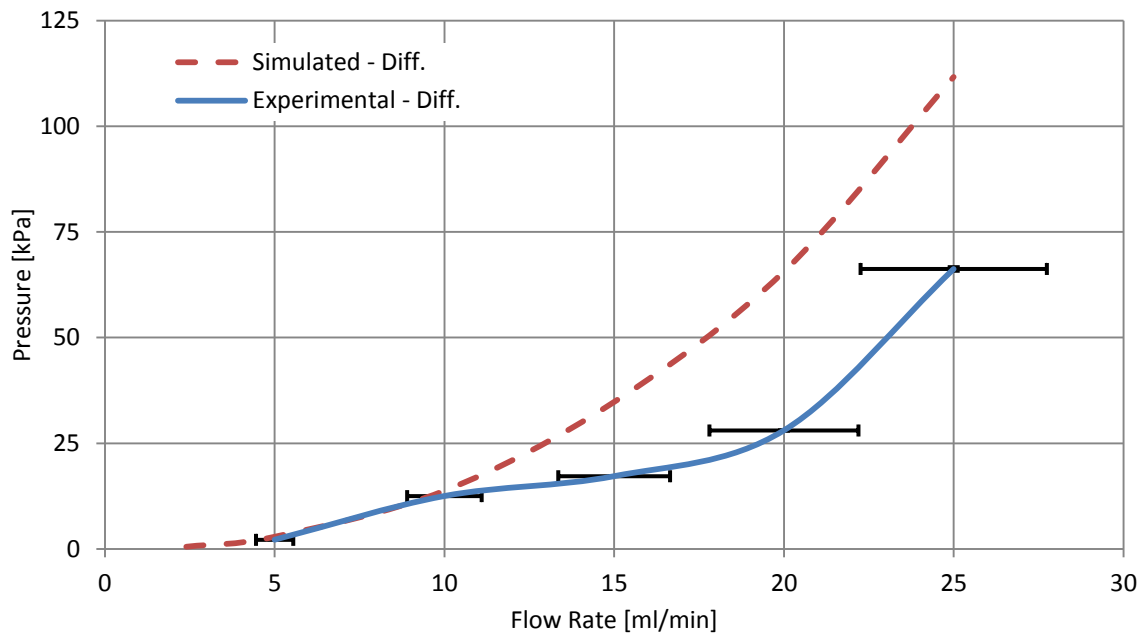


Figure 5-13: Comparison between experimental and simulated difference results with uncertainty analysis

In addition to the uncertainty analysis, another obvious source of error is the dimensions measured from the prototype design compared to the dimensions of the simulations. In the simulation the dimensions are consistent with no variation but as shown in Section 4.2.2 Table 4-1, not all measurements were aligned to each other and were inconsistent throughout. Thus, a study for tolerance of the dimensions was examined to observe the influence of change in pressure measurements on several differences in the cross-sectional dimensions.

5.2.2.1 Numerical Study with Actual Dimensional Discrepancy Tolerance

From Section 4.2.2, one of the actual cross-sectional measurements differs by roughly 9.1 % of the intended dimension (i.e. 200 [μm]) as shown in Table 4-1. Table 4-1 illustrates that the channel’s cross-sectional dimension varied along the path of the micro-channel. As mentioned in Section 4.2.2, the measurements deviate by approximately 4.7 % of the intended dimension. As a result, dimension tolerance of ±5 % (i.e. 200±10 [μm]) was investigated during the simulations to study the effect of the valvular conduit design performance.

Table 5-4: Simulated discrepancy study results

Flow Rate	Positive Flow				Negative Flow			
	+5%	-5%	Diff. Mag 	% Diff.	+5%	-5%	Diff. Mag 	% Diff
[ml/min]	[kPa]	[kPa]	[kPa]	-	[kPa]	[kPa]	[kPa]	-
2.4	2.663	2.998	0.3348	11.83	3.181	3.475	0.2937	8.823
5	7.359	8.134	0.7753	10.01	10.26	10.79	0.5300	5.036
10	20.05	21.99	1.936	9.210	33.85	34.71	0.8522	2.486
15	36.58	40.01	3.426	8.948	70.67	71.60	0.9279	1.304
20	56.25	61.53	5.286	8.976	121.3	122.1	0.8035	0.6603
25	78.94	86.16	7.222	8.748	184.8	186.9	2.169	1.167

From Table 5-4, the percent differences of the two tolerance values were evaluated by dividing the difference between -5 % and +5 % values by the average value of the two. The discrepancy tolerance study shows that, during negative direction flow, the change in

cross-sectional dimension caused almost no impact on the pressure results at a flow rate higher than 15 [ml/min]. During positive direction flow, the percent difference between the two extremes of the tolerance ranges from 8.75 – 11.8 %.

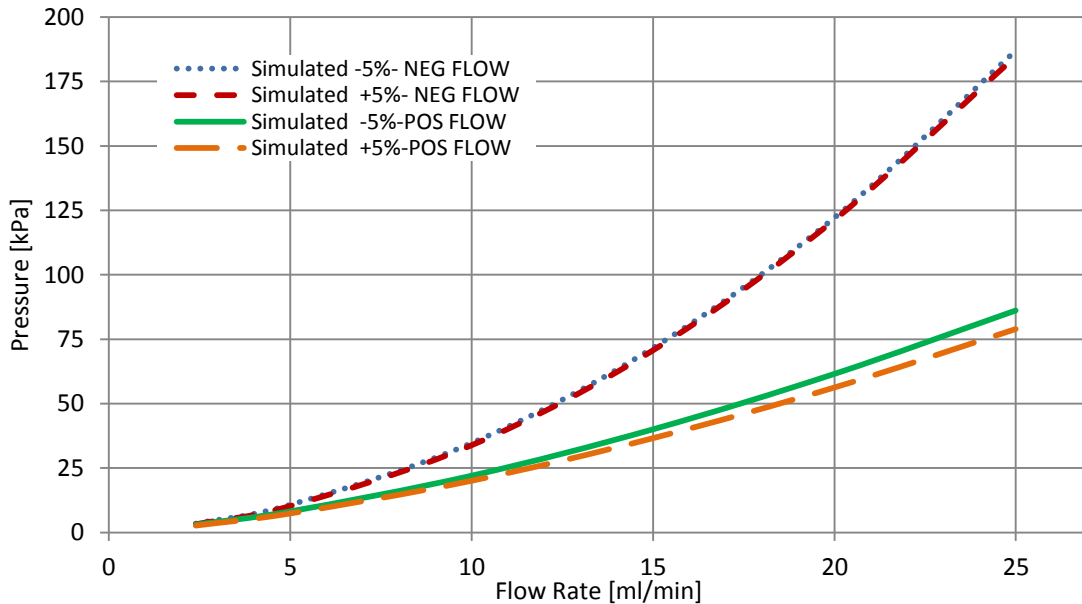


Figure 5-14: Simulated results with tolerance $\pm 5\%$

After analyzing the plot in Figure 5-14, it is apparent that the slight error in cross-sectional length can alter the effectiveness of the valvular conduit design for the positive direction flow. However, it had a minimal effect on the negative direction flow. In summary, both flow directions showed differences in results with a change in dimensional tolerance, but the differences were greater for the positive flow than the negative flow. Through a visual observation of the numerical study, as shown in section 5.1.1, the main pressure resistance in the negative flow direction is generated by the curvature bends of the conduit design as seen in Figure 5-2. Figure 5-14 also illustrates that the pressure resistance due to the change in the cross-sectional area is negligible in the negative flow direction. When the fluid flows in the positive direction, even the slightest change in the cross-sectional area can affect the pressure drop value as demonstrated in Figure 5-14. This is due to the fact

that pressure resistance has no effect caused by the curvature bends in the positive flow direction as shown in Figure 5-1.

5.2.2.2 Prototype Dimensional Discrepancy Tolerance and the Uncertainty Analysis

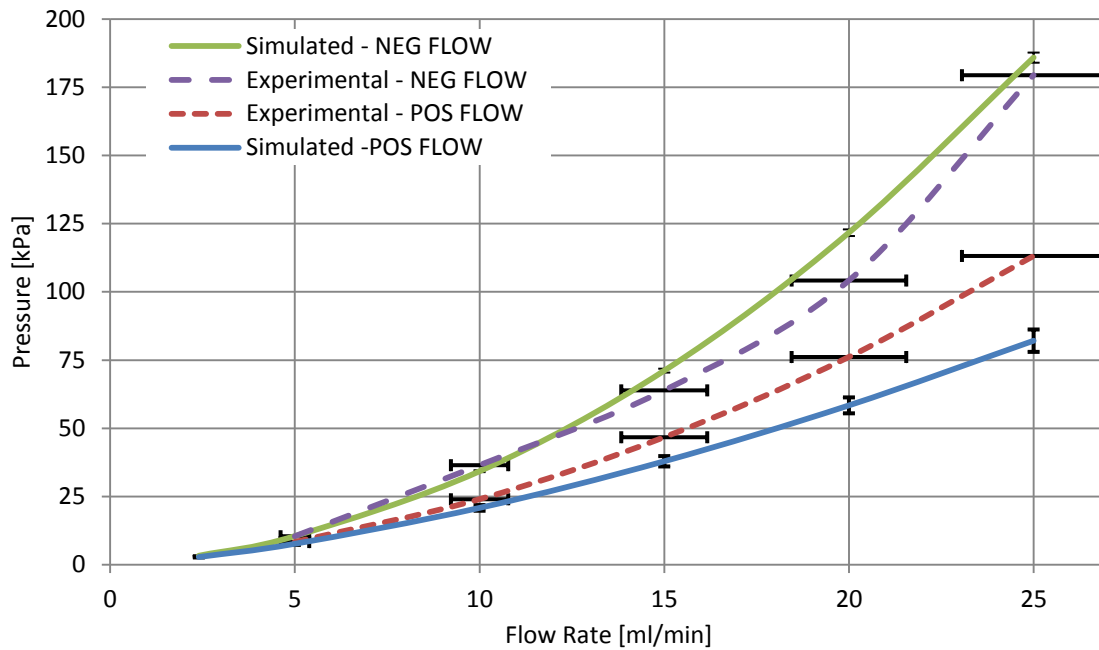


Figure 5-15: Comparison between experimental and simulated results with dimensional tolerance and uncertainty analysis considered

Since the cross-sectional dimension (i.e. width) of the micro-channel was inconsistent along the path of the micro-channel, the prototype dimensional discrepancy tolerance of 5 % was used when comparing the experimental and simulated results with the uncertainty analysis as displayed in Figure 5-15. With the extremes of the conduit design dimensional discrepancy (5 %) considered in the simulations and uncertainty analysis considered in the experimental results, the experimental and numerical results are in better agreement, which is seen by comparing Figure 5-12 and Figure 5-15. Both the negative and positive flow direction plots of simulation and experiments have narrowed closer to each other. Especially in the positive flow direction, the simulated plot is within the uncertainty bar in the experimental plot.

When the differences of the pressure drop across the conduit between the negative and the positive flow directions were plotted with the uncertainty and dimensional tolerance considered, the experimental and simulated plots are in a better agreement as shown in Figure 5-16.

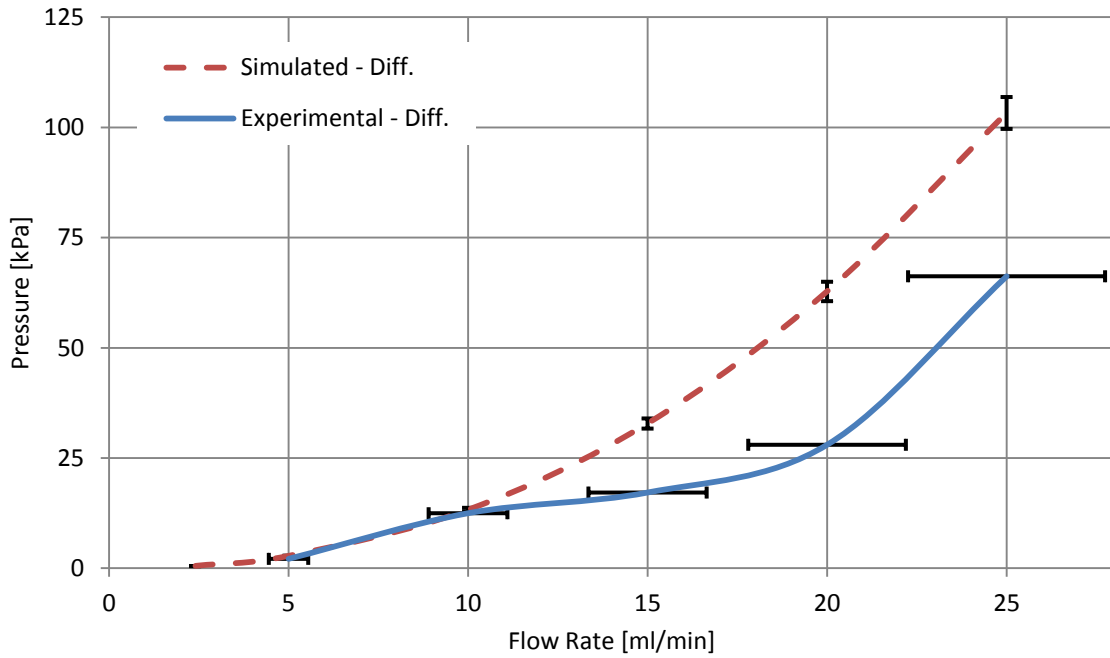


Figure 5-16: Pressure difference between negative and positive flow direction plot of simulated and experimental results with uncertainty and dimensional tolerance considered

Chapter 6

CONCLUSION

In conclusion, the need for micro-pumps in cooling small-scaled portable computers (e.g. laptops and netbooks) is apparent. The single phase liquid cooling system has great potential in the next generation for implementation in dissipating heat from computer processors. For the liquid cooling system, the feasibility of the micro-diaphragm-pump is very high, and check valve research will be important since it is one of the major components in diaphragm pumps.

From this research, the non-mechanical valvular conduit has demonstrated potential as a replacement for check valves in micro-scale pumps. The valvular design uses the principle of pressure resistance generated from the bend curvatures, divergence and convergence in the channel flow such that one direction is favorable over the other. During the numerical analysis, the geometric dimensions of the valvular conduit design were very sensitive to change in pressure drop across the conduit; hence, the geometric dimensions were optimized to following values: $\alpha = 30^\circ$, $t = 0.200$ [mm], and $R = 0.500$ [mm]. In addition, by applying the methodology from Idel'Chik [34], the overall pressure resistances were estimated which proved that the favorable direction produced 8.55 times less pressure resistance.

For the transient simulation, the pumping procedure performance was successful. In a pumping sequence, the volume chamber in a diaphragm pump oscillates. This will result in a pressure change in the entrance of the check valve. Hence, when the pressure oscillates at the entrance, the behavior of the valve must favor the fluid flow in one direction only. From the pumping simulation, the accumulated flow rate demonstrated that the fluid flow is favored in the positive direction by the multiple factor of 1.38. As the frequency of the fluctuation increases, the accumulation of the flow increases in performance exponentially. Thus, with the cross-sectional area of 0.709 [mm²], the optimized geometrical design of the valvular conduit can produce a sufficient flow rate to dissipate the necessary TDP (130 [W]) within the piezo-electric diaphragm operating frequency (70 – 180 [Hz]).

The experiments only validated the performance of the valvular conduit design. The experimental plots/results illustrated that the negative flow produced 2.44 times greater pressure resistance than the positive flow. The hypothesis of its performance derived from the numerical analysis was correct and the results agree with the simulation results. There were some unexpected discrepancies between the experimental and the numerical approach but considering the dimensional tolerance and the uncertainty analysis, the results were in concurrence.

In general, the non-mechanical valvular conduit design demonstrates great potential for replacing check valves in micro-scale single-phase flow. Check valves will be still applicable in the macro-scale because of the simplicity of the mechanism; however, this non-mechanical valvular conduit design will be as effective without any possibility of obstructing a mechanism especially in micro-scale.

Chapter 7

RECOMMENDATION

As technology advances, the processors integrated circuit chips (ICC) are becoming more condensed. This will lead to better/faster computers which generate more heat. Currently, a forced air cooling system is the most common system in actual application due to its ease of implementation. However, the demand for dissipating heat will rise and air cooling system will be insufficient to cool the processor at an operating temperature. Thus, more research into cooling systems that require a different mode of cooling from an air/fan is highly recommended. From past research paper from Kandikar [7], changing the fluid of the cooling system was the obvious step. For this reason, more research with regard to liquid cooling systems is recommended.

In this thesis, past research of various micro-pumps was investigated for a single phase liquid cooling system. Furthermore, simple examinations on an appropriate pump design for a laptop were made. From this study, a micro-diaphragm-pump was considered as the best candidate for micro-cooling applications. With regard to a diaphragm pump, this thesis focused on creative valvular conduit design such that the implementation of micro-pumps in application can be feasible. However, further thorough research on this topic is recommended to improve the effectiveness and efficiency of the cooling system.

During the study of the valvular design, two approaches were considered: numerical and experimental. For a numerical approach to the research, boundary conditions were set to simplify the study in order to understand the effect of the key components of the valvular conduit design; however, more accurate boundary conditions should be suggested to produce more accurate results. Also, the main objective of this thesis was to understand the valvular conduit design in pump operation; therefore, a simulation with a diaphragm chamber which oscillates in pressure to produce flow into the valvular conduit design, an idea also used in Wang et al.'s paper [35]. For the experimental approach, a test setup that minimizes possible sources of error (e.g. air bubbles, accuracy errors, etc.) is highly recommended. In addition, for this research work, the experiment was conducted to

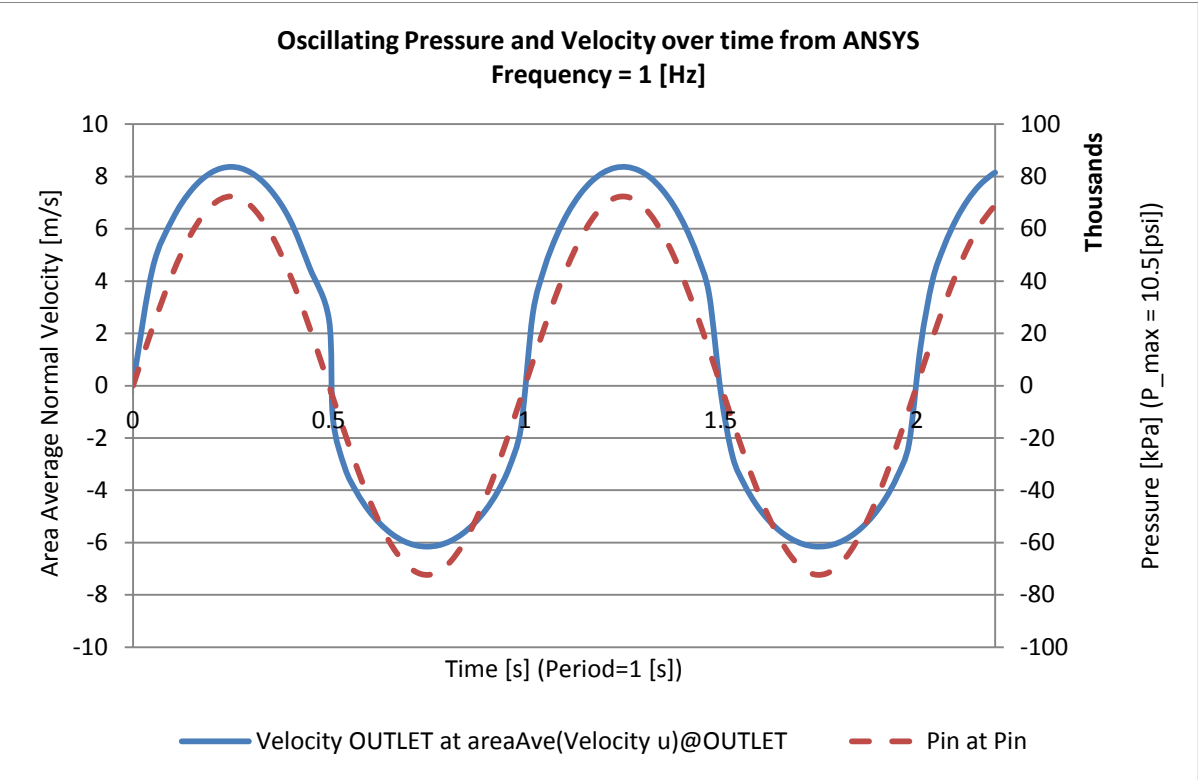
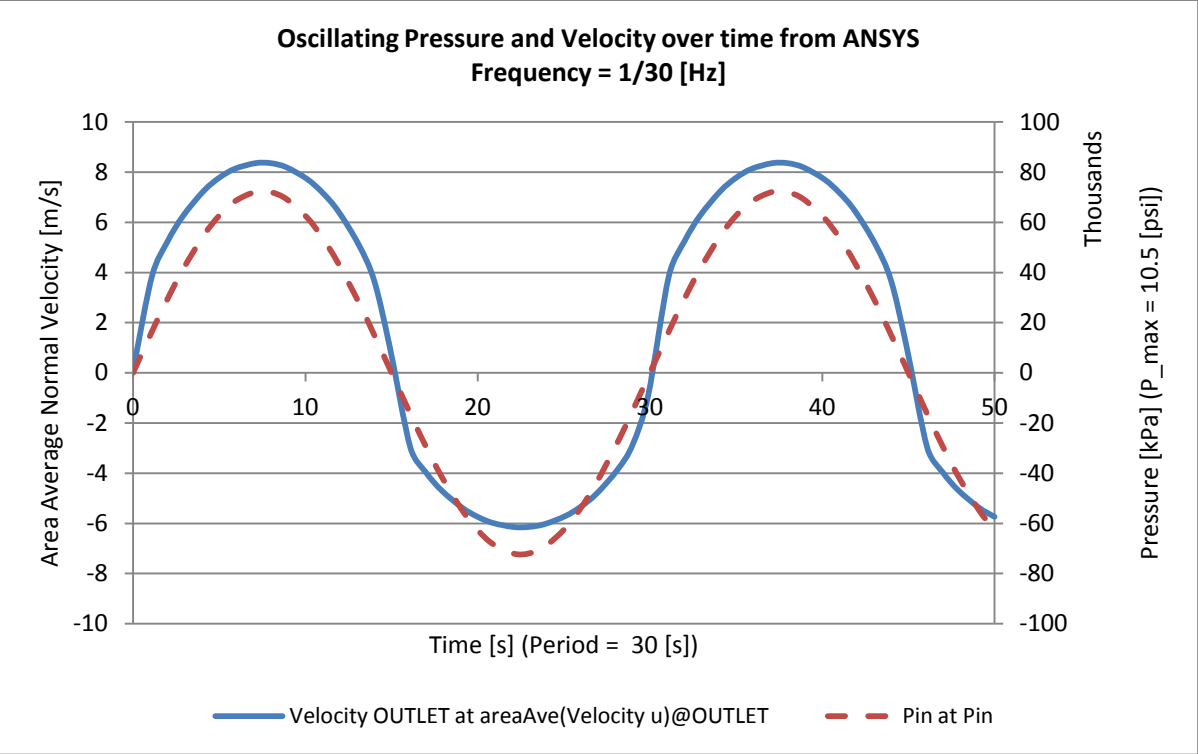
validate the performance of the numerical approach but it is strongly recommended to fabricate an actual experimental setup which can be used to observe the effectiveness of the valvular conduit design during the pumping process.

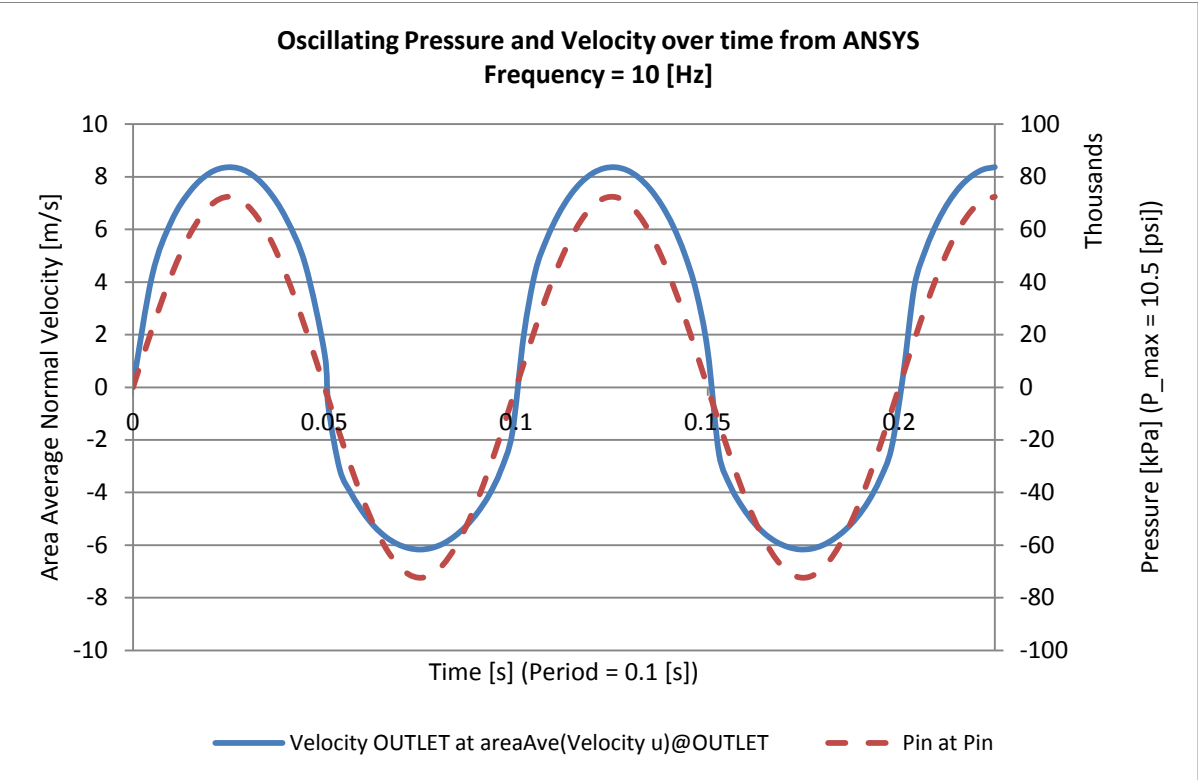
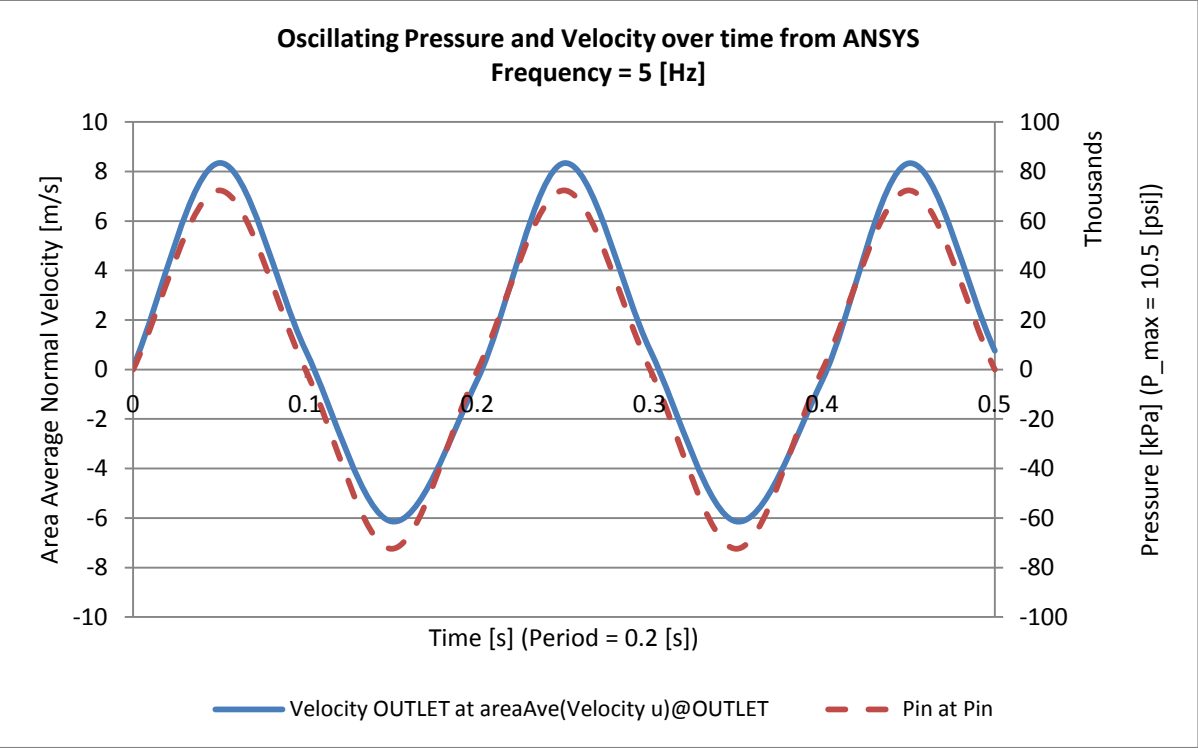
Appendix A

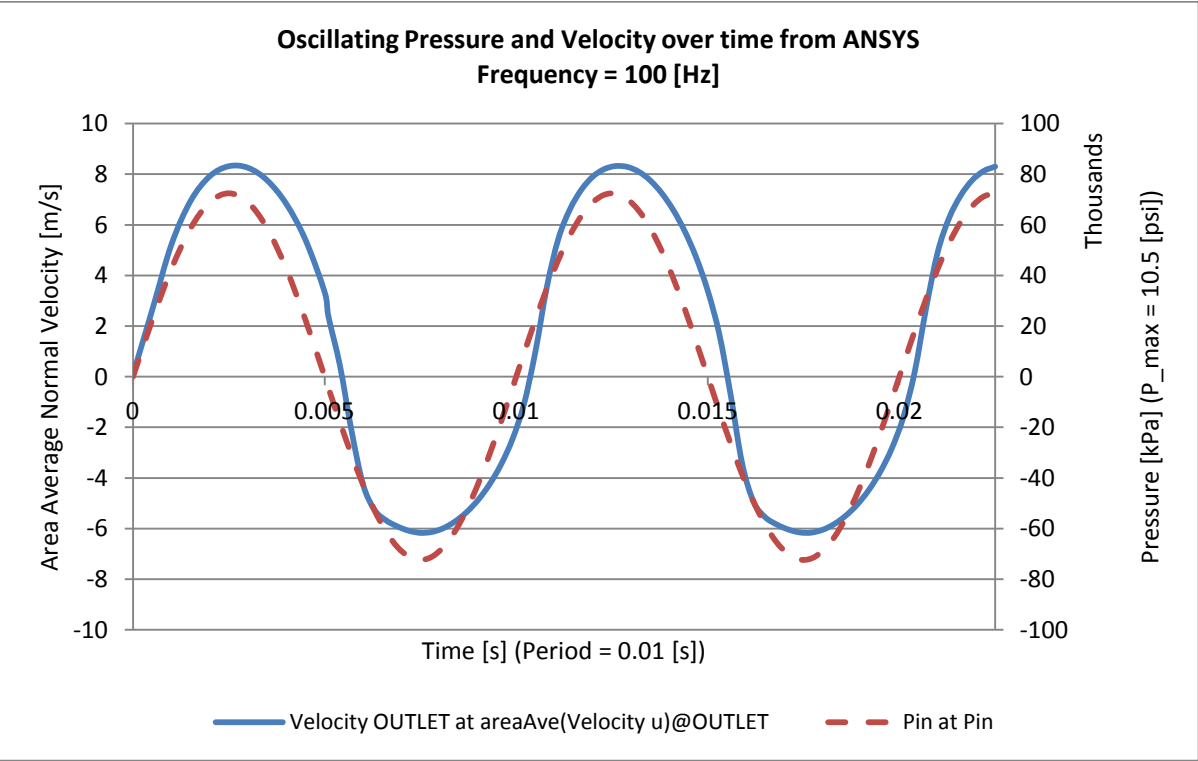
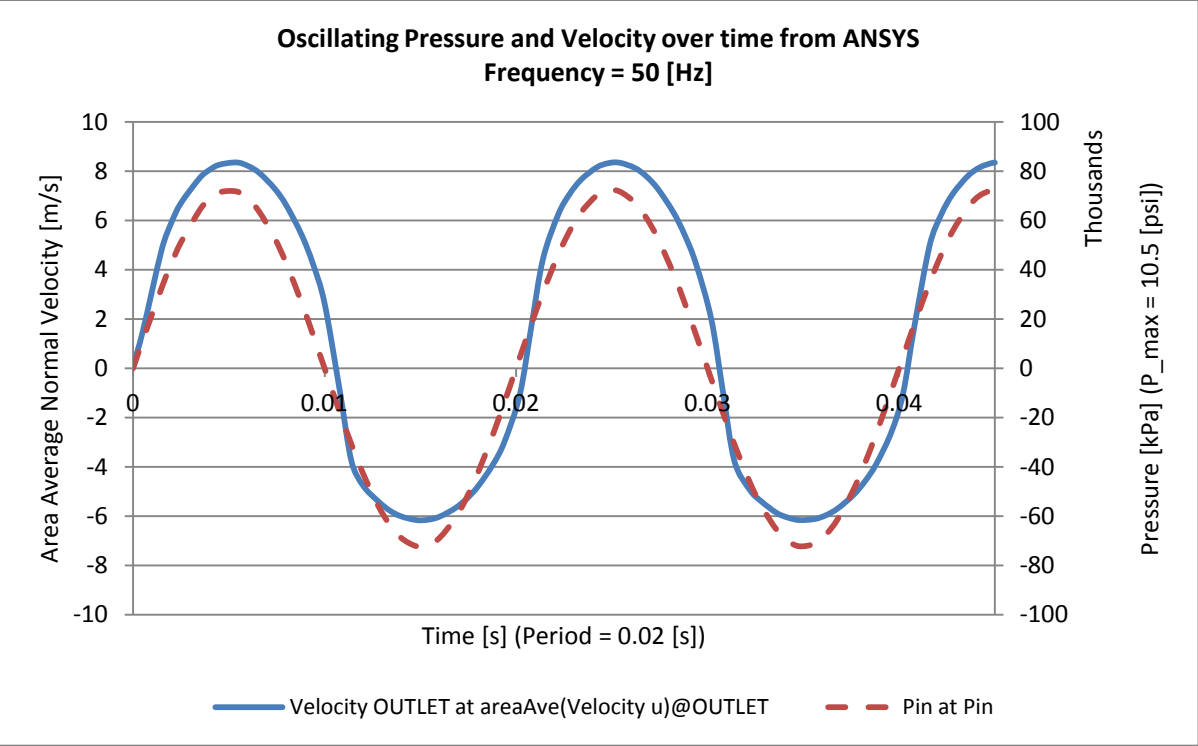
Transient: Setup and Results

Analysis Type	
<i>Transient</i>	
Total Time	50 [s]
Time Steps	0.05 [s]
Initial Time	0 [s]
Default Domain	
<i>Basic Setting</i>	
Domain Type	Fluid Domain
Material	Water
Domain Motion	Stationary
Fluid Model	Turbulence
Option	k-Epsilon
Wall Function	Scalable
<i>Boundary</i>	
<i>INLET</i>	
Boundary Type	Opening
Flow Regime	Subsonic
Mass and Momentum	Opening Pressure and Direction
Relative Pressure	P_in
Flow Direction	Normal to Boundary Condition
Turbulence	Medium (Intensity = 5%)
<i>OUTLET</i>	
Boundary Type	Opening
Flow Regime	Subsonic
Mass and Momentum	Opening Pressure and Direction
Relative Pressure	0 [psi]
Flow Direction	Normal to Boundary Condition
Turbulence	Medium (Intensity = 5%)
<i>WALL</i>	
Mass and Momentum	No Slip Wall
Wall Roughness	Smooth Wall
Global Initialization	
<i>Global Setting</i>	
<i>Initial Condition</i>	
Velocity Type	Cartesian
Static Pressure	Automatic with Value
Relative Pressure	0 [psi]
Turbulence	Medium Intensity and Eddy Viscosity Ratio
Solver Control	
<i>Basic Setting</i>	
Advection Scheme	High Resolution
Transient Scheme	Second Order Backward Euler (Automatic)
Turbulence Numerics	High Resolution
<i>Convergence Control</i>	
Min. Coeff. Loops	1

Max Coeff. Loops	20
<i>Convergence Criteria</i>	
Residual Type	MAX
Residual Target	1 E-5
Conservation Target	0.01
Equation Class Setting	Continuity
Output Control	
<i>Trn Results: Transient Results 1</i>	
Transient Results1	Selected Variables
File Compression	Default
Output Variables List	Absolute Pressure,Velocity,Velocity u,Velocity v,Velocity w,Pressure
Output Frequency	Time Interval
Time Interval	1 [s]
<i>Monitor Options</i>	
Monitor Expression	OutFlow
Expression	massFlow()@OUTLET
<i>Expert Parameter</i>	
<i>Flow Analysis 1</i>	I/OControl
Transient Model and I/O	Transient initialization override
Value	t
Expressions	
P_max	10.5 [psi]
period	30 [s]
P_in	$P_max \cdot \sin(2 \cdot \pi \cdot t / \text{period})$

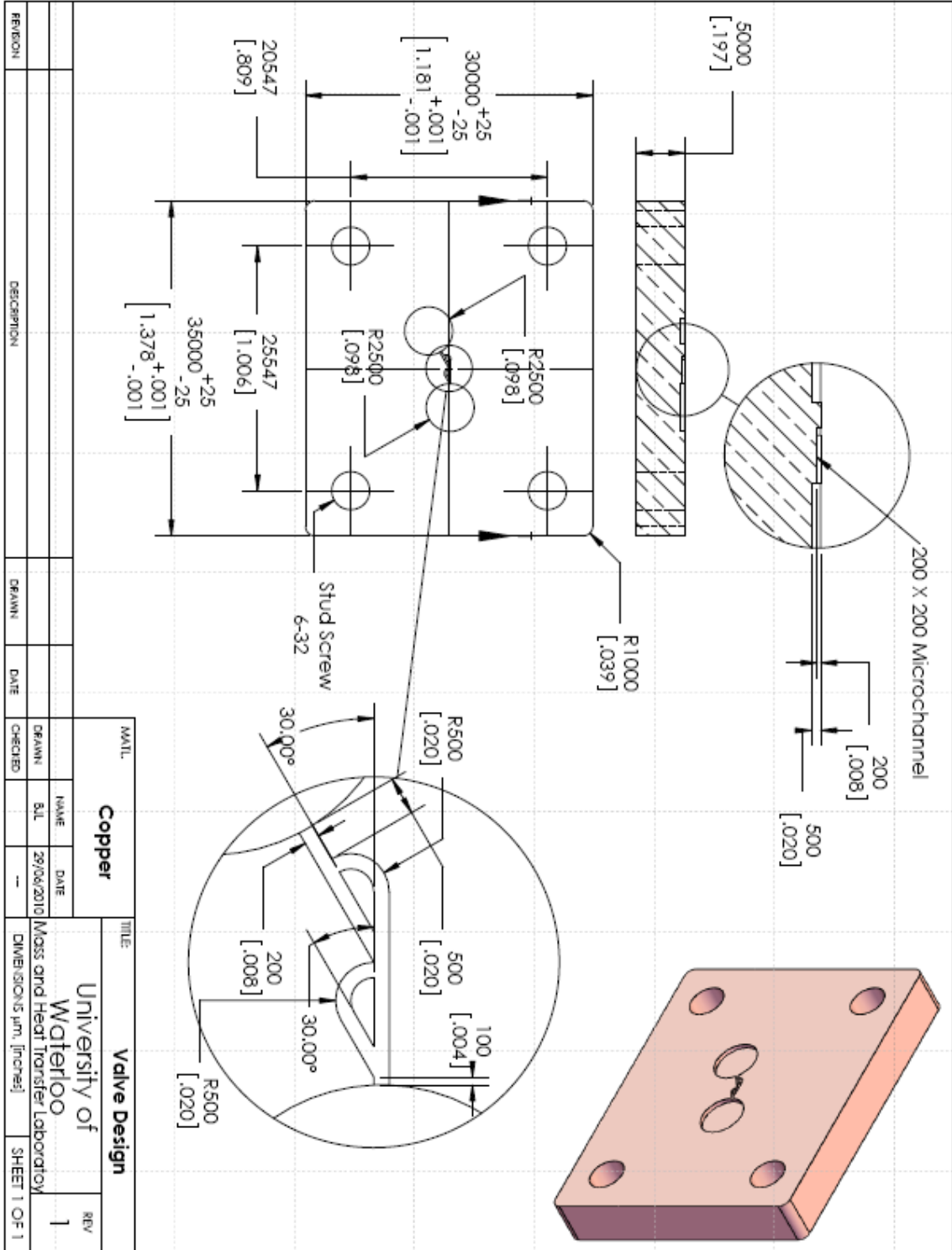






Appendix B

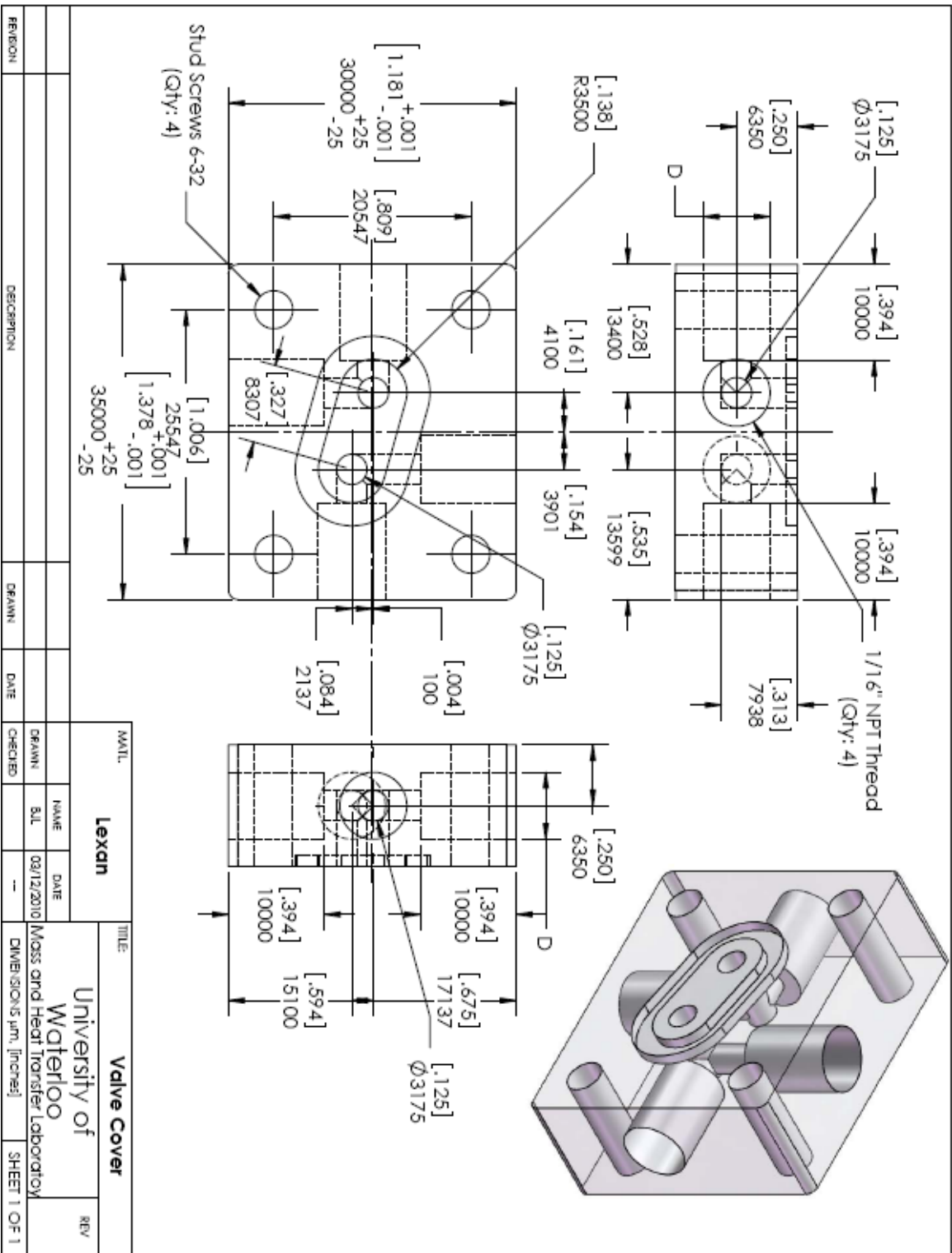
Design: Drawings



REVISION	DESCRIPTION	DRAWN	DATE	CHECKED	DATE

MATERIAL	NAME	DATE	DRAWN	SJL	29/06/2010	CHECKED	---
Copper							

TITLE	REV
Valve Design	1
University of Waterloo	
Mass and Heat Transfer Laboratory	
DIMENSIONS: mm, [inches]	
SHEET 1 OF 1	



MATERIAL: Lexan		TITLE: Valve Cover	
NAME	DATE	NAME	DATE
B.L.	09/12/2010		
DRAWN	CHECKED		
DESCRIPTION	DRAWN	DATE	CHECKED
REVISION			

UNIVERSITY OF
Waterloo
 MASS and Heat Transfer Laboratory
 DIMENSIONS (mm, [inches]) SHEET 1 OF 1

Appendix C

MicroMachining and MasterCAM

MasterCAM Program (ATOMETRIC G4-ULTRA CNC MicroMachining Centers)

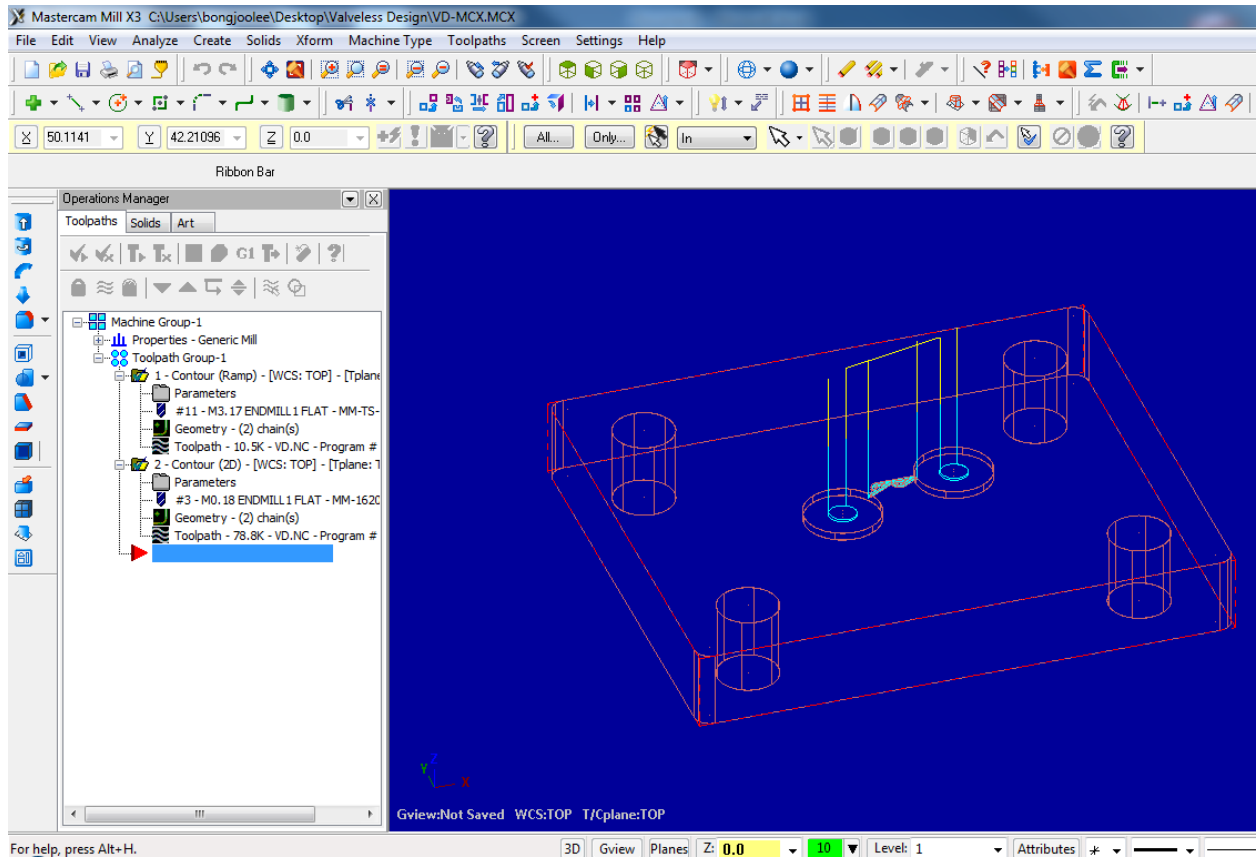
G4-ULTRA

CNC

MicroMachining Centers (<http://www.atometric.com/index-1.html>)

Standard Configurations
<p>Three X, Y, Z axes. Four axes: X, Y, Z plus rotational table. Fives axes: X, Y, Z plus table axes (rotate and trunion). Machines are field upgradeable to add table options.</p>
Maximum Table Load
5 lbs (2.73 kg); Higher payload, as special.
Servo Spindles
<p>100,000 RPM Servo air cooled spindle as standard, 200,000 RPM water chilled servo spindle as option.</p>
Speed and Acceleration
<p>Acc/Decs XYZ of >2 G's; Speed maximum of 30 m/min. Note: Typical applications use Acc/Dec of ~<=1G .</p>
Accuracy
XYZ 0.6 μm to position, ~2 micron along path (dynamic).
Resolution
<p>XYZ 0.1 μm all axes individually. Linear axes have 5 nanometer resolution optical scales.</p>
Repeatability
<p>XYZ 0.3 μm to position, ~1 micron along path (dynamic). Z Z can add 1 micron tool holding variation auto tool change.</p>
Automatic Tool Changer
(# of tools) Fourteen tools per cartridge; With additional cartridges and/or part fixtures,

(14) new tools input < 30 seconds.
Tool position repeatability Validation of tool tip depth within one micron
____ Tool Position Repeatability
Validation of tool tip depth within one micron
____ Conductive Contact Probing
(Standard) Contact probing within one micron.
G-codes supporting application usage.
____ Travel
X__ 101 mm (4 inch) work envelop
Y__ 101 mm (4 inch) work envelop
Z__ 76 mm (3 inch) stroke. 101 mm (4 inch) work envelop w/ table rotation..
____ File Format
G code program storage in .txt files. CAM option programs semi-auto generated from SolidWorks, ACAD, STEP files.
____ User Interface
Macro capabilities User interface for manual, program call and G-code programs. Macros for planarizing, surface probing, tool change, part shifts, peck drilling, etc.
CAM option semi-auto generates complex path multiple-tool part programs.
____ Major Options
Table options for 3, 4, or 5 axes, 200k RPM spindle, CAM software, 5-axis contour milling, additional tool changer and pallet cartridges.
____ Non Contact Confocal Laser
Probe option for non-conducting and translucent/transparent materials. Automatic deployment. Accuracy < 1 micron. G code supported.
____ Coolant System
Flood and directed recirculated filtered coolant, G-code directed.



%	N4100 G0 Z14.8
O0000	N4300 Z15.
(PROGRAM NAME - VD-MCX)	N4500 X20.688 Y15.1
(DATE=DD-MM-YY - 29-06-10	N4700 Z10.
TIME=HH:MM - 06:02)	N4900 G1 Z5. F50.
N100 G21	N5100 X20.784 Y14.691 Z4.978 F40.
N300 G0 G17 G40 G49 G80 G90	N5300 X21.054 Y14.369 Z4.956
(MM-TS-2-1250-S TOOL - 11 DIA.	N5500 X21.44 Y14.202 Z4.933
OFF. - 11 LEN. - 11 DIA. - 3.175)	N5700 X21.859 Y14.225 Z4.911
(GENERIC MILL)	N5900 X22.224 Y14.434 Z4.889
(MACHINE GROUP-1)	N6100 X22.456 Y14.784 Z4.867
N500 T11 M6	N6300 X22.507 Y15.201 Z4.844
N700 G0 G90 G54 X12.687 Y12.863 A0.	N6500 X22.365 Y15.597 Z4.822
S10000 M3	N6700 X22.061 Y15.887 Z4.8
N900 G43 H11 Z15.	N6900 G3 X20.688 Y15.1 R.912
N1100 Z10.	N7100 X22.512 R.912
N1300 G1 Z5. F50.	N7300 X22.061 Y15.887 R.912
N1500 X12.784 Y12.454 Z4.978 F40.	N7500 G1 Z9.8 F60.
N1700 X13.053 Y12.132 Z4.956	N7700 G0 Z15.
N1900 X13.439 Y11.965 Z4.933	N7900 M5
N2100 X13.858 Y11.988 Z4.911	N8100 G91 G28 Z0.
N2300 X14.223 Y12.197 Z4.889	N8300 G28 X0. Y0. A0.
N2500 X14.455 Y12.548 Z4.867	N8500 M01
N2700 X14.506 Y12.965 Z4.844	(MM-1620-0070.011 TOOL - 3 DIA.
N2900 X14.365 Y13.36 Z4.822	OFF. - 3 LEN. - 3 DIA. - .1778)
N3100 X14.061 Y13.651 Z4.8	(GENERIC MILL)
N3300 G3 X12.687 Y12.863 R.913	(MACHINE GROUP-1)
N3500 X14.511 R.912	N8700 T3 M6
N3700 X14.061 Y13.651 R.912	N8900 G0 G90 G54 X15.66 Y14.041 A0.
N3900 G1 Z9.8 F60.	S10000 M3

N9100 G43 H3 Z15.
N9300 Z10.
N9500 G1 Z4.975 F25.
N9700 X15.768 Y14.103
N9900 X17.456 Y15.077
N100 G2 X17.589 Y15. R.089
N300 G3 X18.206 Y14.644 R.411
N500 G1 X18.976 Y15.089
N700 X19.102
N900 X19.226
N1100 Z9.975 F30.
N1300 G0 Z14.975
N1500 Z15.
N1700 Y15.111
N1900 Z10.
N2100 G1 Z4.975 F25.
N2300 X19.102
N2500 X16.58
N2700 G3 X16.224 Y14.494 R.411
N2900 G2 X16.192 Y14.373 R.089
N3100 G1 X15.757 Y14.122
N3300 X15.649 Y14.06
N3500 Z9.975 F30.
N3700 G0 Z14.975
N3900 X15.66 Y14.041
N4100 Z9.975
N4300 G1 Z4.95 F25.
N4500 X15.768 Y14.103
N4700 X17.456 Y15.077

N4900 G2 X17.589 Y15. R.089
N5100 G3 X18.206 Y14.644 R.411
N5300 G1 X18.976 Y15.089
N5500 X19.102
N5700 X19.226
N5900 Z9.95 F30.
N6100 G0 Z14.95
N6300 Z14.975
N6500 Y15.111
N6700 Z9.975
N6900 G1 Z4.95 F25.
N7100 X19.102
N7300 X16.58
N7500 G3 X16.224 Y14.494 R.411
N7700 G2 X16.192 Y14.373 R.089
N7900 G1 X15.757 Y14.122
N8100 X15.649 Y14.06
N8300 Z9.95 F30.
N8500 G0 Z14.95
N8700 X15.66 Y14.041
N8900 Z9.95
N9100 G1 Z4.925 F25.
N9300 X15.768 Y14.103
N9500 X17.456 Y15.077
N9700 G2 X17.589 Y15. R.089
N9900 G3 X18.206 Y14.644 R.411
N100 G1 X18.976 Y15.089
N300 X19.102
N500 X19.226

N700 Z9.925 F30.
N900 G0 Z14.925
N1100 Z14.95
N1300 Y15.111
N1500 Z9.95
N1700 G1 Z4.925 F25.
N1900 X19.102
N2100 X16.58
N2300 G3 X16.224 Y14.494 R.411
N2500 G2 X16.192 Y14.373 R.089
N2700 G1 X15.757 Y14.122
N2900 X15.649 Y14.06
N3100 Z9.925 F30.
N3300 G0 Z14.925
N3500 X15.66 Y14.041
N3700 Z9.925
N3900 G1 Z4.9 F25.
N4100 X15.768 Y14.103
N4300 X17.456 Y15.077
N4500 G2 X17.589 Y15. R.089
N4700 G3 X18.206 Y14.644 R.411
N4900 G1 X18.976 Y15.089
N5100 X19.102
N5300 X19.226
N5500 Z9.9 F30.
N5700 G0 Z14.9
N5900 Z14.925
N6100 Y15.111
N6300 Z9.925

N6500 G1 Z4.9 F25.
N6700 X19.102
N6900 X16.58
N7100 G3 X16.224 Y14.494 R.411
N7300 G2 X16.192 Y14.373 R.089
N7500 G1 X15.757 Y14.122
N7700 X15.649 Y14.06
N7900 Z9.9 F30.
N8100 G0 Z14.9
N8300 X15.66 Y14.041
N8500 Z9.9
N8700 G1 Z4.875 F25.
N8900 X15.768 Y14.103
N9100 X17.456 Y15.077
N9300 G2 X17.589 Y15. R.089
N9500 G3 X18.206 Y14.644 R.411
N9700 G1 X18.976 Y15.089
N9900 X19.102
N100 X19.226
N300 Z9.875 F30.
N500 G0 Z14.875
N700 Z14.9
N900 Y15.111
N1100 Z9.9
N1300 G1 Z4.875 F25.
N1500 X19.102
N1700 X16.58
N1900 G3 X16.224 Y14.494 R.411
N2100 G2 X16.192 Y14.373 R.089

N2300 G1 X15.757 Y14.122
N2500 X15.649 Y14.06
N2700 Z9.875 F30.
N2900 G0 Z14.875
N3100 X15.66 Y14.041
N3300 Z9.875
N3500 G1 Z4.85 F25.
N3700 X15.768 Y14.103
N3900 X17.456 Y15.077
N4100 G2 X17.589 Y15. R.089
N4300 G3 X18.206 Y14.644 R.411
N4500 G1 X18.976 Y15.089
N4700 X19.102
N4900 X19.226
N5100 Z9.85 F30.
N5300 G0 Z14.85
N5500 Z14.875
N5700 Y15.111
N5900 Z9.875
N6100 G1 Z4.85 F25.
N6300 X19.102
N6500 X16.58
N6700 G3 X16.224 Y14.494 R.411
N6900 G2 X16.192 Y14.373 R.089
N7100 G1 X15.757 Y14.122
N7300 X15.649 Y14.06
N7500 Z9.85 F30.
N7700 G0 Z14.85
N7900 X15.66 Y14.041

N8100 Z9.85
N8300 G1 Z4.825 F25.
N8500 X15.768 Y14.103
N8700 X17.456 Y15.077
N8900 G2 X17.589 Y15. R.089
N9100 G3 X18.206 Y14.644 R.411
N9300 G1 X18.976 Y15.089
N9500 X19.102
N9700 X19.226
N9900 Z9.825 F30.
N100 G0 Z14.825
N300 Z14.85
N500 Y15.111
N700 Z9.85
N900 G1 Z4.825 F25.
N1100 X19.102
N1300 X16.58
N1500 G3 X16.224 Y14.494 R.411
N1700 G2 X16.192 Y14.373 R.089
N1900 G1 X15.757 Y14.122
N2100 X15.649 Y14.06
N2300 Z9.825 F30.
N2500 G0 Z14.825
N2700 X15.66 Y14.041
N2900 Z9.825
N3100 G1 Z4.8 F25.
N3300 X15.768 Y14.103
N3500 X17.456 Y15.077
N3700 G2 X17.589 Y15. R.089

N3900 G3 X18.206 Y14.644 R.411

N4100 G1 X18.976 Y15.089

N4300 X19.102

N4500 X19.226

N4700 Z9.8 F30.

N4900 G0 Z14.8

N5100 Z14.825

N5300 Y15.111

N5500 Z9.825

N5700 G1 Z4.8 F25.

N5900 X19.102

N6100 X16.58

N6300 G3 X16.224 Y14.494 R.411

N6500 G2 X16.192 Y14.373 R.089

N6700 G1 X15.757 Y14.122

N6900 X15.649 Y14.06

N7100 Z9.8 F30.

N7300 G0 Z15.

N7500 M5

N7700 G91 G28 Z0.

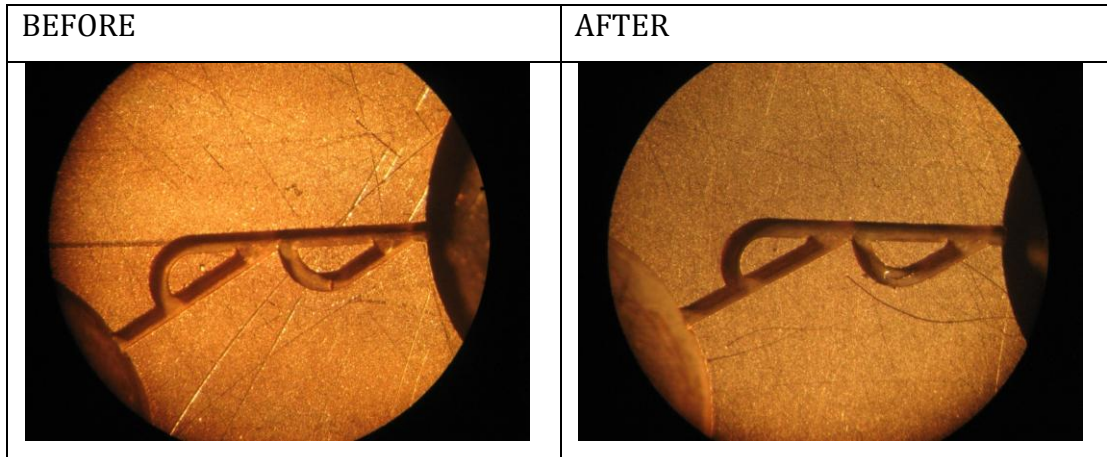
N7900 G28 X0. Y0. A0.

N8100 M30

%

Actual Manufactured Part

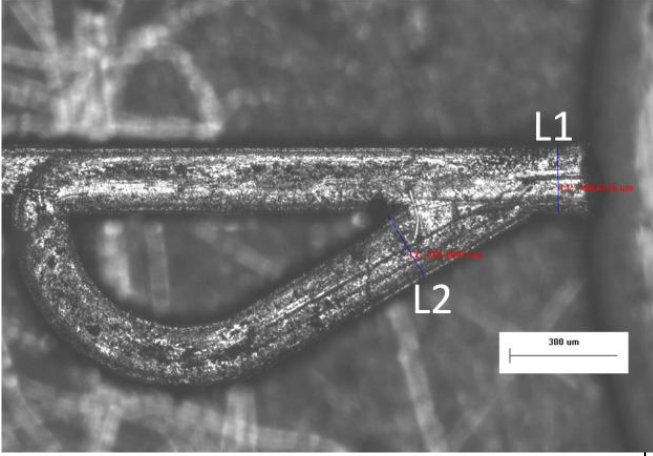
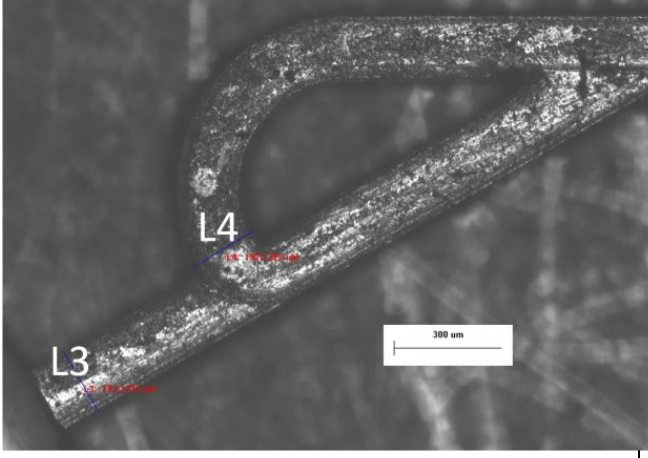
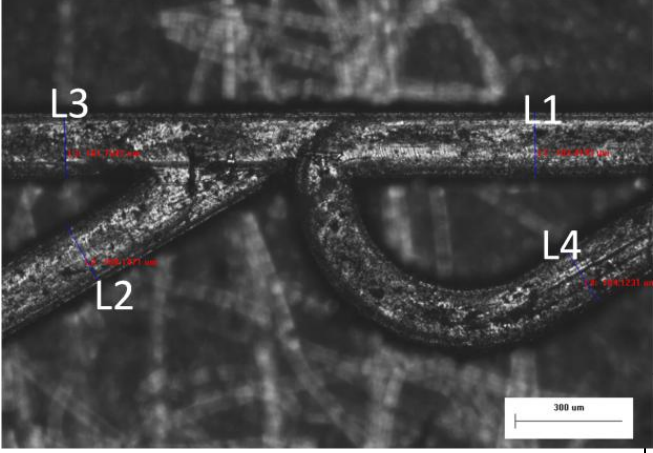
Polishing: Prototype of the Valvular Conduit



Before initiating the experiments, there were visible scratches on the designed prototype. So, I took it to materials lab and polished it. Also, I went back to the machine shop guys to get feedback on how to improve the surface (senior machine technician, Rick was very helpful).

As you can see there is a significant difference after polishing.

Actual approximate measurements from microscope software

				Features	Value [μm]	Min. Tol. [μm]	Max. Tol. [μm]
				L1	190.6116	-0.001	0.001
				L2	201.6807	-0.001	0.001
Features	Value [μm]	Min. Tol. [μm]	Max. Tol. [μm]				
L3	193.3735	-0.001	0.001				
L4	192.1322	-0.001	0.001				
				Features	Value [μm]	Min. Tol. [μm]	Max. Tol. [μm]
				L1	183.4193	-0.001	0.001
				L2	189.1471	-0.001	0.001
				L3	181.7547	-0.001	0.001
				L4	184.1231	-0.001	0.001

Appendix D

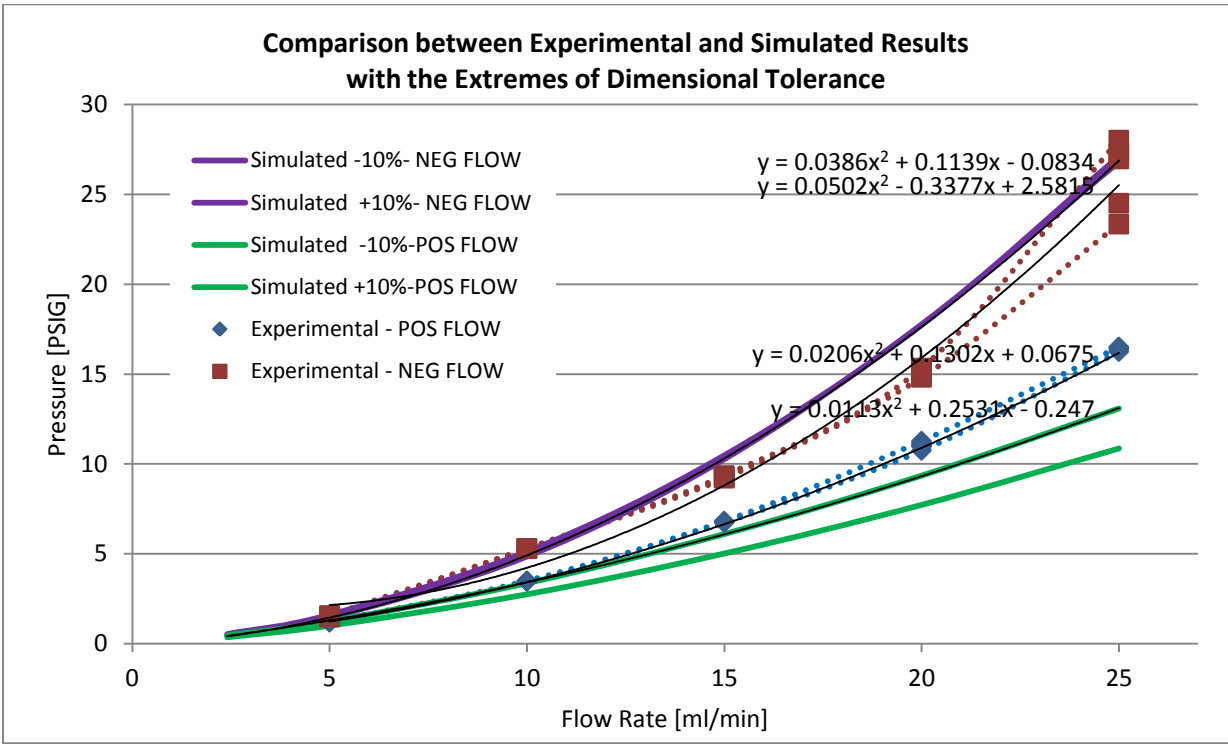
Comparing Experimented and Simulated Results

EXPERIMENTAL (Pressure sensor) NEW COVER!!!! 30 PSI NEW volt meter								
Flow Rate [ml/min]	Experimental - POS FLOW				Experimental - NEG FLOW			
			MAX	MIN			MAX	MIN
	mV	PSI			mV	PSI		
5	4.0204	1.20612			5.2283	1.56849		
5	4.0181	1.20543			4.9467	1.48401		
5	4.0001	1.20003	1.20612	1.20003	4.9701	1.49103	1.56849	1.48401
10	11.648	3.4944			17.6614	5.29842		
10	11.5448	3.46344			17.6488	5.29464		
10	11.5951	3.47853	3.4944	3.46344	17.5967	5.27901	5.29842	5.27901
15	22.7401	6.82203			31.179	9.3537		
15	22.6255	6.78765			30.94	9.282		
15	22.5106	6.75318			30.688	9.2064		
15	22.4701	6.74103	6.82203	6.74103	30.784	9.2352	9.3537	9.2064
20	37.586	11.2758			49.389	14.8167		
20	37.069	11.1207			50.388	15.1164		
20	35.822	10.7466			50.032	15.0096		
20	37.343	11.2029			49.886	14.9658		
20	36.59	10.977			51.049	15.3147		
20	36.592	10.9776			51.115	15.3345		
20	36.655	10.9965	11.2758	10.7466	50.635	15.1905	15.3345	14.8167
25	54.978	16.4934			81.7	24.51		
25	54.157	16.2471			77.81	23.343		
25	54.54	16.362			90.875	27.2625		
25	55.039	16.5117			89.9	26.97		
25	54.831	16.4493	16.5117	16.2471	93.399	28.0197	28.0197	23.343

Simulated Results from ANSYS-CFX Workbench

Density		997	kg/m ³				
Kinematic Viscosity		1.00E+00	mm ² /s				
Cross-Sectional Area		0.04	mm ²				
Hydraulic Diameter (Dh)		0.2	mm				
Flow Rate		Normal Speed		Pressure Differences [Pa]			
ml/min	mm ³ /s	mm/s	Reynolds	Simulated – Positive	PSI	Simulated – Negative	PSI
2.4	40	1000	199.2032	2798.964	0.405955	3316.297	0.480988
5	83.33333	2083.333	415.0066	7660.06	1.110998	10540.03	1.528702
10	166.6667	4166.667	830.0133	20823.22	3.020153	34582.99	5.015839
15	250	6250	1245.02	37915.34	5.499155	72691.8	10.54305
20	333.3333	8333.333	1660.027	58408.8	8.47148	124032.6	17.98941
25	416.6667	10416.67	2075.033	82115.3	11.90982	193785.2	28.10617

Tolerance -10%				Tolerance +10%				
	SIMULATED				SIMULATED			
Flow Rate	Simulated -10%-POS FLOW		Simulated -10%- NEG FLOW		Simulated +10%-POS FLOW		Simulated +10%-NEG FLOW	
ml/min	Pa	PSI	Pa	PSI	Pa	PSI	Pa	PSI
2.4	3230.704	0.468574	3661.819	0.531102	2501.612	0.362828	3046.201	0.441814
5	8667.48	1.257112	11097.22	1.609516	6955.24	1.008772	9991.416	1.449132
10	23255.13	3.372871	35254.39	5.113217	18982.79	2.753221	33453.33	4.851995
15	42099.4	6.106002	72265.7	10.48125	34590.99	5.016999	70809.9	10.27011
20	64505	9.355659	122301.4	17.73832	53239.4	7.721722	122515	17.7693
25	90242.2	13.08852	187023.4	27.12545	74843.3	10.8551	184926.8	26.82136



Appendix E

Uncertainty Analysis

An uncertainty analysis of the experimental method, apparatus and data is performed in the following sections. Following an assessment of the accuracy of each of the instruments and sensors used in the experiments, the impact of these uncertainties on the reported values of pressure and flow rate is presented.

E.1 Method

The procedure used for the uncertainty analysis is based on the method described by Moffat [39]. Given an experimental test program where a quantity Y is determined from a set of measured values, X_j :

$$Y = Y(X_1, X_2, X_3, \dots, X_N) \quad \text{E-1}$$

where each measured value X_j has an associated uncertainty represented by the notation δX_j , the effect of the uncertainty in X_j on the result Y is calculated by:

$$\delta Y_{X_j} = \frac{\partial Y}{\partial X_j} \delta X_j \quad \text{E-2}$$

where δY_{X_j} refers to the uncertainty in Y as a result of the uncertainty in the X_j measurement. When Y depends on a number of measured quantities and this dependence can be expressed in the form:

$$Y = X_1^{C_1} \cdot X_2^{C_2} \cdot X_3^{C_3} \dots \cdot X_N^{C_N} \quad \text{E-3}$$

The overall uncertainty is determined from the uncertainties of each of the individual measurements:

$$\frac{\delta Y}{Y} = \left\{ \left(C_1 \cdot \frac{\delta X_1}{X_1} \right)^2 + \left(C_2 \cdot \frac{\delta X_2}{X_2} \right)^2 + \left(C_3 \cdot \frac{\delta X_3}{X_3} \right)^2 + \dots + \left(C_N \cdot \frac{\delta X_N}{X_N} \right)^2 \right\}^{1/2} \quad \text{E-4}$$

The result of this equation is the overall uncertainty Y expressed as a percentage. The following section describes the uncertainty associated with the instrumentation and method used in the measurement of each of the individual quantities in the experimental test program.

E.2 Uncertainty in Measured Values

E.2.1 Pressure

The pressure readings from the PX26 transducers, which converts the pressure reading to voltage signal that is measured by the Fluke Model 187 Multimeter. The pressure reading is calculated using:

$$P = C_{PX26} \cdot \bar{V}_{pressure} \quad \mathbf{E-5}$$

where C_{PX26} is a constant correlation coefficient from the transducers. The uncertainty in the pressure measurement is determined by:

$$\frac{\delta P}{P} = \left\{ \left(\frac{\delta C_{PX26}}{C_{PX26}} \right)^2 + \left(\frac{\delta \bar{V}_{pressure}}{\bar{V}_{pressure}} \right)^2 \right\}^{1/2} \quad \mathbf{E-6}$$

The accuracy of the PX26 transducer is determined from its user's manual [40]:

$$\frac{\delta C_{PX26}}{C_{PX26}} = 1\% \text{ of full scale} \quad \mathbf{E-7}$$

Also, the accuracy of the Fluke Model 187 Multimeter to read the voltage signal is found in the user's manual:

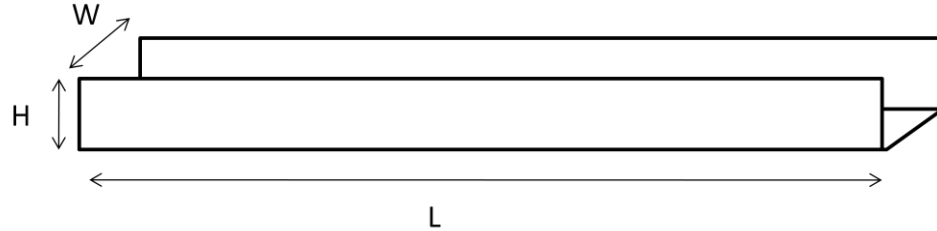
$$\frac{\delta V_{pressure}}{V_{pressure}} = 0.025\% \text{ DC voltage} \quad \mathbf{E-8}$$

Based on these expressions the uncertainty in the pressure readings can be calculated by:

$$\frac{\delta P}{P} = \{(0.01)^2 + (0.00025)^2\}^{1/2} = 1.0003 \% \quad \mathbf{E-9}$$

E.2.2 Dimensions

The prototype of the non-mechanical valvular conduit was fabricated by ATOMETRIC G4-ULTRA CNC micro-milling machine with Performance Micro Tool (PMT) end mills. ATOMETRIC G4-ULTRA CNC micro-milling machine has a maximum accuracy tolerance of ± 0.6 [μm] to position ($\varepsilon_{position}$) and ± 2 [μm] along the dynamic path (ε_{path}) [38]. Also, the PMT 0.007" 2 Flute end mill standard length has a diameter tolerance (ε_{tool}) of ± 0.0005 " (12.7 [μm])[41].



Therefore, the cross-sectional area can be evaluated by:

$$A = W \cdot H \quad \mathbf{E-10}$$

where W is the width and H is the height/depth of the channel. Thus, the uncertainty in the dimensional measurement is determined by:

$$\frac{\delta A}{A} = \left\{ \left(\frac{\delta W}{W} \right)^2 + \left(\frac{\delta H}{H} \right)^2 \right\}^{1/2} \quad \mathbf{E-11}$$

The accuracy of the channel width and height is determined by combining the tolerance of the end mill tool, and the milling position and dynamic path:

$$\delta W = \varepsilon_{position} + \varepsilon_{path} + \varepsilon_{tool} = 15.3 [\mu\text{m}] \quad \mathbf{E-12}$$

$$\delta H = \varepsilon_{position} + \varepsilon_{path} = 2.6 [\mu\text{m}] \quad \mathbf{E-12}$$

Since, the cross sectional area is known to be $200 [\mu\text{m}] \times 200 [\mu\text{m}]$; therefore, the width of the channel is $W = 200 [\mu\text{m}]$ and the depth of the channel is $H = 200 [\mu\text{m}]$. Thus, based on these expressions the uncertainty in the volume can be calculated by:

$$\frac{\delta A}{A} = \left\{ \left(\frac{15.3}{200} \right)^2 + \left(\frac{2.6}{200} \right)^2 \right\}^{1/2} = 7.760 \% \quad \text{E-13}$$

E.2.3 Flow Rate

The flow rate for the experiment rig was provided from the HARVARD Apparatus PHD 22/2000 Syringe Pump. The syringe pump is programmed to supply a specified input flow rate in ml/min as mentioned in Section 4.3. The accuracy of syringe pump is $\pm 1\%$ [42]. Since, the fluid flows through the micro-channel valvular conduit design, the volumetric flow rate can be evaluated with product of the cross-sectional area (A) and velocity (v):

$$\dot{V} = A \cdot v \quad \text{E-15}$$

Therefore, the uncertainty of the flow rate measurement is:

$$\frac{\delta \dot{V}}{\dot{V}} = \left\{ \left(\frac{\delta A}{A} \right)^2 + \left(\frac{\delta v}{v} \right)^2 \right\}^{1/2} \quad \text{E-16}$$

With velocity provided by the pump, the uncertainty of the velocity was assumed:

$$\frac{\delta v}{v} = 1 \% \quad \text{E-17}$$

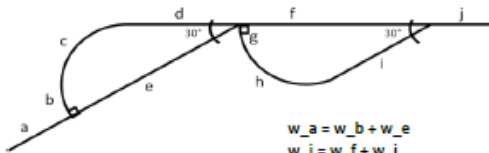
From E.2.2, the uncertainty of the cross-sectional area is 7.760 %. Thus, based on these expressions the uncertainty in the flow rate can be calculated:

$$\frac{\delta \dot{V}}{\dot{V}} = \{(0.07760)^2 + (0.01)^2\}^{1/2} = 7.824 \% \quad \text{E-18}$$

Appendix F

Pressure Resistance Calculations

ρ 997 kg/m³
 g 9.81 m/s²
 μ 8.90E-04 kg*m/s
 D_h 0.0002 m
 R 0.0005 m



$$w_a = w_b + w_e$$

$$w_j = w_f + w_i$$

$$w_c = w_d + w_e$$

$$w_d = w_d + w_e$$

POSITIVE FLOW DIRC'N

Node	Flow Rate (m/s)
a → j	
w _a	0.9565
w _b	0.02283
w _c	0.02283
w _d	0.02283
w _e	0.93367
w _{c'}	0.9565
w _f	0.9565
w _g	0
w _h	0
w _i	0
w _j	0.9565

NEGATIVE FLOW DIRC'N

Node	Flow Rate (m/s)
j → a	
w _a	0.9565
w _b	0.9565
w _c	0.9565
w _d	0.9565
w _e	0
w _{d'}	0.9565
w _f	0.6302
w _g	0.3263
w _h	0.3263
w _i	0.3263
w _j	0.9565

POSITIVE FLOW DIRC'N

KE _a =	$((\rho \cdot w_a^2) / (2 \cdot g))$	456.0738
KE _b =	$((\rho \cdot w_b^2) / (2 \cdot g))$	0.259823

KE _e =	$((\rho \cdot w_e^2) / (2 \cdot g))$	434.5622
KE _h =		53.07614

a/b/e Diverging Wye
pg 280 α 90 °

1.570796 rad

1. Branch (pg 280)

$$w_b/w_a = 0.023868 <$$

$$\xi_{a,b} = \Delta H_b / KE_b = \xi_{b,a} \cdot A'$$

$$\xi_{b,a} = f(w_b/w_a)$$

1

No. 2

0.8 A'

1

w _b /w _a	$\xi_{b,a}$
0	1
0.1	1

$$\Delta H_b = \xi_{a,b} \cdot A' \cdot KE$$

456.074 kg/m-s²

2. Main Passage (pg 282)

$$w_e/w_a = 0.976132$$

$$\xi_{a,e} = \Delta H_{e1} / KE$$

$$\xi_{a,e} = f(w_e/w_a)$$

0.0477365

w _b /w _a	$\xi_{b,a}$
0.8	0.4
1	0

$$\Delta H_{e1} = \xi_{a,e} \cdot KE$$

21.7714 kg/m-s²

b/c/d Smooth Bends Arbitrary Angle (Low Reynolds)

pg. 210 δ 60 °
1.047198 rad
Re_b= $\rho \cdot w_b \cdot D_h / \mu$
Re_b 5.114946

$$Re'_b = Re_b \cdot (D_h / 2R)^{0.5}$$

$$Re'_b = 2.287473$$

$$\xi_c = \Delta H_c / KE_b = \lambda \cdot R / D_h \cdot \delta$$

$$\xi_c = \lambda \cdot R / D_h \cdot \delta = 13.675153$$

$$50 < Re'_b < 600$$

$$\lambda = 20 / (Re_b)^{0.65} \cdot (D_h / (2R))^{0.175}$$

$$\lambda = 5.223524$$

$$\Delta H_c = \xi_c \cdot KE_b$$

3.55311 kg/m-s²

d/e/c' Converging Wye

α 30 °
0.523599 rad

1. Branch (pg 260)

$$w_e/w_{c'} = 0.976132$$

$$\xi_{c',e} = \Delta H_{e2} / KE$$

$$\xi_{c',e} = f(w_e/w_{c'}) = 0.3010288$$

w _b /w _a	$\xi_{b,a}$
0.9	0.4
1	0.27

$$\Delta H_{e2} = \xi_{c',e} \cdot KE$$

137.291 kg/m-s²

2. Main Passage (pg 261)

$$w_e/w_{c'} = 0.976132$$

$$\xi_{c',d} = \Delta H_d / KE$$

$$\xi_{c',d} = f(w_e/w_{c'}) = -0.6783952$$

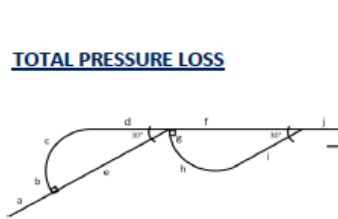
w _b /w _a	$\xi_{b,a}$
0.9	-0.45
1	-0.75

$$\Delta H_d = \xi_{c',d} \cdot KE$$

-309.4 kg/m-s²

c'/g/f pg 280	Diverging Wye α	90 ° 1.570796 rad	1. Branch (pg 280)		No. 2			
			$w_g/w_{c'}$	0 <	0.8 A'	1		
			$\xi_{c'.g} = \Delta H_{g}/KE = \xi_{c'.g} \cdot A'$		$w_g/w_{c'}$	$\xi_{c'.g}$	$\Delta H_g = \xi_{c'.g} \cdot A' \cdot KE$	456.074 kg/m-s ²
			$\xi_{c'.g} = f(w_g/w_{c'})$	1	0	1		
					0.1	1		
			2. Main Passage (pg 282)					
			$w_f/w_{c'}$	1	$w_f/w_{c'}$	$\xi_{c'.f}$	$\Delta H_{f1} = \xi_{c'.f} \cdot KE$	0 kg/m-s ²
			$\xi_{c'.f} = \Delta H_{f1}/KE$	0	0	0		
			$\xi_{c'.f} = f(w_f/w_{c'})$	0	0	0		
g/h/i pg. 210	Smooth Bends Arbitrary Angle (Low Reynolds)	60 ° 1.047198 rad	Re'_h = Re_h * (D_h/2*R) ^{0.5}		50 < Re'_b < 600		$\lambda = 20 / ((Re_h)^{0.65} * (D_h / (2*R))^{0.175})$	
			$Re_h = \rho * w_h * D_h / \mu$	0			λ	#DIV/0!
			$\xi_c = \Delta H_h / KE_b = \lambda * R / D_h * \delta$				$\Delta H_h = \xi_c * KE_h$	0 kg/m-s ²
			$\xi_c = \lambda * R / D_h * \delta$	#DIV/0!				
f/i/j	Converging Wye α	30 ° 0.523599 rad	1. Branch (pg 260)		2. Main Passage (pg 261)			
			w_i/w_j	0	w_i/w_j	0		
			$\xi_{j.i} = \Delta H_i / KE$		$\xi_{j.f} = \Delta H_{f2} / KE$		$\Delta H_{f2} = \xi_{j.f} \cdot KE$	0 kg/m-s ²
			$\xi_{c'.e} = f(w_e/w_{c'})$	-1	w_b/w_a	$\xi'_{b.a}$	$\Delta H_i = \xi_{j.i} \cdot KE$	-456.07 kg/m-s ²
					0	-1		
					0	-1		
					0	0		
					0	0		

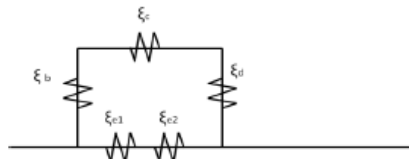
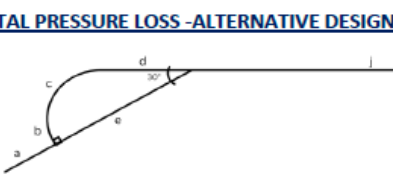
TOTAL PRESSURE LOSS



ΔH_b	ΔH_c	ΔH_d	ξ_b	ξ_c	ξ_d
456.0738	3.553114	-309.398	1755.327	13.67515	-1190.8056
ΔH_{e1}	ΔH_{e2}		ξ_{e1}	ξ_{e2}	
21.77138	137.2913		0.0501	0.31593	
ΔH_{f1}	ΔH_{f2}		ξ_{f1}	ξ_{f2}	
0	0		0	0	
ΔH_g	ΔH_h	ΔH_i	ξ_g	ξ_h	ξ_i
456.0738	0	-456.074	8.592822	0	-8.5928217

ΔH_{b+c+d}	150.2286	$\xi_{b+c+d} = \Delta H_{b+c+d} / KE_b$	578.1969		
ΔH_{e1+e2}	159.0627	$\xi_{e1+e2} = \Delta H_{e1+e2} / KE_e$	0.36603		
ΔH_{f1+f2}	0	$\xi_{f1+f2} = \Delta H_{f1+f2} / KE_e$	0	$\Delta H_{total} = \xi_{total} \cdot KE$	158.8429 kg/m-s ²
ΔH_{g+h+i}	0	$\xi_{g+h+i} = \Delta H_{g+h+i} / KE_g$	0		
$\xi_{total} = (\xi_{b+c+d} \wedge -0.5 + \xi_{e1+e2} \wedge -0.5) \wedge -2 + (\xi_{f1+f2} \wedge -0.5 + \xi_{g+h+i} \wedge -0.5) \wedge -2$			0.348283		

TOTAL PRESSURE LOSS - ALTERNATIVE DESIGN

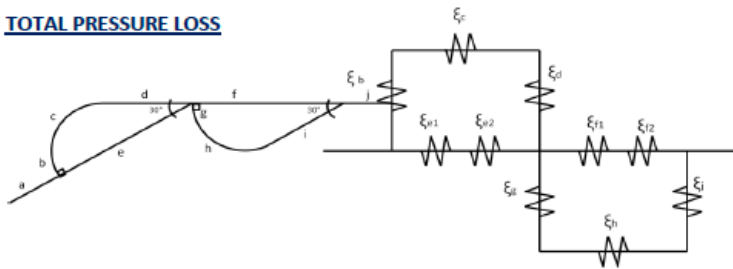


ΔH_{b+c+d}	150.2286	$\xi_{b+c+d} = \Delta H_{b+c+d} / KE_b$	578.1969		
ΔH_{e1+e2}	159.0627	$\xi_{e1+e2} = \Delta H_{e1+e2} / KE_e$	0.36603		
$\xi_{total alt} = (\xi_{b+c+d} \wedge -0.5 + \xi_{e1+e2} \wedge -0.5) \wedge -2$			0.348283	$\Delta H_{total} = \xi_{total} \cdot KE$	158.8429 kg/m-s ²

NEGATIVE

KE=	$((\rho \cdot w_a^2)/(2 \cdot g))$	456.0738							
KE_c=	$((\rho \cdot w_b^2)/(2 \cdot g))$	456.0738	KE_f=	$((\rho \cdot w_b^2)/(2 \cdot g))$	197.9803				
KE_h=	$((\rho \cdot w_h^2)/(2 \cdot g))$	53.07614	KE_e=	$((\rho \cdot w_h^2)/(2 \cdot g))$	0				
j/i/f pg 280	Diverging Wye α	30 ° 0.523599 rad	1. Branch (pg 280) w_i/w_j	0.34114	<	0.8 A'	1		
			$\xi_{j,i} = \Delta H_i / KE = \xi_{j,i} \cdot A'$					$\Delta H_i = \xi_{j,i} \cdot A' \cdot KE$	242.008 kg/m-s ²
			$\xi_{j,i} = f(w_i/w_j)$	0.530633		w_i/w_j	$\xi_{j,i}$		
							0.2 0.7 0.4 0.46		
			2. Main Passage (pg 282) w_f/w_j	0.65886				$\Delta H_{f2} = \xi_{j,f} \cdot KE$	21.9955 kg/m-s ²
			$\xi_{j,f} = \Delta H_{f2} / KE$						
			$\xi_{j,f} = f(w_f/w_j)$	0.048228		w_f/w_j	$\xi_{j,f}$		
							0.6 0.06 0.8 0.02		
i/h/g pg. 210	Smooth Bends Arbitrary Angle (Low Reynolds) δ	60 ° 1.047198 rad	Re'_h = $\rho \cdot w_h \cdot D_h / \mu$	Re'_h = $Re_h \cdot (D_h / 2 \cdot R)^{0.5}$	50 < Re'_b < 600	$\lambda = 20 / (Re_h)^{0.65} \cdot (D_h / 2 \cdot R)^{0.175}$			
			Re_b = 73.10587	Re'_h = Re'_l = 32.69394		$\lambda = 0.927131$			
			$\xi_h = \Delta H_h / KE = \lambda \cdot R / D_h \cdot \delta$	$\xi_h = \lambda \cdot R / D_h \cdot \delta$				$\Delta H_h = \xi_c \cdot KE_h$	128.828 kg/m-s ²
				2.427224					
f/g/d'	Converging Wye α	90 ° 1.570796 rad	1. Branch (pg 266) w_g/w_d'	0.34114				$\Delta H_g = \xi_{d',g} \cdot KE$	53.0266 kg/m-s ²
			$\xi_{d',g} = \Delta H_g / KE$						
			$\xi_{d',g} = f(w_g/w_d')$	0.116268		w_g/w_d'	$\xi_{d',g}$		
							0.3 -0.11 0.4 0.44		
			2. Main Passage (pg 266) w_g/w_d'	0.34114				$\Delta H_{f1} = \xi_{d',f} \cdot KE$	188.318 kg/m-s ²
			$\xi_{d',f} = \Delta H_{f1} / KE$						
			$\xi_{d',f} = f(w_d'/w_f)$	0.412912		w_b/w_a	$\xi_{d',f}$		
							0.3 0.38 0.4 0.46		
d'/e/d pg 280	Diverging Wye α	30 ° 0.523599 rad	1. Branch (pg 280) w_e/w_d'	0 <	0.8 A'	No. 2	1	$\Delta H_{e2} = \xi_{d',e} \cdot A' \cdot KE$	456.074 kg/m-s ²
			$\xi_{d',e} = \Delta H_{e2} / KE = \xi_{d',e} \cdot A' \cdot KE$						
			$\xi_{d',e} = f(w_e/w_d')$	1		w_e/w_d'	$\xi_{d',e}$		
							0 1 0.1 0.94		
			2. Main Passage (pg 282) w_d/w_d'	1				$\Delta H_d = \xi_{d',d} \cdot KE$	0 kg/m-s ²
			$\xi_{d',d} = \Delta H_d / KE$						
			$\xi_{d',d} = f(w_e/w_a)$	0		w_d/w_d'	$\xi_{d',d}$		
							0.8 0.02 1 0		
d/c/b pg. 210	Smooth Bends Arbitrary Angle (Low Reynolds) δ	60 ° 1.047198 rad	Re'_d = $\rho \cdot w_d \cdot D_h / \mu$	Re'_d = $Re_d \cdot (D_h / 2 \cdot R)^{0.5}$	50 < Re'_b < 600	$\lambda = 20 / (Re_d)^{0.65} \cdot (D_h / 2 \cdot R)^{0.175}$			
			Re_d = $\rho \cdot w_d \cdot 2.14E+02$	Re'_d = 95.83742		$\lambda = 0.460837$			
			$\xi_c = \Delta H_c / KE = \lambda \cdot R / D_h \cdot \delta$	$\xi_c = \lambda \cdot R / D_h \cdot \delta$				$\Delta H_c = \xi_c \cdot KE_c$	550.238 kg/m-s ²
				1.206468					
e/b/a	Converging Wye α	90 ° 1.570796 rad	1. Branch (pg 266) w_b/w_a	1	Table 7-4 A		0.6	$\Delta H_b = \xi_{a,b} \cdot KE$	547.289 kg/m-s ²
			$\xi_{a,b} = \Delta H_b / KE = A' \cdot \xi_{a,b}$						
			$\xi_{a,b} = f(w_b/w_a)$	2		w_b/w_a	$\xi_{a,b}$		
							0.9 1.8 1 2		
			2. Main Passage (pg 266) w_b/w_a	1				$\Delta H_{e1} = \xi_{a,e} \cdot KE$	250.841 kg/m-s ²
			$\xi_{a,e} = \Delta H_{e1} / KE$						
			$\xi_{a,e} = f(w_b/w_a)$	0.55		w_b/w_a	$\xi_{a,e}$		
							0.9 0.59 1 0.55		

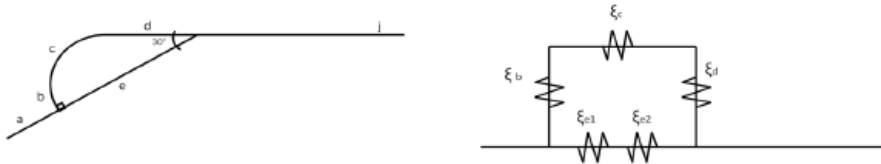
TOTAL PRESSURE LOSS



ΔH_b	ΔH_c	ΔH_d	ξ_b	ξ_c	ξ_d
547.2885	550.2384	0	1.2	1.206468	0
ΔH_{e1}	ΔH_{e2}		ξ_{e1}	ξ_{e2}	
250.8406	456.0738		--	--	
ΔH_{f1}	ΔH_{f2}		ξ_{f1}	ξ_{f2}	
188.3182	21.99549		0.951197	0.111099	
ΔH_g	ΔH_h	ΔH_i	ξ_g	ξ_h	ξ_i
53.02662	128.8277	242.0076	0.999067	2.427224	4.5596306

ΔH_{b+c+d}	1097.527	$\xi_{b+c+d} = \Delta H_{b+c+d} / KE_b$	2.406468		
ΔH_{e1+e2}	706.9144	$\xi_{e1+e2} = \Delta H_{e1+e2} / KE_e$	--		
ΔH_{f1+f2}	210.3137	$\xi_{e1+e2} = \Delta H_{e1+e2} / KE_e$	1.062296		
ΔH_{g+h+i}	423.8619	$\xi_{b+c+d} = \Delta H_{b+c+d} / KE_b$	7.985922		
$\xi_{total} = (\xi_{b+c+d} \wedge -0.5 + \xi_{e1+e2} \wedge -0.5) \wedge -2 + (\xi_{f1+f2} \wedge -0.5 + \xi_{g+h+i} \wedge -0.5) \wedge -2$			2.97684	$\Delta H_{total} = \xi_{total} * KE$	1357.659 kg/m-s ²

TOTAL PRESSURE LOSS -ALTERNATIVE DESIGN



ΔH_{b+c+d}	1097.527	$\xi_{b+c+d} = \Delta H_{b+c+d} / KE_b$	2.406468		
ΔH_{e1+e2}	706.9144	$\xi_{e1+e2} = \Delta H_{e1+e2} / KE_e$	--		
$\xi_{total alt} = (\xi_{b+c+d} \wedge -0.5 + \xi_{e1+e2} \wedge -0.5) \wedge -2$			2.406468	$\Delta H_{total} = \xi_{total} * KE$	1097.527 kg/m-s ²

Bibliography

- [1] PC Power & Cooling. *Operating Temperature vs System Reliability*. An OCZ Technology Group Company, Copyright 1997-2011 Accessed: May 2011.
<http://www.pcpower.com/technology/optemps/>
- [2] Intel Corporation. *Thermal Management Boxed Intel Pentium D Processor*. Intel Corporation, 2011 . Accessed: May 2011.
<http://www.intel.com/cd/channel/reseller/asm-na/eng/216412.htm>.
- [3] Hood, III et al. *Computer with improved internal cooling system*. 6058009 United States, 2000 2-May.
- [4] Moore, G. *Cramming more components onto integrated circuits*. Electronics, Apr. 19, 1965 , Vols. 38 pp. 114-117.
- [5] Mahajan, Ravi, Chiu, Chia-pin and Chrysler, Greg. *Cooling a Microprocessor Chip*. IEEE, 2006.
- [6] Cengel, Yunas A., Boles, Michael A. *Thermodynamics: An Engineering Approach Fourth Edition*. McGraw-Hill, Copyright 2002.
- [7] Kandlikar, Satish G. *High Flux Heat Removal With Microchannels: A Roadmap of Challenges and Opportunities*. ASME 3rd International Conference on Microchannels and Minichannels, 2005.
- [8] Donahoe et al. *Appartus for liquid cooling of specific computer components*. 6,333,849 B1 United States of America, 12 25, 2001.
- [9] PELITAWIJAYA. Aquabay M1. 2009. Accessed: Apr. 2011.
<http://www.pelitawijaya.com/detail-368-Aquabay-M1-Thermaltake-CL-W0032.html>.
- [10] Kyrnin, Mark. *Guide To Laptop Size And Weight*. The New York Times Company., Copyright 2011 . Accessed: Apr. 2011.
<http://compreviews.about.com/od/buyers/a/Laptop-Size-and-Weight-Guide.htm>.

- [11] Sidewinder: Computer Systems Inc. *PC Liquid Cooling Pumps, Pump Controllers, Pump Tops and Dress Kits*. 2011 . Accessed: Apr. 2011.
<http://www.sidewindercomputers.com/pumps.html>.
- [12] White, Frank M. *Fluid Mechanics Fifth Edition*. McGraw-Hill , Copyright 2003.
- [13] UV Process Supply, Inc. *Selecting and Maintaining UV Ink and Coating Transfer Pumps*. Chicago : UV Process Supply, Inc., Copyright 2003. Manual.
- [14] *Vane Pumps*. Copyright 2007. Accessed: Apr. 2011.
<http://www.pumpschool.com/principles/vane.htm>.
- [15] Sahdev, Mukesh. *Centrifugal Pumps: Basics Concepts of Operation, Maintenance, and Troubleshooting, Part I*. The Chemical Engineers' Resource, 2010.
- [16] Garimella, Suresh V., Singhal, Vishal and Liu, Dong. *On-Chip Thermal Management With Microchannel Heat Sinks and Integrated Micropumps*. Proceedings of the IEEE, 2009.
- [17] Laboratory Networks. *Micro-Annular Gear*. Copyright 1996-2011. Accessed: Apr. 2011. <http://www.laboratorynetwork.com/product.mvc/Micro-Annular-Gear-Pumps-0001?VNETCOOKIE=NO>.
- [18] Ma, H. K., et al. *DEVELOPMENT AND APPLICATION OF A DIAPHRAGM MICRO-PUMP WITH PIEZOELECTRIC DEVICE*. Taipei : Department of Mechanical Engineering National Taiwan University, Taiwan Cooler Master Co., 2007.
- [19] Jeong, Ok Chan and Konishi, Satoshi. *Fabrication of a peristaltic micro pump with novel cascaded actuators*. J. Micromech. Microeng., January 2008.
- [20] Dewa, A. S., et al. *Development of LIGA-fabricated, self-priming, in-line gear pumps*. 1997. Transducers'97. pp. 757–760.
- [21] Cole-Parmer Instrument Co. *Cole-Parmer Product Manual 2001/02*. Vernon Hills, IL, 2001. Manual.
- [22] Miner, A. and Ghoshal, U. *Cooling of high-power-density microdevices using liquid metal coolants*. 2004. Appl. Phys. Lett. pp. vol. 85, pp. 506–508.
- [23] Richter, A., et al. *A micromachined electrohydrodynamic (EHD) pump*. Sens. Actuators A, 2001 , Vols. 29 pp. 159-168.

- [24] Jiang, L., et al. Packag, *Closed-loop electroosmotic microchannel cooling system for VLSI circuits*. *Manuf. Technol., IEEE Trans. Compon.*, 2002 , Vols. vol. 25, no. 3, pp. 347–355.
- [25] Spirax-Sarco Limited. *Check Valves. Spirax Sarco*. Copyright 2011. Accessed: Apr. 2011. <http://www.spiraxsarco.com/resources/steam-engineering-tutorials/pipeline-ancillaries/check-valves.asp>.
- [26] Olsson, Anders. *Valve-less Diffuser Micropumps*. Stockholm: Royal Institute of Technology: Department of Signals, Sensors and Systems, 1998.
- [27] Runstadler, P. W., Dolan, F. X. and Dean, R. C. *Diffuser data book*. Hanover, New Hampshire : Create Inc., 1975.
- [28] Tesla, Nikola. *Valvular Conduit*. 1329559 1920 3-Feb. United States Patent Office.
- [29] Forster, F. K., et al. *Design, fabrication and testing of fixed-valve micro-pumps.*: Proceedings of the ASME Fluids Engineering Division ASME 1995 pp. 39-44, 1995.
- [30] Gamboa, Adrian R., Morris, Christopher J. and Forster, Fred K. *Improvements in Fixed-Valve Micropump Performance Through Shape Optimization of Valves*. University of Washington, Department of Mechanical Engineering, 2005.
- [31] ANSYS Inc. *ANSYS-CFX Workbench version 12.1*. 2009 .
- [32] Galvis, Elmer. *Lower Entropy Generation in Microchannels With Laminar Single Phase Flow*. University of Waterloo, 2010.
- [33] Stublely, Gordon D. *ME566: CFD for Engineering Design* University of Waterloo, 2010.
- [34] Idel'Chik, I. E. *Handbook of Hydraulic Resistance: Coefficients of Local Resistance and of Friction*. Springfield, VA. 2251 : The U.S. Atomic Energy Commission and The National Science Foundation, Washington, D.C., 1960.
- [35] Wang, C. T., Leu, T. S. and Sun, J. M. *UNSTEADY ANALYSIS OF MICROVALVES WITH NO MOVING PARTS*. I Lan, Taiwan : National I Lan University, Dept. of Mechanical and Electro-Mechanical Engineering, 2007.

- [36] Kang, Jianke, Mantese, Joseph V. and Auner, Gregory W. *A self-priming, high performance, check valve diaphragm micropump made from SOI wafers*. JOURNAL OF MICROMECHANICS AND MICROENGINEERING, 2008.
- [37] Bendib, Samir, et al. *Analytical study and characterisation of micro-channel and passive micro-diode*. Grand Cedex : Group ESIEE, Laboratory of physics statistical ENS of Paris, 2001.
- [38] MicroMachining Centers. *ATOMETRIC G4-ULTRA CNC MicroMachining Centers*. Atometric Inc, Copyright 2008 . Accessed: Apr. 2011.
<http://www.atometric.com/index-1.html>.
- [39] Moffat, R.J. (1988). Describing the uncertainties in experimental results. *Experimental Thermal and Fluid Science*, 1, 3-17.
- [40] OMEGA Engineering, Inc. *PX26 Series Pressure Transducers: M1608/1204*. OMEGA Engineering, Inc, Copyright 2010.
- [41] Performance Micro Tool. *TR Series 2 Flute Micro End Mills*. Performance Micro Tool, Copyright 2010 . Accessed: Apr. 2011.
http://www.pmtnow.com/end_mills/tools/TR-2.asp.
- [42] Fluid Science, 1, 3-17. HARVARD Apparatus. *HD 2000 Syringe Pump Series User's Manual*. Instech Laboratories Inc.
- [43] Bardell, Ronald Louis. *The Diodicity Mechanism of Tesla-Type No-Moving-Parts Valves*. University of Washington, 2000